

August 2023

# Decadal Climate Variability in Mesoscale-resolving Coupled Models

Ilijana Mastilovic  
*University of Wisconsin-Milwaukee*

Follow this and additional works at: <https://dc.uwm.edu/etd>



Part of the [Atmospheric Sciences Commons](#)

---

## Recommended Citation

Mastilovic, Ilijana, "Decadal Climate Variability in Mesoscale-resolving Coupled Models" (2023). *Theses and Dissertations*. 3303.

<https://dc.uwm.edu/etd/3303>

This Dissertation is brought to you for free and open access by UWM Digital Commons. It has been accepted for inclusion in Theses and Dissertations by an authorized administrator of UWM Digital Commons. For more information, please contact [scholarlycommunicationteam-group@uwm.edu](mailto:scholarlycommunicationteam-group@uwm.edu).

DECADAL CLIMATE VARIABILITY IN MESOSCALE-  
RESOLVING COUPLED MODELS

by

Ilijana Mastilovic

A Dissertation Submitted in

Partial Fulfillment of the

Requirements for the Degree of

Doctor of Philosophy

in Atmospheric Science

at

The University of Wisconsin – Milwaukee

August 2023

## ABSTRACT

### DECADAL CLIMATE VARIABILITY IN MESOSCALE-RESOLVING COUPLED MODELS

by

Ilijana Mastilovic

The University of Wisconsin-Milwaukee, 2023  
Under the Supervision of Professor Sergey V. Kravtsov

Most of our knowledge about the causes of 20th-century climate change comes from simulation using numerical models. However, the observed climate variability and the one simulated by the state-of-the-art climate models exhibit substantial discrepancies at the decadal-to-multidecadal time scale and thus it hinders our fundamental understanding of the observed climate change. Evidence is mounting that vigorous intrinsic variability associated with mesoscale oceanic features contributes significantly to large-scale low-frequency climate variability, with fundamental implications for decadal climate low-frequency climate prediction. As of yet, extensive simulation of these decadal effects using high-resolution state-of-the-art coupled climate models has been computationally prohibitive, as it may require mesoscale-resolving atmospheric components. Here we study the effects of mesoscale air-sea coupling on large-scale low-frequency (interannual-to-multidecadal) climate variability using idealized high-resolution coupled climate models.

We hypothesized that resolving mesoscale oceanic fronts and eddies in both ocean and atmosphere will lead to the emergence of qualitatively new phenomena rooted, dynamically, in multi-scale ocean-atmosphere interactions. In particular, we propose that the climate system

may possess internal climate modes due to multi-scale ocean–atmosphere interactions involving (i) decadal variations in the meridional location and magnitude of the narrow (mesoscale, 100-km wide) sea-surface temperature (SST) fronts associated with the eastward-jet extension of oceanic western boundary currents (such as Gulf Stream); (ii) mesoscale response of the atmospheric planetary boundary layer (APBL) winds and, most importantly, ensuing large-scale (basin-scale-to-global-scale) response of the free atmosphere to these mesoscale SST anomalies; and (iii) subsequent modifications in the large-scale oceanic wind-driven gyres and further changes in the location and/or magnitude of the SST fronts. The unambiguous demonstration of a concerted action of these elements to result in the coherent decadal and longer internal climate variability has yet remained elusive, partly because modeling these dynamics requires at least semi-hemispheric-extent coupled ocean–atmosphere climate models with high horizontal resolution in both fluids; long, multidecadal simulations using these models are challenging to achieve due to their enormous computational expense.

The goal of the present work was to test our hypothesis above in a more idealized, numerically efficient model, yet the one containing the requisite dynamics required in the elements (i), (ii), (iii) of the proposed multi-scale coupled decadal climate modes. The model versions we developed and used here are based on the Quasi-Geostrophic Coupled Model (Q-GCM) of Hogg et al. (2003, 2006, 2009, 2014), which was revamped and modified to include a parameterized effect of SST anomalies on APBL wind, a new radiation/heat exchange parameterization meant to invigorate the coupling between the surface and free atmosphere, and, finally, the moisture dynamics and the associated latent heat sources that are likely to be essential in the large-scale

atmospheric response to mesoscale SST anomalies; the moist model version was dubbed the MQ-GCM model. Despite these modifications, we have to report that we did not thus far identify, in this model, the parameter regime conducive to the multi-scale coupled ocean–atmosphere modes we were looking for. The two main stumbling blocks we encountered were the inability of the ocean model to produce persistent self-sustained meridional shifts of the midlatitude SST front implied in (i), and the weak forced response of the model’s free atmosphere to variable SST fronts, even in the MQ-GCM model, which affects leg (ii) of the proposed feedback sequence. We used the insights obtained during the project to propose a set of suggestions for future work needed to rectify these issues.

© Copyright by Ilijana Mastilovic, 2023  
All Rights Reserved

To my Sava.

# TABLE OF CONTENTS

List of Figures .....	ix
List of Tables .....	xiii
List of Abbreviations .....	xiv
Acknowledgments.....	xv
Chapter 1.....	1
1. Introduction .....	1
1.1 Motivation.....	1
1.2 Background .....	4
1.2.1 Atmospheric response to mesoscale SST anomalies in extratropics.....	6
1.2.2 Atmospheric Feedback onto Oceanic Variability .....	8
1.2.3 Sensitivity of multi-scale air–sea coupling to the atmospheric model’s horizontal resolution...	9
1.3 This dissertation .....	12
1.3.1 Quasi-Geostrophic Coupled Model (Q-GCM) .....	12
1.3.2 Presentation layout.....	14
1.3.3 Timeline.....	19
Chapter 2.....	21
2. Quasi-Geostrophic Coupled Model (Q-GCM) .....	21
2.1 Model Geometrical and Dynamical Set Up .....	21
2.2 Quasi-geostrophic formulation of ocean and atmosphere’s interiors.....	26
2.3 Updates to the original, ‘dry’ version of Q-GCM.....	28
2.3.1 Radiative-convective equilibrium, atmospheric mean state and convective fluxes .....	28
2.3.2 Mixed-layer perturbation equation and entrainment formulation.....	33
2.3.3 Temperature-dependent flow in atmospheric mixed layer and partially coupled setup.....	39
2.2.4 Lateral boundary conditions for mass and temperature equations.....	41
Chapter 3.....	43
3. Experiments with dry Q-GCM .....	43
3.1 Experiments with the original Q-GCM modified to include SST-wind feedback .....	43
3.1.1 Diagnosing the effects of temperature-dependent wind-stress parameterizations in high-resolution coupled Q-GCM simulations.....	43
3.1.2 Comparing the simulations with and without temperature-dependent APBL wind.....	46
3.2 Bimodal behavior in the atmosphere-only modified dry Q-GCM configuration .....	56



3.3 Sensitivity of the Q-GCM atmosphere to the permanent SST-front displacements .....	63
Chapter 4.....	67
4. Moist Quasi-Geostrophic Coupled Model (MQ-GCM) formulation.....	67
4.1 Development of Moist Quasi-Geostrophic Coupled Model .....	67
4.2. MQ-GCM Simulations .....	73
Chapter 5.....	88
5. Large-scale effects of mesoscale air–sea coupling in MQ-GCM .....	88
5.1 Multi-century simulations under alternative ocean parameter settings .....	88
5.2 Atmospheric response to variable SST fronts in dry and moist Q-GCM models .....	91
5.2.1 Atmospheric variability in the simulations forced by the SST fronts fixed in time.....	92
5.2.2 SST front slowly drifting southward.....	93
5.2.3 Periodic SST front experiments.....	100
Chapter 6.....	103
6. Summary, conclusions, and outlook .....	103
6.1 Summary and discussion.....	103
6.2. Future directions.....	110
References .....	113
Appendices.....	124
Appendix A: Summary of model updates and code modifications.....	124
Appendix B: QGPV equation in a layered atmospheric model .....	127
Appendix C: Code availability.....	130
Curriculum Vitae .....	131

## LIST OF FIGURES

<b>Figure 1</b> – Schematic of a two-layer version of the Q-GCM model. Source: Hogg et al. 2014. ...	22
<b>Figure 2</b> – Downwind (upper plot) and Cross-wind (bottom plot) SST gradient from Hogg et al., 2009 TDWS run. ....	44
<b>Figure 3</b> – Downwind (upper plot) and Cross-wind (bottom plot) SST gradient from Feliks et al., 2004 TDWS run .....	45
<b>Figure 4</b> – Oceanic streamfunction climatology ( $S_v$ ) of control (left plot), TDWS (middle plot) and the difference between Control and TDWS simulations (right plot); coarse resolution.....	47
<b>Figure 5</b> – SST climatology [anomaly with respect to the reference temperature] (K) of Control (left plot), TDWS (middle plot), and the difference between Control and TDWS simulations (right plot); coarse resolution .....	47
<b>Figure 6</b> – ATS climatology (K) of control run (upper plot) and AST climatology differences (K) between TDWS and Control runs. ....	49
<b>Figure 7</b> – Oceanic Kinetic Energy (left panel) and SST variability (right panel); Control – blue, TDWS – red. ....	50
<b>Figure 8</b> – Second EOF of the first atmo layer streamfunction (upper panel) and PC timeseries associated with the lower-layer streamfunction EOF-2 .....	51
<b>Figure 9</b> – PC-2 Spectrum .....	51
<b>Figure 10</b> – EOF-1 (top row) and EOF-2 (bottom row) of SST from the Control (left column) and TDWS coupled simulation (right column).....	52
<b>Figure 11</b> – Fraction of variance accounted for by SST EOFs in the Control (blue) and TDWS (red) coupled simulations.....	52

<b>Figure 12</b> – SST snapshot from Control run (left) and TDWS run (right).....	54
<b>Figure 13</b> – Zonally uniform SST-front distributions used in the bimodality detection experiments.....	58
<b>Figure 14</b> – PDF of mid-layer streamfunction as a function of SST-front magnitude. (a) Left: CTRL simulation; (b) right: TDWS simulation. different colored curves in each panel correspond to 4 different magnitudes of SST front (see Fig. 17), with SST1 denoting the strongest front and SST4 – the weakest front.....	60
<b>Figure 15</b> – PDF of the leading PC of mid-layer streamfunction in the simulation forced by the strongest SST front at the drag coefficient set to $C_d=0.5e-3$ and equator-to-pole radiative contrast of $fs'=175W/m^2$ : (a) top left – 30 km resolution (b) top right – 40 km resolution; (c) bottom left – 120 km resolution; (d) bottom right – 120 km resolution [the same as (c)], but with the (tiny) time step of the 30-km-resolution simulation.....	62
<b>Figure 16</b> – Cross section of the idealized SST fronts along y axis used to force atmosphere-only Q-GCM sensitivity experiments. (a) Left: default configuration, with the front located in the middle of the ocean; (b) Right: shifted SST-front configuration, with the front located 1000 km to the south of the default position. ....	64
<b>Figure 17</b> – Climatology of the mid-layer atmospheric dynamic pressure ( $m^2/s^2$ ) from the experiment forced by the default SST front (top), shifted SST front (middle) and the difference between the two (bottom). Left: the results from the 60-km resolution experiment; right: 120-km-resolution experiment. The x and y axes show grid points at the 120 km spacing in both cases.....	64
<b>Figure 18</b> – Atmospheric mean state in control (a, d), partially coupled (b, e), and fully coupled (c, f) simulations involving temperature dependent wind in the atmospheric mixed layer. (a–c) Lower-layer zonal wind, $CI = 2 m s^{-1}$ , the zero contour is black; rectangle in the middle (here and in other figures) marks the location of the ocean. (d–f) Zonally averaged zonal wind ( $m s^{-1}$ ) in all layers (see legend). ....	75
<b>Figure 19</b> – Atmospheric mean state (continued). (a–c) Barotropic zonal wind, $CI = 2 m s^{-1}$ ; (d–f) interior temperature perturbation according to Eq. (12), $CI = 2 K$ ; (g–i) AML temperature, $CI = 2 K$ . ....	75

<b>Figure 20</b> – Atmospheric snapshots from the three simulations. (a–c) Lower-layer streamfunction; (d–f) AML temperature perturbation, CI = 2 K. Black curves show the zero contour.....	76
<b>Figure 21</b> – Oceanic time-mean streamfunction ( $S_v$ ) in control (a, d, g), partially coupled (b, e, h), and fully coupled (c, f, i) simulations involving temperature-dependent wind in the atmospheric mixed layer. Top, middle, and bottom layer results are shown in the corresponding rows of the figure. CI is shown in panel captions. Black curves show the zero contour. The panels also display the range of streamfunction in $S_v$ . .....	77
<b>Figure 22</b> – Time-mean SST (a–c, CI = 1 K) and ocean Ekman pumping (d–f, CI = $10^{-7}$ m s $^{-1}$ ) in control (a, d), partially coupled (b, e), and fully coupled (c, f) simulations involving temperature dependent wind in the atmospheric mixed layer. Black line on SST plots shows $-2$ °C anomaly with respect to the mean-state SST, approximately indicating the location of SST front; black line shows the zero contour on Ekman pumping plots. ....	78
<b>Figure 23</b> – Oceanic snapshots from the three simulations. (a–c) Upper layer streamfunction ( $S_v$ ); (d–f) OML temperature perturbation (K). .....	79
<b>Figure 24</b> – Time series of the basin-mean specific humidity (g kg $^{-1}$ ) in the four atmospheric layers (see the legend).....	80
<b>Figure 25</b> – Time series of the basin-mean evaporation (positive) and layer precipitation (negative) (m yr $^{-1}$ ); see the legend. ....	80
<b>Figure 26</b> – Climatological distribution of specific humidity (g kg $^{-1}$ ).....	81
<b>Figure 27</b> – Climatological distribution of evaporation (left) and precipitation in the mixed layer (right) (m yr $^{-1}$ ) .....	81
<b>Figure 28</b> – Climatological distribution of precipitation (m yr $^{-1}$ ); all layers. ....	82
<b>Figure 29</b> – Snapshot of precipitation (mm d $^{-1}$ ); all layers.....	83
<b>Figure 30</b> – The leading EOF of SST. (a–c) EOF pattern in control (a), partially coupled (b), and full temperature-dependent momentum coupling (c) simulations; the zero contour is black. (d,	

e) PC-1 (d) and Welch-periodogram spectra (e) (the type of the simulation corresponding to each curve shown is given in the legend). ..... 84

**Figure 31** – The leading EOF of the mid-layer atmospheric streamfunction. (a) EOF pattern in the control simulation. (b) Smoothed Welch-periodogram spectra of PC-1 in each simulation (the type of the simulation corresponding to each curve shown is given in the legend). ..... 86

**Figure 32** – Climatology of the lower-layer dynamic pressure ( $m^2/s^2$ ) from the coarse-resolution experiment of dry model with TDWS parametrization forced by: (a) default SST front; (b) shifted SST front; (c) slow-moving SST front. (d) The difference between (a) and (b); (e) the difference (a) and (c). The x and y axes show grid points at the 120 km spacing in both cases. .... 94

**Figure 33** – The leading (dimensional) EOF of the lower layer dynamic pressure smoothed by the 10-yr running-mean boxcar filter, from the simulations of the dry version of Q-GCM model with TDWS parametrization, for (a) control simulation using the default SST front position in the middle of the ocean; (b) shifted SST front simulation; and (c) slow-moving SST front simulation. The x and y axes show grid points at the 120 km spacing in both cases..... 97

**Figure 34** – Lower-layer streamfunction’s (dimensional) PC-1 from the dry model version with TDWS parametrization for the data smoothed using: (a) 10-year boxcar running mean, (b) 20-year boxcar running mean, and (c) 30-year boxcar running mean. .... 98

**Figure 35** – Same as Fig. 34 but from the moist version of the model with TDWS..... 99

**Figure 36** – Cross section of the SST front along the y axis for the amplitude  $A = 500$  km and period  $T_p=3$  years (equation 38) at: the first year (left plot), the second year (middle plot), and third year (right plot) of simulation, with  $y_o$  set to zero..... 100

**Figure 37** – Leading EOFs of lower-layer dynamic pressure from the periodic-front simulation using the dry version of Q-GCM model with TDWS parametrization: Left: EOF 1 and 2 patterns; right: the corresponding PC time series. Percentages in panel captions indicate the fraction of the total variance accounted for by each EOF..... 101

**Figure 38** – Same as in Fig. 36 but from the simulation using the moist version of the Q-GCM with TDWS parametrization..... 101

## LIST OF TABLES

<b>Table 1</b> – Timeline of this PhD project.....	20
<b>Table 2</b> – Standard Atmospheric parameters.....	24
<b>Table 3</b> – Standard oceanic parameters.....	25
<b>Table 4</b> – Mean-state parameters derived from (7)–(11), except for the last two rows detailing the ocean mean state based, loosely, on the observed oceanic vertical structure (note the difference here with the values used in the previous Q-GCM version). .....	32
<b>Table 5</b> – Atmospheric parameters used in the experiments on identification of bimodality of Section 3.2.....	59
<b>Table A1</b> - Differences between updated and original Q-GCM formulation .....	125
<b>Table A2</b> - Changes in the source code .....	126

## LIST OF ABBREVIATIONS

AML – Atmospheric Mixed Layer

APBL – Atmospheric Planetary Boundary Layer

CESM – Coupled Earth System Model

CTRL – Control

GCM – General Circulation Model

MABL – Mixed Atmospheric Boundary Layer

MQ-GCM – Moist Quasi-Geostrophic Coupled Model

OML – Ocean Mixed Layer

Q-GCM – Quasi-Geostrophic Coupled Model

QGPV – Quasi-geostrophic Potential Vorticity

SST – Sea Surface Temperature

TDWS – Temperature Dependent Wind Stress

WBC – Western Boundary Currents

## ACKNOWLEDGMENTS

First and foremost, I extend my deepest appreciation to my advisor, Professor Sergey Kravtsov. His invaluable insights, guidance, and expertise played a pivotal role in shaping this project. Moreover, his unwavering support and understanding not only made this PhD journey possible but also transformed it into a truly enjoyable and fulfilling experience.

I would like to thank the committee members and professors at Atmospheric Science Department at UMW: Professor Clark Evans, Professor Jonathan Kahl, and Professor Paul Roebber, as well as the professors at the University of Belgrade, Institute of Meteorology. Your ingenuity and humility are a true inspiration, motivating me to persist in my learning journey and push the boundaries of my abilities.

A special thanks to Professor William Dewar, whose presence as a committee member is an honor, considering his significant scientific work that has laid the foundation for this project.

I am grateful to my classmates for their willingness to share their knowledge, but also for their contribution to creating a wonderful time I had here at UWM.

Without the immense support system established by my family and friends, this journey would have been impossible. I find it difficult to convey my gratitude to my mom, dad, siblings - Iva, Isidor, Ljubomir, and my aunt Dana. Those are individuals who shower me with limitless love, bring happiness to my life, and help me go through challenging moments. A special thanks to my mom for her selflessness throughout my entire life and months of babysitting - her contributions have been immeasurable throughout our parental journey.



I am also surrounded by amazing friends who create countless enjoyable moments, make my life funnier, never fail to provide support, and genuinely rejoice in my accomplishments: Rosa, Spoma, Ruža, Tina, Zoka, Beka, Sanja, Jelena, Maryam, Gunes, Sanda, Ruška.

Last but not least, I want to express a heartfelt appreciation for everything my new family has brought into my life. Milan, your everyday love, support, unforgettable travels, adventures, jokes, and playful banter made this journey easier!

Sava, thank you for filling my days with joy, smiles, warm hugs, and enormous love. You are my greatest motivation, the wellspring of my energy, and an incredible source of happiness!

# Chapter 1

## 1. Introduction

### 1.1 Motivation

State-of-the-art climate models seemingly reproduce the observed non-uniform global warming, with periods of faster warming in 1910–1940 and 1970–2000, and a pause in between. However, closer inspection reveals substantial differences between the observations and model simulations (Evan et al., 2013; Eade et al., 2014; Kravtsov et al., 2014; Martin et al., 2014; Stockdale et al., 2015; Siegert et al., 2016). In recent work, Kravtsov, 2017 utilized ensembles of 20<sup>th</sup>-century climate simulations to isolate the forced signal and residual internal variability in a network of observed and modeled climate indices. The observed internal variability so estimated exhibits a pronounced multidecadal mode with a distinctive spatiotemporal signature, which is altogether absent in state-of-the-art climate model simulations. This single mode explains a major fraction of model–data differences; it may reflect either biases in the models’ forced response, models’ lack of requisite internal dynamics, or a combination of both.

There are several possible reasons behind the reported differences between observed and model simulated climate trends, which may arise from internal climate-system dynamics possibly misrepresented in the state-of-the-art climate models. These dynamics include sea-ice dynamics (Wyatt and Curry, 2014), positive cloud and dust feedback (Evan et al., 2013; Martin et al., 2014; Brown et al., 2016; Yuan et al., 2016), or large-scale atmospheric response to

ocean-induced sea-surface temperature (SST) anomalies (Kushnir et al., 2002; Eade et al., 2014; Stockdale et al., 2015; Siegert et al., 2016). In the latter category, a distinctive possibility is related to the atmospheric response to SST anomalies associated with oceanic fronts and eddies (features with spatial scales of 10–100 km, hereafter referred to as mesoscales) (Kravtsov et al., 2011; Kirtman et al., 2012; Siqueira and Kirtman, 2016; O’Reilly and Czaja, 2015; Parfitt et al., 2017). This possibility is the main focus of the present work. Mesoscale variability in the ocean contributes significantly to large-scale low-frequency climate variability (time scales of years to decades), with fundamental implications for near-term (interannual-to-decadal) climate prediction. As of yet, extensive simulation of these possible decadal effects using high-resolution state-of-the-art coupled climate models has been computationally prohibitive, as it may require mesoscale-resolving atmospheric components (Feliks et al., 2004, 2007, 2011; Brachet et al., 2012).

We strongly believe that climate model development activities should strive to understand and alleviate the present large discrepancies between the observed and simulated decadal-to-multidecadal climate variability, as these discrepancies hinder our fundamental understanding of the observed climate change. With this in mind, our main goal here is to identify and analyze the effects of mesoscale air–sea coupling on the interannual-to-decadal large-scale climate variability in multi-century simulations using an idealized and numerically efficient, yet mesoscale-resolving (in both fluids) coupled ocean–atmosphere model. Our hypothesis is that qualitatively and quantitatively new coupled phenomena will arise due to the multiscale (from mesoscale to basin-scale) atmosphere–ocean interactions in this model; these phenomena, by inference, would be relevant and important dynamically in more complete global climate

models. In particular, **we hypothesize that the oceanic frontal mesoscale air–sea interaction forces mesoscale anomalies in the atmospheric boundary layer and an ensuing large-scale response in the free atmosphere (perhaps largely associated with moist processes and latent heat release), which feeds back on and modifies the oceanic basin-scale circulation and, by inference, fronts, and eddies, leading to further modifications of the mesoscale air–sea interaction and large-scale atmospheric anomalies on decadal time scales.**

The objectives of this work are thus:

- to examine this hypothesis by designing and running multi-century simulations of the Quasi-Geostrophic Coupled Model (Q-GCM: Hogg et al., 2003) mimicking the (‘double-gyre’) coupled ocean–atmosphere system in the North Atlantic;
- to revamp this model to include additional relevant processes: in particular, an active hydrological cycle and the modification it introduces in the heat budget via the associated latent heat transfers;
- to analyze and interpret the above model simulations using a combination of advanced statistical analyses and *ad hoc* uncoupled or partially coupled simulations with the purpose of identifying and diagnosing the dynamics of the effects of mesoscale air–sea coupling on the system’s large-scale decadal variability.

## 1.2 Background

The long oceanic thermal and dynamical inertia makes the ocean a primary agent for generating potentially predictable climate signals on timescales from years to decades, whereas atmospheric intrinsic timescales are significantly shorter. The null hypothesis for climate variability views the ocean as a passive integrator of high-frequency noise associated with atmospheric geostrophic turbulence (Hasselmann, 1976; Frankignoul and Hasselmann, 1977; Frankignoul, 1985; Barsugli and Battisti, 1998; Xie, 2004). However, both observations (e.g., Chelton, 2013; Frenger et al., 2013) and decades of experimentation with wind-driven eddy-resolving ocean models (e.g., Berloff and McWilliams, 1999a; Primeau, 2002; Berloff et al., 2007; Hogg et al., 2009; Shevchenko et al., 2016, among many others) documented vigorous internal variability and the associated mesoscale features (fronts and eddies with spatial scales of 10–100 km) throughout the world ocean. Two key regions in which these eddies are most important are near the western boundary currents (WBC) such as the Gulf Stream region in the North Atlantic, Kuroshio in the North Pacific and their extensions, as well as in the Southern Ocean.

Mesoscale variability in these regions modulates atmospheric fronts and storms' intensity and distribution, thus affecting mesoscale atmospheric variability on short timescales locally (e.g., Maloney and Chelton, 2006; Minobe et al., 2008; Nakamura and Yamane, 2009; Bryan et al., 2010; Chelton and Xie, 2010; Kuwano-Yoshida et al., 2010; O'Neill et al., 2010, 2012; Frenger et al., 2013; O'Reilly and Czaja, 2015; Seo et al., 2016; Parfitt et al., 2017). Recent observational and modeling evidence strongly suggested that this mesoscale oceanic turbulence may also

imprint itself onto large-scale low-frequency climate modes (with timescales from intra-seasonal to decadal), which would have profound consequences for near-term climate predictability (e.g., Hogg et al., 2006; Siqueira and Kirtman, 2016). There are also indications that correctly capturing the magnitude and spatial extent of atmospheric response to oceanic mesoscale SST anomalies could require coupled climate models with high horizontal resolution in both their oceanic and atmospheric components (Feliks et al., 2004, 2007, 2011; Brachet et al., 2012: see Section 1.2.1 ); this would make the requisite long climate simulations using highly resolved state-of-the-art climate models computationally infeasible, which, in part, motivates and justifies our intermediate-complexity modeling approach.

There are three main aspects of the problem at hand that will form the framework of our research:

- Mesoscale ocean variability intrinsic to the ocean affecting the Maritime Atmospheric Boundary Layer (MABL) and, perhaps most importantly, the free atmosphere;
- an atmospheric feedback onto the ocean's mesoscale and, hypothetically, basin-scale variability required for an active multi-scale coupling;
- sensitivity of the multi-scale air–sea coupling to the atmospheric model's horizontal resolution.

Below we summarize the current state of knowledge with regards to these three aspects and map out our own research strategy.

### 1.2.1 Atmospheric response to mesoscale SST anomalies in extratropics

Mesoscale ocean features (fronts and eddies) force the atmosphere and induce a strong response in both the Maritime Atmospheric Boundary Layer (MABL) and in the free troposphere throughout the World Ocean, as evidenced by observations and numerical model simulations (e.g., Maloney and Chelton, 2006; Minobe et al., 2008; Nakamura and Yamane, 2009; Bryan et al., 2010; Chelton and Xie, 2010; Kuwano-Yoshida et al., 2010; O’Neill et al., 2010, 2012; Frenger et al., 2013; Ma et al., 2015; Seo et al., 2016, Ma et al., 2017; Parfit et al., 2017; Foussard et al., 2019 among others). This occurs through: (a) changes in MABL stability (Wallace et al., 1989) and (b) hydrostatic pressure adjustment (Lindzen and Nigam, 1987); see Small et al., 2008 and Chelton and Xie, 2010 for a review. Putrasahan et al., 2013 demonstrated that, in the Kuroshio region, both mechanisms (a) and (b) are important, with relative contributions depending on the spatial scale of SST anomalies. Putrasahan et al., 2017 also concluded that heat advection by oceanic mesoscale currents plays a key role in creating such SST anomalies and forcing the MABL response in the Gulf of Mexico. Czaja et al., 2011 proposed that the oceans can influence the troposphere through moist convection over the regions with strong mesoscale variability. In a study with a realistic General Circulation Model (GCM), Perlin et al., 2014 demonstrated a strong sensitivity of mesoscale ocean–atmosphere influence on the MABL vertical mixing scheme.

Many GCM studies with atmospheric-component horizontal resolutions of 50 km or so documented a pronounced influence of the mesoscale air–sea interactions on the atmospheric storm tracks (Miller and Schneider, 2000; Nakamura et al., 2008; Taguchi et al., 2009; Kelly et al.,

2010; Small et al., 2014; Ma et al., 2015, 2017; Piazza et al., 2016). A standard protocol for assessing the influence of mesoscale SST features on the atmospheric storm track is to compare the atmosphere-only simulations forced by highly resolved SST evolution and a smoothed version thereof. Kuwano-Yoshida and Minobe, 2017 and O'Reilly et al., 2017 demonstrated a poleward shift of the mean atmospheric jet position and storm track over the North Atlantic and North Pacific under mesoscale-resolving SST forcing. This shift affects weather upstream (westward) of the Kuroshio (Nakamura et al., 2012; Hayasaki et al., 2013; Sugimoto et al., 2021) and the Gulf Stream regions (Infanti and Kirtman 2019; Hirata et al., 2019; Liu et al., 2020). Additionally, many studies reveal a downstream (eastward) response to the SST fronts and eddies in the WBC regions such as variability in blocking frequency over Europe (O'Reilly et al., 2016, O'Reilly et al., 2017, Joyce et al., 2019), atmospheric circulation anomalies in the Gulf Stream extension (Wills et al., 2016), variability on the storm-track in the Kuroshio Extension region (Kuwano-Yoshida and Minobe, 2017; Ma et al., 2017) and rainfall variability over the western North America (Liu et al., 2021; Siqueira et al., 2021).

However, these types of conclusions are clearly model dependent due to any number of missing or misrepresented processes in a given model and are also a function of the numerical experimental design. For example, Tsopouridis et al., 2021 failed to identify any appreciable SST front's contribution to an individual cyclone intensification over the WBC regions aside from an indirect upstream impact on the environment where the cyclone forms.

In summary, unambiguous characterization of how the SST fronts and eddies affect the free atmosphere still remains a challenge. In this regard, another, distinctive possibility is that the response of the atmosphere to ocean induced mesoscale SST anomalies may involve a



nonlinear, weather-regime-type atmospheric behavior documented in the intermediate-complexity atmospheric (Marshall and Molteni, 1993; Kravtsov et al., 2005) and coupled models (Kravtsov et al., 2006, 2007); such behavior may lead to a nonlinear atmospheric sensitivity to ocean-induced SST anomalies and generate fundamentally coupled decadal climate modes (e.g., Kravtsov et al., 2008).

### 1.2.2 Atmospheric Feedback onto Oceanic Variability

Mesoscale perturbations in SST field associated with oceanic fronts and eddies affect, among other things, the atmospheric winds, which in turn feed back onto the ocean through perturbation heat fluxes (e.g., Xie, 2004; Jin et al., 2009) and Ekman pumping (Stern, 1965; McGillicuddy et al., 2007; Dewar and Flierl, 1987; Maloney and Chelton, 2006; Gaube et al., 2013, 2015; Chelton, 2013; Small et al., 2014). Feedback from those processes is negative, as it tends to reduce the intensity of the oceanic mesoscale perturbations that generated the wind anomalies in the first place. Hogg et al., 2009 utilized an ocean-only idealized eddy-resolving model coupled to a dynamic atmospheric mixed layer with a parameterized SST-driven wind component to demonstrate how mesoscale ocean-induced SST anomalies force variations in the wind stress and resulting Ekman-pumping anomalies, which, despite their small scale, significantly modify the large-scale ocean circulation through affecting the stability of the WBC and the ensuing damping of oceanic mesoscale turbulence. Seo et al., 2016 studied mesoscale eddy–wind interactions in the California Current System using a regional coupled model and documented the strong effect of mesoscale coupling on the regional climate dynamics, thereby

suggesting that it is essential to capture this feedback to faithfully simulate the observed regional climate variability.

Aside from the above mesoscale feedback, the documented large-scale atmospheric response (including that of the midlatitude jet and storm tracks; see Section 1.2.1) is bound to affect the basin-scale oceanic wind-driven circulation. This observation constitutes the entire premise of our research, by which the ‘upward’ branch of the ocean induced air–sea decadal communication occurs on mesoscales, whereas the ‘downward’ atmospheric feedback (modifying large-scale oceanic circulation and its accompanying mesoscale turbulence) acts on the basin scale.

### 1.2.3 Sensitivity of multi-scale air–sea coupling to the atmospheric model’s horizontal resolution

Feliks et al., 2004, 2007, 2011 and Brachet et al., 2012 examined the response of the atmosphere to mesoscale sea-surface temperature (SST) anomalies through hydrostatic pressure adjustment in an idealized atmospheric model. They showed that resolving an ocean front and mesoscale eddies affects atmospheric climatology, intraseasonal modes, as well as decadal variability (when forced with the observed SST history) in their model (see also Nakamura et al., 2008). These authors argued that atmospheric components of global climate models must resolve oceanic fronts to faithfully simulate the observed climate variability (see also Minobe et al., 2008). Ma et al., 2017 also concluded that “It is only when the (atmospheric) model has sufficient resolution to resolve small-scale diabatic heating that the full effect of

mesoscale SST forcing on the storm track can be correctly simulated,” with the ensuing consequences for atmospheric low-frequency variability associated with the downstream Rossby wave breaking (Piazza et al., 2016) and blocking (O’ Reilly et al., 2015). Consistent with this statement, Czaja et al., 2019 also argued that atmospheric models with horizontal resolutions coarser than 100 km do not adequately respond to important mesoscale signals from the ocean; the response improves in higher-resolution atmospheric GCM simulations of 40–50 km but is still underestimated compared to what’s suggested by observations.

By contrast, Bryan et al., 2010 proposed that accurate representation of mesoscale ocean–atmosphere coupling in a model depends more on the MABL vertical mixing scheme than on the ability of an atmospheric model to resolve a thermal front per se; this would justify the use of atmospheric resolutions on the order of 50 km, which is typical of the GCM studies of mesoscale ocean–atmosphere interactions. Indeed, in a recent proof-of-concept, pioneering work, Siqueira and Kirtman, 2016 documented large sensitivity of the decadal climate variability simulated by a state-of-the-art coupled climate model to this model’s oceanic resolution (and, hence, mesoscale activity) despite a relatively coarse atmospheric resolution. In particular, only the high-resolution model version that could capture the mesoscale-eddy-driven variability of major oceanic fronts was able to simulate realistic levels of decadal climate variability. In a similar vein, Chang et al., 2020 presented “an unprecedented set of high-resolution climate simulations” with a horizontal resolution of  $0.25^\circ$  for the atmosphere and  $0.1^\circ$  for the ocean. They found, among other things, a much better agreement between the simulated and observed variability in the atmospheric near-surface air temperature and SST over the entirety of the globe, including WBC regions and the Southern Ocean, compared to the lower-resolution

version of the Coupled Earth System Model (CESM). These results are consistent with idealized coupled eddy-resolving ocean–atmosphere simulations of Hogg et al., 2006, who found imprints of internal oceanic decadal variability associated with mesoscale eddies onto the atmospheric circulation in their model.

## 1.3 This dissertation

The oceanic and atmospheric components of the Hogg et al., 2006 Quasi-Geostrophic Coupled model (Q-GCM) were both eddy-resolving with respect to synoptic eddies in each of the fluids, having a resolution on the order of 10 km in the ocean and 100 km in the atmosphere. *The accumulating evidence about the importance of ocean–atmosphere coupling at the oceanic mesoscale for the long-term (interannual-to-multidecadal) climate variability presented above calls for a thorough analysis of the decadal climate variability in this model subjected to an increasing atmospheric resolution.* The Q-GCM model that we will be using here is ideally suited for this purpose, as it includes (albeit in a mechanistic fashion), essentially all of the required components of local mesoscale air–sea coupling, is dynamically transparent, and is an extremely numerically efficient tool to study the effects of this coupling on vigorous geostrophic turbulence produced in the long runs of this model.

### 1.3.1 Quasi-Geostrophic Coupled Model (Q-GCM)

The Quasi-Geostrophic Coupled Model (Q-GCM) was initially developed by Hogg et al., 2003 and has been substantially modified since. Its latest distribution and source code are publicly available at <http://www.q-gcm.org> and are fully documented in the Q-GCM users' guide, v1.5.0 (Hogg et al., 2014). The model couples the multi-layer quasi-geostrophic (QG) ocean and atmosphere components via ageostrophic mixed layers that regulate the exchange of heat and momentum between the two fluids. Q-GCM model can be configured as either a box (double

gyre) or a channel ocean (Southern Ocean) underneath a channel atmosphere; it conceptualizes the midlatitude climate system driven by the latitudinal variation of the incoming solar radiation. In addition to the oceanic mixed layer, the model physics incorporates a dynamically active atmospheric mixed layer (effectively, the atmospheric planetary boundary layer: APBL), the dependence of the wind stress on the ocean–atmosphere surface velocity difference, and a dynamically consistent parameterization of the entrainment heat fluxes between the model layers. It can also be easily modified to include a parameterization of sea-surface temperature (SST) feedback on the wind stress (e.g., Hogg et al., 2009), which will be an essential part of all of the model versions developed here. Q-GCM thus encompasses a richer, more comprehensive set of processes, enabling one to achieve a more accurate simulation of the ocean–atmosphere coupling, especially at mesoscales, relative to some other analogous conceptual models, which either assume the atmospheric near-surface temperature to be in equilibrium with SST (e.g., Feliks et al., 2004, 2007, 2011; cf. Schneider and Qiu, 2015) or relate this temperature in an ad hoc way to the instantaneous in situ distribution of the model’s tropospheric temperature (Kravtsov et al., 2005, 2006, 2007; Deremble et al., 2012).

The Q-GCM model was previously used for ocean-only and coupled experiments around the double-gyre problem (Hogg et al., 2005, 2006, 2007; Martin et al., 2020; Kurashina and Berloff, 2023a), as well as in the ocean-only studies of the Southern Ocean’s climate system (Hogg and Blundell, 2006; Meredith and Hogg, 2006; Hogg et al., 2008; Hutchinson et al., 2010; Kravtsov et al., 2011). Recently, Kurashina and Berloff, 2023b conducted and analyzed a set of fully coupled and partially coupled simulations to study the dynamical role of two-way ocean–atmosphere interaction in the Q-GCM model’s decadal variability.

A numerically efficient intermediate-complexity Q-GCM model provides an alternative (to highly resolved general circulation models) and unique tool ideally suited to help advance our understanding of multi-scale ocean–atmosphere interactions and their climatic impacts. Its QG dynamical core resolves well the geostrophic turbulence on either side of the ocean–atmosphere interface, including oceanic mesoscale eddies/fronts and atmospheric storm tracks. The default version of this model, however, lacks the parameterization of SST effects on the model’s APBL winds, although one such parameterization was tested in the Q-GCM’s ocean-only configuration by Hogg et al., 2009. This parameterization will be included in the revised version of Q-GCM model developed and analyzed here, along with extensive edits/additions to the model’s physical core.

### 1.3.2 Presentation layout

In this work, we will test our hypothesis about the existence of multi-scale coupled ocean–atmosphere decadal variability in multi-century simulations using an intermediate-complexity mesoscale-resolving Q-GCM model introduced above. As a part of our work, multiple model versions will be developed, with enhancements/modifications introduced in search of relevant dynamical processes and parameter regimes that would support the mesoscale air–sea interaction effects on large-scale climate variability in the model. We will also systematically explore the sensitivity of the simulated decadal variability to horizontal atmospheric resolution in the model.

**The model formulation, including modifications to the original dry version of the Q-GCM model, is described in Chapter 2.** These modifications include: (i) an improved radiative-convective scheme resulting in a more realistic model mean state and the associated model parameters (Section 2.2.1); (ii) a new formulation of entrainment in the atmosphere, which prompts a more efficient communication between the atmospheric mixed layer and free troposphere (Section 2.2.2); and (iii) addition of a temperature-dependent wind component in the atmospheric mixed layer and the resulting mesoscale feedbacks (Section 2.2.3).

The above modifications to the model's radiative-convective and entrainment formulations (Sections 2.2.1, 2.2.2) were prompted by our experiments with the original version of the Q-GCM model with the inclusion of both Hogg et al., 2009 and Feliks et al., 2004, 2007 SST-dependent MABL wind formulations (Section 2.2.3) in the context of coupled Q-GCM simulations with the standard (coarse) and fine (mesoscale resolving) atmospheric grid spacing. The description of these experiments (Section 3.1) opens **Chapter 3 devoted to the experimentation with the dry version of Q-GCM model.** We found that – consistent with previous studies (Dewar and Flierl, 1987; Maloney and Chelton, 2006; Hogg et al., 2009; Gaube et al., 2013, 2015; Chelton, 2013; Small et al., 2014) – the SST–wind-stress effects constitute negative feedback on the ocean and tend to reduce the intensity of the oceanic mesoscale perturbations that generated the mesoscale wind anomalies in the first place. In a coupled setting, this leads to a dilution of oceanic mesoscale features and the resulting lack of the model's sensitivity to atmospheric resolution. To address this issue in a way that was computationally feasible, we developed a partially coupled experimental design in which the atmosphere reacted to the full-resolution ocean-induced mesoscale SST perturbations, but the



ocean only experienced the large-scale wind-stress perturbations (see Section 2.2.3 for further details). In subsequent experimentation with all versions of the full coupled model, we then ran the standard (low) resolution (120 km) and high-resolution (20–40 km) atmospheric simulations without the SST-dependent atmospheric mixed-layer wind parameterization — hereafter referred to as the control simulation; the simulation with such a parameterization (hereafter, temperature-dependent wind-stress: TDWS simulation); plus the partially coupled version of the TDWS simulation (hereafter, partially coupled simulation).

Another surprising property of the original Q-GCM model (modified to include the temperature-dependent atmospheric mixed-layer wind) discussed in Section 3.1 was the apparent lack of sensitivity to SST fronts. In particular, the atmosphere-only Q-GCM simulations with and without an SST front, or with and without SST-dependent APBL winds, produced statistically identical atmospheric variability irrespective of the atmospheric resolution, in formal contrast to the resolution-dependent dynamics documented in Feliks et al., 2004, 2007. We hypothesized that this apparent confinement of the mesoscale SST effects to the APBL in the original version of the Q-GCM model may be due to the particular choices made in formulating the radiative core of the model and, most importantly, variable-thickness atmospheric mixed-layer entrainment formulation. The modified dry version of the model was thus developed to alleviate these concerns.

In Section 3.2 we describe the atmosphere-only experiments with this modified dry version of Q-GCM forced by steady SST fronts of various strengths (mimicking the setup in Feliks et al. studies) and look for modifications in the atmospheric behavior as a function of the atmospheric model’s horizontal resolution and control parameters, including the magnitude of

equator-to-pole radiative contrast and surface drag coefficients, along with some others. A particular finding that guided this activity was the evidence for the presence in the modified atmospheric module of the Q-GCM model, of the regime behavior associated with persistent shifts of the atmospheric jet north and south of its climatological position. Such behavior was previously reported in atmosphere-only and coupled QG setups by Kravtsov et al., 2005, 2006, but was not found in the original version of the Q-GCM model. The presence of the jet-position bimodality and regime behavior may be extremely important in the context of coupled ocean–atmosphere behavior in middle latitudes, as it may amount to nonlinear (and large) sensitivity of the atmosphere to small (in magnitude or scale) SST perturbations (Kravtsov et al., 2008). Studying nonlinear phenomena such as atmospheric jet’s bimodality requires long experiments, which is particularly challenging and time-consuming at high model resolutions, but we invested quite a bit of time in it given its potential key importance in the problem at hand. After no consistent trends in regime populations, depending on the model parameters, emerge in coarse-resolution simulations, we showed that the bimodal behavior may after all be an artifact of under-resolving the Rossby radius in these simulations, as the bimodality disappears in high-resolution simulations with otherwise identical parameters (including large horizontal diffusivities, with the same values as in the coarse-resolution runs).

Aside from a subtle issue of bimodality, the atmosphere-only experiments of Section 3.2 did not, once again, show any significant changes in the atmospheric *variability* in response to a sharpening or meridionally displaced SST front, irrespective of the model’s horizontal resolution, in an apparent remaining contradiction with the Feliks et al.’s results. Specifying an alternative *meridional position* of the SST front, however, produced enough radiative anomaly

(even in the control runs without temperature-dependent wind) to affect the mean location of the free-atmosphere jet as well, consistent with Deremble et al., 2012.

Despite the above sensitivity of the mean atmospheric jet position to the location of the SST front (even if not related to the mesoscale SST-wind feedbacks per se, as we argue), the atmospheric behaviors of our modified dry Q-GCM **coupled (control and TDWS) and partially coupled experiments** in Section 3.3 are statistically indistinguishable; these experiments thus clearly do not provide evidence to reject the null hypothesis that the mesoscale air–sea coupling has no effect on low-frequency variability of the free atmosphere.

The combination of the results outlined in the last two paragraphs presented two possible explanations for the lack of our hypothesized multi-scale coupled modes in Q-GCM experiments thus far: (i) the inability of the ocean model to produce, internally, persistent decadal SST front shifts able to force the atmospheric jet to "relocate" (as in the atmosphere-only experiments with meridionally shifted SST fronts); and (ii) a still less effective (compared to Feliks et al.'s parameterization, directly tying atmospheric winds to SST gradients) forcing of the free atmosphere by the SST-induced wind anomalies. To address (i), we increased the horizontal resolution in the ocean model to 5 km (as opposed to the 10 km resolution in our test runs thus far) and used the parameters from Martin et al., 2020 to put the model in a more turbulent regime characterized by a more pronounced low-frequency variability and mesoscale activity.

The most drastic change to the Q-GCM related to item (ii) was, however, the inclusion, in the model, of moist dynamics (Chapter 4), which may be key to midlatitude ocean–atmosphere coupling (Czaja and Blunt, 2011; Laîné et al., 2011; Deremble et al., 2012; Willison et al., 2013;

Foussard et al., 2019). Accordingly, this version of the model is to be referred to as the MQ-GCM model. Overall, the MQ-GCM model is shown to exhibit a rich spectrum of behaviors reminiscent of many of the observed properties of the Earth’s climate system but, once again, did not exhibit any significant alteration of large-scale low-frequency atmospheric behavior due to mesoscale air–sea coupling despite a larger, than that of a dry model, sensitivity of the MQ-GCM’s atmosphere to meridionally shifting SST front in the atmosphere-only context (Chapter 5).

In Chapter 6, we make an attempt to deepen our understanding of the problem at hand by synthesizing the numerous (mostly unfavorable) results obtained in the course of this work and offer a roadmap for further analyses. Thus far, however, the unequivocal demonstration of the multi-scale coupled ocean–atmosphere behavior involving mesoscale air–sea interaction remains elusive. The presentation concludes with a discussion of the importance, relevance, and meaning of our results, and proposed future work in Chapter 6. Finally, in Appendix A and B, we provide a detailed summary of the MQ-GCM changes and code modifications with respect to the original Q-GCM version, while Appendix C describes the code availability.

### 1.3.3 Timeline

To summarize the activities completed during the course of the project, Table 1 provides the timeline associated with various aspects of this work, referring to the model configurations and simulations described in Section 1.3.2.

Table 1 – Timeline of this PhD project

Model's version	Parametrization	Resolution	Description	Year
Model's Original Version: Coupled and Partially coupled	Control / TDWS / Delta T	<b>Coarse:</b> 120km atmo and 10km ocean; <b>High:</b> 20km atmo and 10km ocean	Searching for atmo variability in the old version of the Q-GCM. Presented at EGU 2019	2018/2019
MQ-GCM	N/A	N/A	Developing the new revamped version of the Q-GCM and adding moist dynamics (MQ-GCM).	2019/2020
Q-GCM: Atmo-only mode	CTRL and TDWS ( $\alpha_T = 1$ and $\alpha = 0.15$ ; see Section 2.3.3): fixed SST with 4 different SST strengths	<b>Coarse:</b> 120km <b>High:</b> 20km	Parameter sensitivity: different $F_s'$ , $C_d$ , and atmo diffusion coefficient.	2020/2021
Q-GCM: Atmo-only mode	CTRL and TDWS: SST with 4 different strengths, 5 values of $F_s'$ and 2 values of $C_d$	<b>Coarse:</b> 120km <b>High:</b> 40 & 30km	Searching for a bimodal regime in the Q-GCM.	2021/2022
Q-GCM: Atmo-only mode	CTRL and TDWS: fixed SST with 2 different magnitudes and 2 meridional locations	<b>Coarse:</b> 120km <b>High:</b> 60km	Checking free atmosphere sensitivity to the SST front's position.	2021/2022
MQ-GCM: Coupled and Partially coupled	Control / TDWS	<b>Coarse:</b> 120km atmo and 10km ocean; <b>High:</b> 40km atmo and 5km ocean	Looking for a parameter regime conducive to hypothesize multi-scale coupled behavior	2021/2022
MQ-GCM and Q-GCM: Atmo-only mode	CTRL and TDWS: periodic SST (3 and 100 years) and steady SST with 2 different locations	<b>Coarse:</b> 120km <b>High:</b> 40 km	Understanding forced response of the free atmosphere to variable SST fronts.	2022/2023

## Chapter 2

### 2. Quasi-Geostrophic Coupled Model (Q-GCM)

#### 2.1 Model Geometrical and Dynamical Set Up

The Quasi-Geostrophic Coupled Model (Q-GCM) was initially developed by Hogg et al., 2003 and has been substantially modified since: its latest distribution and source code are publicly available at <http://www.q-gcm.org> and are fully documented in the Q-GCM Users' Guide, v1.5.0 (Hogg et al., 2014). The model couples the multi-layer quasi-geostrophic (QG) ocean and atmosphere components via ageostrophic mixed layers that regulate the exchange of heat and momentum between the two fluids.

A schematic of the two-layer version of Q-GCM is presented in Figure 1, although in this study we used an additional third layer in each fluid. Three layers of the atmosphere have the unperturbed thicknesses of  $H_1 = 2000$  m,  $H_2 = 3000$  m,  $H_3 = 4000$  m; the channel lateral dimension is  $15360 \times 7680$  km. The ocean spans a rectangular horizontal area of  $3840 \times 4800$  km and also consists of three quasi-geostrophic layers with the unperturbed depths of  $H_1 = 350$  m,  $H_2 = 750$  m and  $H_3 = 2900$  m, where the values in parentheses correspond to those in the original version of the Q-GCM model and their alternative values characterize the modified model we will have developed below. The mixed layers of both fluids are embedded within the fluids' first layer. The above geometrical parameters, as well as fixed physical parameters of the model for the atmosphere and the ocean are listed in Tables 2 and 3, respectively.

The original setup of the Q-GCM model has a constant-thickness 100-m-deep oceanic mixed layer, but a variable-thickness atmospheric mixed layer. This variable-thickness version of the mixed layer was designed to prevent run-away atmospheric instability (Hogg et al., 2003). Upon experimenting with the Q-GCM model modified to include temperature-dependent winds in the atmospheric mixed layer (Section 3.1), we hypothesized that this design was partially responsible for a limited influence of SST onto the free QG atmosphere and resorted to the constant-thickness (1000 m) atmospheric mixed-layer formulation; for suppressing the run-away instability found in Hogg et al., 2003, we also modified the radiative transfer formulation to explicitly account for the radiative-convective balances that set up the atmospheric mean state and its thermal perturbations (see Section 2.2).

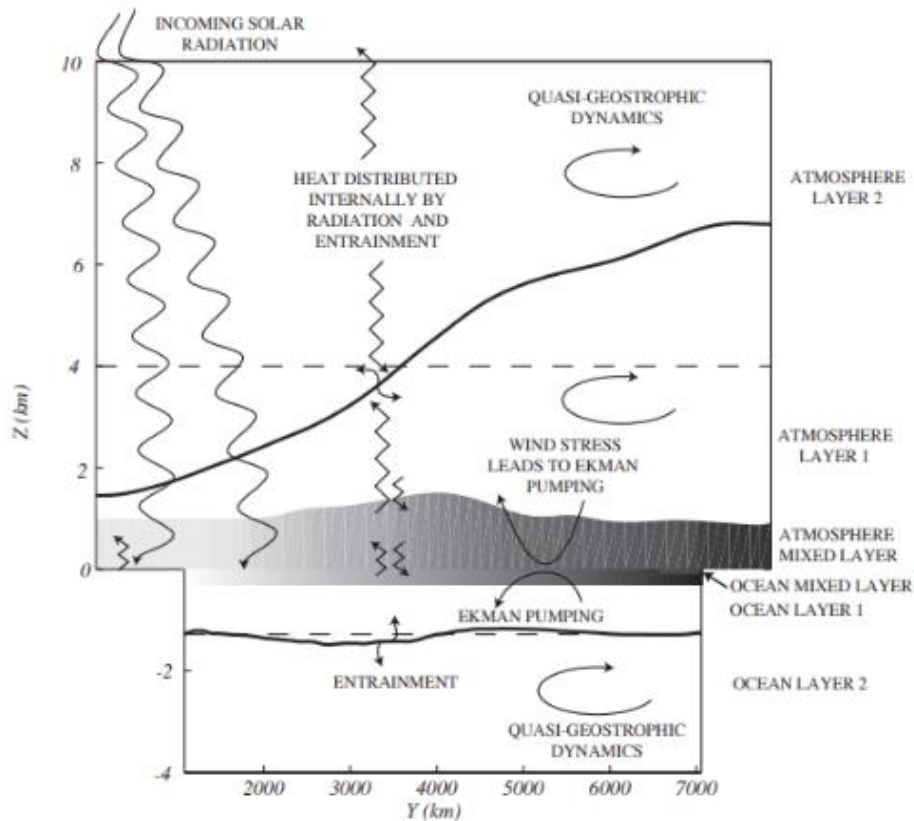


Figure 1 - Schematic of a two-layer version of the Q-GCM model. Source: Hogg et al. 2014.

The model is driven by the constant in time, latitudinally varying shortwave solar radiation, which is assumed to be transmitted through the atmosphere and absorbed by the ocean or (zero heat-capacity and conductivity) land. The atmosphere is then forced from below by the long-wave radiation from the ocean/land surface, as well as via ocean–atmosphere sensible/latent heat exchange. Both the atmosphere and ocean exhibit entrainment mass and heat fluxes between each layer. These entrainment fluxes are associated with vortex stretching resulting in modifications to atmospheric and oceanic circulation. In contrast to the thermally driven atmosphere, the major driver of the oceanic circulation in the model is the wind-induced Ekman pumping of the ocean interior, whereas most of the effects of the large-scale buoyancy-driven oceanic circulation are implicit in the pre-specified density stratification of the ocean.

The key feature of the modified Q-GCM formulation here is the inclusion of the temperature-dependent mixed-layer wind component. It is through this component that large-magnitude mesoscale Ekman pumping anomalies and the associated entrainment fluxes are generated; these fluxes could be able to drive a substantial response in the free atmosphere, which is the major focus of the present study.

Standard sets of atmospheric and oceanic parameters are listed in Tables 2 and 3, respectively. Throughout this project we performed numerous experiments with modified parameter values; these values will be spelled out in the corresponding sections of the presentation.



Table 2 - Standard Atmospheric parameters

PARAMETER	VALUE	DESCRIPTION
${}^aX \times {}^aY$	15360 × 7680 km	Domain size
${}^aH_k$	(2, 3, 4) km	Layer thicknesses
${}^aH_m$	1000 m	Mixed layer thickness (fixed)
${}^a\rho$	1 kg/m <sup>3</sup>	Density
${}^aC_p$	1000 J/kg/K	Specific heat capacity
${}^a g'_k$	(1.2, 0.4) m/s <sup>2</sup>	Reduced gravity
$C_D$	$1.3 \times 10^{-3}$	Drag coefficient
${}^aA_4$	$2 \times 10^{14}$ m <sup>4</sup> /s	Biharmonic viscosity coefficient
${}^a\alpha_{bc}$	1	Mixed boundary condition coefficient
${}^aK_2$	$2.7 \times 10^4$ m <sup>2</sup> /s	Temperature diffusion coefficient
${}^aK_4$	$3 \times 10^{14}$ m <sup>4</sup> /s	4th order diffusion coefficient
$Z_m$	200 m	Optical depth in the mixed layer
${}^a r_{dk}$	(465, 243) km	Baroclinic Rossby radii (derived)

Table 3 - Standard oceanic parameters

PARAMETER	VALUE	DESCRIPTION
$^{\circ}X \times ^{\circ}Y$	3840 x 4800 km	Domain size
$^{\circ}H_k$	(350, 750, 2900)	Layer thicknesses
$^{\circ}H_m$	100 m	Mixed layer thickness
$^{\circ}\rho$	1000 kg/m <sup>3</sup>	Density
$^{\circ}C_p$	4000 J/kg/K	Specific heat capacity
$^{\circ}g'_k$	(0.05, 0.025) m/s <sup>2</sup>	Reduced gravity
$\delta_{ek}$	1 m	Bottom Ekman layer thickness
$^{\circ}A_2$	0 m <sup>2</sup> /s	Laplacian viscosity coefficient
$^{\circ}A_4$	$1.0 \times 10^{10}$ m <sup>4</sup> /s	Biharmonic viscosity coefficient
$^{\circ}\alpha_{bc}$	0.5	Ocean mixed BC coefficient
$^{\circ}K_2$	380 m <sup>2</sup> /s	Temperature diffusion coefficient
$^{\circ}K_4$	$4 \times 10^{10}$ m <sup>4</sup> /s	4th order diffusion coefficient
$^{\circ}r_{dk}$	(51, 32) km	Baroclinic Rossby radii (derived)

## 2.2 Quasi-geostrophic formulation of ocean and atmosphere's interiors

The starting point for the models used in this study is the Q-GCM formulation described in Hogg et al., 2014; we refer the reader to the Q-GCM Guide for more detailed information about this default model. For the sake of completeness, we here briefly present the quasi-geostrophic equations which govern the model dynamics and emphasize the important changes made to the model throughout this study effort.

Q-GCM model incorporates quasi-geostrophic dynamics on a  $\beta$ -plane in its  $K$ -layer oceanic and atmospheric modules (here,  $K=3$ ); these dynamics are governed by the equations describing the evolution of quasi-geostrophic potential vorticity. For a flat-bottom ocean (used here for simplicity, although the topography is included in the latest Q-GCM distribution):

$${}^o q_{k,t} + J({}^o \psi_k, {}^o q_k) = \frac{f_0}{{}^o H_k} ({}^o e_{k-1} - {}^o e_k) + {}^o A_2 \nabla_H^4 {}^o \psi_k - {}^o A_4 \nabla_H^6 {}^o \psi_k; \quad k = 1,2,3 \quad (1)$$

where

$${}^o q_k = \nabla_H^2 {}^o \psi_k + \frac{f_0}{{}^o H_k} ({}^o \eta_k - {}^o \eta_{k-1}) + \beta(y - y_o); \quad k = 1,2,3 \quad (2)$$

and

$${}^o \eta_k = \frac{f_0}{{}^o g'_k} ({}^o \psi_{k+1} - {}^o \psi_k), \quad {}^o g'_k = g \frac{({}^o \rho_{k+1} - {}^o \rho_k)}{{}^o \rho_0}; \quad k = 1,2; \quad {}^o \eta_0 = {}^o \eta_3 = 0 \quad (3)$$

In the equations above, the left superscript 'o' refers to the oceanic quantities,  ${}^o q_k$  is the potential vorticity for ocean layer  $k$ , counted from the surface down,  ${}^o \psi_k$  is the layer- $k$  geostrophic streamfunction,  ${}^o H_k$  are layer thicknesses and  ${}^o g'_k$  — layer densities (all close to

the representative water density  ${}^o\rho_0$ ), with  $k = 1,2,3$ . Furthermore,  ${}^o\eta_k$  are the perturbation displacements of the interface between the top/middle and middle/bottom layers,  ${}^og'_k$  are reduced gravity coefficients (for both of these  $k = 1,2$ ),  $f_0$  and  $\beta$  are the Coriolis parameter and its  $y$ -derivative at the central latitude  $y_0$ , respectively,  ${}^oA_2$  and  ${}^oA_4$  are viscosity coefficients for the Laplacian and biharmonic friction parameterizations, the subscript  $t$  denotes the time derivative,  $\nabla_H^2$  is the horizontal Laplacian operator, and  $J$  is the Jacobian operator.

The ocean model is driven by the entrainment  ${}^oe_0 = {}^ow_{ek}$  associated with the surface Ekman pumping  ${}^ow_{ek}$  computed as the curl of the wind stress; the model also includes Ekman dissipation at the bottom, with  ${}^oe_3 \sim \nabla_H^2 \psi_3$ , as well as a thermally driven entrainment  ${}^oe_1$  (between ocean layers 1 and 2) due to heat exchange between the ocean's layer-1 and the mixed layer.

The atmospheric module mirrors the ocean module: it is set up in a fluid comprised of layers with constant potential temperatures  $\theta_k$  and variable depths (see above). In particular:

$${}^aq_{kt} + J({}^a\psi_k, {}^aq_k) = \frac{f_0}{aH_k} ({}^ae_k - {}^ae_{k-1}) - {}^oA_4 \nabla_H^6 {}^a\psi_k; \quad k = 1,2,3; \quad (4)$$

$${}^aq_k = \nabla_H^2 {}^a\psi_k + \frac{f_0}{aH_k} ({}^a\eta_k - {}^a\eta_{k-1}) + \beta(y - y_0); \quad k = 1,2,3; \quad (5)$$

$${}^a\eta_k = \frac{f_0}{ag'_k} ({}^a\psi_k - {}^a\psi_{k+1}), \quad {}^ag'_k = g \frac{(\theta_{k+1} - \theta_k)}{\theta}; \quad k = 1,2; \quad {}^a\eta_0 = {}^a\eta_3 = 0. \quad (6)$$

Note that the layer indexing in the equations above goes from the surface upward and the Laplacian friction term is omitted; otherwise, these equations are completely analogous to the

oceanic equations (the atmospheric variables are denoted above by the left superscript 'a'). At the lower atmospheric boundary, the entrainment flux  ${}^a e_0 = {}^a w_{ek}$  solely represents, in the original Q-GCM formulation, Ekman dissipation (thus signifying the momentum transfer from the atmosphere to the ocean); in the modified version of the model to be developed here it will also include a temperature dependent component capable of driving mesoscale air–sea interaction (Section 2.3.3). The atmospheric model (and thus the entire coupled model) is driven through interior entrainment fluxes  ${}^a e_1, {}^a e_2$  in Eq. (4) ( ${}^a e_3$  is set to zero), which are a byproduct of perturbing the mean-state radiative-convective equilibrium (Section 2.3.1) by a latitudinally non-uniform insolation. The new radiation/heat exchange formulation and mixed layer/entrainment formulation developed here (Section 2.3) are aimed to help achieve a parameter regime with enhanced (and, arguably, more realistic) coupling between oceanic and atmospheric dynamics in the model. They are further modified in formulating the new version of the model with an active hydrological cycle and the associated latent-heat feedbacks (Chapter 4).

## 2.3 Updates to the original, 'dry' version of Q-GCM

### 2.3.1 Radiative-convective equilibrium, atmospheric mean state and convective fluxes

The purpose of developing a new, revamped version of the Q-GCM model is to address an apparent lack of the Q-GCM free atmosphere's sensitivity to SST anomalies (Chapter 3, Section 3.1), contrary to some theoretical and observational evidence otherwise (Chapter 1). In particular, Feliks et al., 2004, 2007 used an analogous model to document the sensitivity of the

QG atmosphere to the entrainment forcing associated with the SST front and report a substantial effect of mesoscale SST gradients on the large-scale atmospheric dynamics in mesoscale-resolving simulations. Their entrainment formulation would be essentially the same as the one used here in the limiting case of the constant-depth mixed layer with the temperature slaved to SST. We thus hypothesized that the variable-thickness atmospheric mixed-layer formulation of Hogg et al., 2003 somehow limits the effects of the mesoscale SST forcing on the free atmosphere. Going back to the constant-depth atmospheric mixed-layer setup, however, brings about the atmospheric instability described in Hogg et al., 2003 (which was, of course, the primary reason for introducing the variable-thickness atmospheric mixed layer there). To address this issue requires an updated radiative transfer parameterization below, which, as we will see, contributes to a more realistic performance of the modified Q-GCM model.

More specifically, the previous version of Q-GCM assumes purely radiative equilibrium to compute the atmospheric mean state. In our revised version, this assumption is replaced by that of the radiative-convective mean-state balance. We denote the actual (not potential) vertically averaged temperatures within each of the interior atmospheric layers as  ${}^aT_k, k = 1,2,3$  to write, over ocean,

$$\begin{aligned}
\rho {}^oC_p {}^oH_m {}^o\dot{T}_m &= -F_\lambda - F_0^\uparrow - F_m^\downarrow - F_s + {}^oF_m^{e+}, \\
{}^a\rho {}^aC_p {}^aH_m {}^a\dot{T}_m &= F_\lambda + F_0^\uparrow + F_m^\downarrow - (F_m^\uparrow + {}^aF_m^{e-} + F_1^\downarrow), \\
{}^a\rho {}^aC_p {}^aH_1 {}^a\dot{T}_1 &= F_m^\uparrow + F_1^\downarrow + {}^aF_m^{e+} - (F_1^\uparrow + F_2^\downarrow + {}^aF_1^{e-}), \\
{}^a\rho {}^aC_p {}^aH_2 {}^a\dot{T}_2 &= F_1^\uparrow + F_2^\downarrow + {}^aF_1^{e+} - (F_2^\uparrow + F_3^\downarrow + {}^aF_2^{e-}), \\
{}^a\rho {}^aC_p {}^aH_3 {}^a\dot{T}_3 &= F_2^\uparrow + F_3^\downarrow + {}^aF_2^{e+} - F_3^\uparrow
\end{aligned} \tag{7}$$

Here the dot denotes the time derivative and other notations follow the Q-GCM Users' Guide, v1.5.0 (Hogg et al., 2014). In particular, the upward/downward arrow subscripts denote upwelling/downwelling longwave radiative fluxes within each of the layers  $k = m$  (mixed layer), 1, 2, 3 or the surface (0), the subscripts  $e -$  and  $e +$  denote entrainment fluxes below and above interface  $k$ , the subscript  $s$  refers to the solar radiation and  $\lambda -$  to the ocean-atmosphere sensible/latent heat exchange. The fluxes describing non-radiative heat exchange between the layers are interpreted, in the mean state, as convective fluxes parameterized in the following way (cf. Manabe and Strickler, 1964; Manabe and Wetherald, 1967; Ramanathan and Coakley, 1978):

$$\begin{aligned}
\bar{F}_\lambda &= K(\ ^o\bar{T}_m - \ ^a\bar{T}_m - \gamma_c \Delta H_m); \Delta H_m = \ ^aH_m/2, \\
\ ^a\bar{F}_m^e &= \ ^a\bar{F}_m^{e-} = \ ^a\bar{F}_m^{e+} = K(\ ^a\bar{T}_m - \ ^a\bar{T}_1 - \gamma_c \Delta H_1); \Delta H_1 = (\ ^aH_m + \ ^aH_1)/2, \\
\ ^a\bar{F}_1^e &= \ ^a\bar{F}_1^{e-} = \ ^a\bar{F}_1^{e+} = K(\ ^a\bar{T}_1 - \ ^a\bar{T}_2 - \gamma_c \Delta H_2); \Delta H_2 = (\ ^aH_1 + \ ^aH_2)/2, \\
\ ^a\bar{F}_2^e &= \ ^a\bar{F}_2^{e-} = \ ^a\bar{F}_2^{e+} = K(\ ^a\bar{T}_2 - \ ^a\bar{T}_3 - \gamma_c \Delta H_3); \Delta H_3 = (\ ^aH_2 + \ ^aH_3)/2.
\end{aligned} \tag{8}$$

The upward fluxes in above equation are all positive (or are otherwise set to zero), with the coefficient  $K = 200 \text{ W m}^2 \text{ K}^{-1}$  and the critical lapse rate  $\gamma_c = 6.5 \text{ K km}^{-1}$ . The potential temperatures of the atmospheric layers are given by:

$$\begin{aligned}
\bar{\theta}_m &= \ ^a\bar{T}_m + \Gamma_d \ ^aH_m/2; \\
\theta_1 &= \ ^a\bar{T}_1 + \Gamma_d (\ ^aH_m + \ ^aH_1/2); \\
\theta_2 &= \ ^a\bar{T}_2 + \Gamma_d (\ ^aH_m + \ ^aH_1 + \ ^aH_2/2); \\
\theta_3 &= \ ^a\bar{T}_3 + \Gamma_d (\ ^aH_m + \ ^aH_1 + \ ^aH_2 + \ ^aH_3/2),
\end{aligned} \tag{9}$$

where  $\Gamma_d = g / {}^a C_p$  is the dry adiabatic lapse rate (of about  $10 \text{ K km}^{-1}$ ).

The radiative fluxes in Eq. (7) are parameterized assuming that the atmospheric layers have constant emissivity  $\varepsilon_m, \varepsilon_1, \varepsilon_2, \varepsilon_3$ , and the Stefan-Boltzmann expressions for perturbation fluxes are linearized with respect to the basic-state:

$$\begin{aligned}
F_0^\uparrow &= A_0 + D_0 {}^o T_m', \\
F_m^\uparrow &= F_0^\uparrow(1 - \varepsilon_m) + \varepsilon_m(A_m + B_m {}^a T_m'), \\
F_1^\uparrow &= F_m^\uparrow(1 - \varepsilon_1) + \varepsilon_1(A_1 + B_1 {}^a T_1'), \\
F_2^\uparrow &= F_1^\uparrow(1 - \varepsilon_2) + \varepsilon_2(A_2 + B_2 {}^a T_2'), \\
F_3^\uparrow &= F_2^\uparrow(1 - \varepsilon_3) + \varepsilon_3(A_3 + B_3 {}^a T_3'), \\
F_3^\downarrow &= -\varepsilon_3(A_3 + B_3 {}^a T_3'), \\
F_2^\downarrow &= F_3^\downarrow(1 - \varepsilon_2) - \varepsilon_2(A_2 + B_2 {}^a T_2'), \\
F_1^\downarrow &= F_2^\downarrow(1 - \varepsilon_1) - \varepsilon_1(A_1 + B_1 {}^a T_1'), \\
F_m^\downarrow &= F_1^\downarrow(1 - \varepsilon_m) - \varepsilon_m(A_m + B_m {}^a T_m'),
\end{aligned} \tag{10}$$

where

$$\begin{aligned}
A_0 &= \sigma {}^o \overline{T_m^4}, & D_0 &= 4\sigma {}^o \overline{T_m^3}, \\
A_m &= \sigma {}^a \overline{T_m^4}, & B_m &= 4\sigma {}^a \overline{T_m^3}, \\
A_k &= \sigma {}^o \overline{T_k^4}, & B_k &= 4\sigma {}^a \overline{T_k^3};
\end{aligned} \tag{11}$$

$k = 1, 2, 3$  and  $\sigma$  is the Stefan–Boltzmann constant.

To solve for the mean state, we set all of  $F_m^{e+}, {}^o T_m', {}^a T_m', {}^a T_1', {}^a T_2', {}^a T_3'$  to zero and numerically integrate Eq. (7) to (11) to equilibrium, using Euler differences in time with the time step of 5 min. Setting  $\varepsilon_m = \varepsilon_1 = \varepsilon_2 = \varepsilon_3 = 0.45$  along with  $\overline{F_s} = -240 \text{ W m}^{-2}$  results in the mean state whose parameters are listed in Table 4.



Table 4 - Mean-state parameters derived from (7)–(11), except for the last two rows detailing the ocean mean state based, loosely, on the observed oceanic vertical structure (note the difference here with the values used in the previous Q-GCM version).

PARAMETERS	VALUE(S)	DESCRIPTION, UNITS
$\begin{pmatrix} {}^o\overline{T}_m, {}^a\overline{T}_m, {}^a\overline{T}_1, \\ {}^a\overline{T}_2, {}^a\overline{T}_3, \end{pmatrix}$	(286.5, 282.6, 272.4, 255.9, 233.1)	Atmospheric mean-temperature structure (K)
$\begin{pmatrix} {}^o\overline{T}_m, {}^a\overline{\theta}_m, \theta_1, \\ \theta_2, \theta_3, \end{pmatrix}$	(286.5, 287.6, 292.4, 300.9, 313.1)	Atmospheric potential-temperature structure (K)
$\Delta_1^a T \equiv \theta_2 - \theta_1,$ $\Delta_2^a T \equiv \theta_3 - \theta_2$	8.5, 12.2	Cross-interfacial temperature difference (K), atmosphere
$\overline{\theta}$	302.7	Vertically averaged mean potential temperature (K)
${}^a g'_k = g \Delta_1^a T / \overline{\theta}$	(0.3, 0.4)	Reduced gravity ( $\text{m s}^{-2}$ ), atmosphere
$(\overline{F}_\lambda, {}^a\overline{F}_m^e, {}^a\overline{F}_1^e, {}^a\overline{F}_2^e)_a$	(143.3, 90.5, 45.3, 15.8)	Convective heat fluxes ( $\text{W m}^{-2}$ )
$({}^o T_1, {}^o T_2, {}^o T_3)$	${}^o\overline{T}_m - (2, 10, 14)$	Oceanic mean-temperature structure (K)
$\Delta_1^o T \equiv {}^o T_1 - {}^o T_2,$ $\Delta_2^o T \equiv {}^o T_2 - {}^o T_3,$	8 4	Cross-interfacial temperature difference (K), ocean

The atmospheric optical depth decreases with altitude, but so do the unperturbed thicknesses of our chosen atmospheric layers, making the constant layer emissivities above a reasonable first approximation commensurate with an idealized nature of the present model. The model has a realistic (time-mean, global-mean) vertical temperature distribution. Note that the

atmospheric reduced gravities are derived, in this version of the model, from the mean-state parameters rather than being prescribed (at  $1.2$  and  $0.4 \text{ m s}^{-2}$ ), as in the previous version (see the appendix B for further details). The climatological solution above is formally obtained over the ocean, but it also applies over land of zero heat capacity (since the steady state does not depend on the heat capacity of the surface); the land's zero heat capacity is also a feature of the original Q-GCM formulation. The near-surface convective fluxes, however, would generally be different over the ocean and over land (which occupies a significant fraction of the atmospheric channel, including fairly large strips both north and south of the ocean to avoid the distortion of ocean–atmosphere interaction by the effects associated with the atmospheric boundary conditions); the values of the convective fluxes in Table 4 should thus be interpreted to represent zonally averaged fluxes. Below, in Section 2.3.2, we will describe, among other things, modifications of the atmospheric-mixed-layer (AML) perturbation equation (that is, the one describing the evolution of the anomalies with respect to the mean state) over land regions.

### 2.3.2 Mixed-layer perturbation equation and entrainment formulation

The perturbation equations in the mixed layers, for primed variables, have the same form as the first two Eq. (7), aside from the addition of advective and entrainment fluxes which we will discuss further below; hereafter, we will drop primes in all perturbation equations for convenience. We will assume that the atmospheric perturbation temperature is vertically

uniform, consistent with an active role of convection processes (cf. Manabe and Wetherald, 1967), viz.

$${}^aT'_1 = {}^aT'_2 = {}^aT'_3 \equiv {}^aT' = -({}^a\eta_1\Delta_1^aT + {}^a\eta_2\Delta_2^aT)/{}^aH; \quad {}^aH \equiv {}^aH_1 + {}^aH_2 + {}^aH_3, \quad (12)$$

( $\Delta_k^aT$  above denotes the potential temperature jump across the  $k$ -th interface; see Table 4) which allows one to express all perturbation radiative fluxes in Eq. (10) via perturbation oceanic and atmospheric mixed layer temperatures  ${}^oT_m$ ,  ${}^aT_m$  and interfacial displacements  ${}^a\eta_1$ ,  ${}^a\eta_2$ ; in particular,

$$\begin{aligned} F_0^\uparrow &= D_0 {}^oT_m, \\ F_m^\uparrow &= D_m^\uparrow {}^aT_m + E_0^\uparrow {}^oT_m, \\ F_1^\uparrow &= A_{1,1}^\uparrow {}^a\eta_1 + A_{1,2}^\uparrow {}^a\eta_2 + D_1^\uparrow {}^aT_m + E_1^\uparrow {}^oT_m, \\ F_2^\uparrow &= A_{2,1}^\uparrow {}^a\eta_1 + A_{2,2}^\uparrow {}^a\eta_2 + D_2^\uparrow {}^aT_m + E_2^\uparrow {}^oT_m, \\ F_3^\uparrow &= A_{3,1}^\uparrow {}^a\eta_1 + A_{3,2}^\uparrow {}^a\eta_2 + D_3^\uparrow {}^aT_m + E_3^\uparrow {}^oT_m, \\ F_3^\downarrow &= A_{3,1}^\downarrow {}^a\eta_1 + A_{3,2}^\downarrow {}^a\eta_2, \\ F_2^\downarrow &= A_{2,1}^\downarrow {}^a\eta_1 + A_{2,2}^\downarrow {}^a\eta_2, \\ F_1^\downarrow &= A_{1,1}^\downarrow {}^a\eta_1 + A_{1,2}^\downarrow {}^a\eta_2, \\ F_m^\downarrow &= F_1^\downarrow(1 - \varepsilon_m) + D_m^\downarrow {}^aT_m, \end{aligned} \quad (13)$$

where all of the  $A, D, E$  coefficients can be written in terms of the known mean-state parameters. The Eq. (13) above should be compared with (4.2–4.6) of the Q-GCM User's Guide (Hogg et al. 2014). Notably, the parameter  $\varepsilon_m$  was effectively set to 1 in the previous version of Q-GCM, and hence all of the  $E$  coefficients were equal to zero. On the other hand, that previous version had additional parameters  $B$  and  $C$  for radiative corrections associated with the variable AML depth and topography. Here we are back to the model with a constant AML depth (see below); we also neglect topography corrections for simplicity.

Another consequence of the assumption  $\varepsilon_m < 1$  used here is that the coefficients A, D, E in Eq. (13) over ocean and over land are different, and so is the AML temperature equation — the second equation in Eq. (7). In particular, over land we have (neglecting, for now, advection and entrainment terms in the AML equation)

$$\begin{aligned} 0 &= -F_l^\uparrow - F_m^\downarrow - F_s, \\ {}^a\rho {}^aC_p {}^aH_m {}^aT_m &= F_l^\uparrow + F_m^\downarrow - (F_m^\uparrow + {}^aF_m^{e-} + F_1^\downarrow), \end{aligned} \quad (14)$$

Where  $F_l^\uparrow$  is the infrared upward flux from the surface of the land, the latter assumed to have zero heat capacity [hence zero on the left-hand side of the first equation in Eq. (14)] and conductivity (hence  $F_\lambda = 0$ ). From Eq. (14) it follows that over land

$$\begin{aligned} F_l^\uparrow &= -F_m^\downarrow - F_s, \\ {}^a\rho {}^aC_p {}^aH_m {}^aT_m &= -F_s - (F_m^\uparrow + {}^aF_m^{e-} + F_1^\downarrow), \end{aligned} \quad (15)$$

while, in analogy with Eq. (10),

$$F_m^\uparrow = F_l^\uparrow(1 - \varepsilon_m) + D_m^\uparrow {}^aT_m = -(F_m^\downarrow + F_s)(1 - \varepsilon_m) + D_m^\uparrow {}^aT_m \quad (16)$$

[compare this second equation in Eq. (13)]. The first (additional) term in Eq. (16) will also modify all other upwelling radiation fluxes ( $F_1^\uparrow, F_2^\uparrow, F_3^\uparrow$ ) accordingly through Eq. (10), resulting in the modified values of the A and D coefficients and all E coefficients set to zero over land.

Yet another, minor, but potentially fairly important modification of the previous Q-GCM formulation is the inclusion of the dependence on the relative wind speed  $|{}^a\mathbf{u}_m - {}^o\mathbf{u}_m|$  in the bulk formulas for the sensible/latent heat ocean–atmosphere exchange, which plays a

significant role in setting up the North Atlantic SST tripole variability (Deser and Blackmon, 1993; Kushnir, 1994; Czaja and Marshall, 2001; Kravtsov et al., 2007; Fan and Schneider, 2012):

$$F_\lambda = (\lambda + {}^a\rho {}^aC_p C_h |{}^a\mathbf{u}_m - {}^o\mathbf{u}_m|)({}^oT_m - {}^aT_m) \quad (17)$$

[compare with Eqs. (4.7–4.9) in Hogg et al. 2014], where we used the values of  $\lambda = 5 \text{ W m}^{-2}\text{K}^{-1}$  and  $C_h = 0.004$ ; with the typical relative wind speed of  $|{}^a\mathbf{u}_m - {}^o\mathbf{u}_m| \approx 7.5 \text{ ms}^{-1}$  the magnitude of the total sensible/latent heat exchange coefficient in Eq. (17) would be equal to  $35 \text{ W m}^{-2}\text{K}^{-1}$ , which is the value of  $\lambda$  used in the previous edition of Q-GCM (Hogg et al., 2014), along with the value of  $C_h = 0$ .

To complete the mixed-layer heat conservation equations, we need to add advection, diffusion, and entrainment heat fluxes, namely:

$$\begin{aligned} {}^oT_{mt} + ({}^ou_m {}^oT_m)_x + ({}^ov_m {}^oT_m)_y - \frac{{}^oW_{ek} {}^oT_m}{{}^oH_m} &= {}^oK_2 \nabla_H^2 {}^oT_m - {}^oK_4 \nabla_H^4 {}^oT_m \\ &+ \frac{1}{{}^o\rho {}^oC_p {}^oH_m} (-F_\lambda - F_0^\uparrow - F_m^\downarrow - F_s + {}^oF_m^{e+}), \\ {}^aT_{mt} + ({}^au_m {}^aT_m)_x + ({}^av_m {}^aT_m)_y - \frac{{}^aW_{ek} {}^aT_m}{{}^aH_m} &= {}^aK_2 \nabla_H^2 {}^aT_m - {}^aK_4 \nabla_H^4 {}^aT_m \\ &+ \frac{1}{{}^a\rho {}^aC_p {}^aH_m} (F_\lambda + F_0^\uparrow + F_m^\downarrow - (F_m^\uparrow + {}^aF_m^{e-} + F_1^\downarrow)); \end{aligned} \quad (18)$$

compare this with the first two equations in Eq. (7) and with Eqs. (3.28–29) in Hogg et al., 2014.

As mentioned above, in contrast to the previous Q-GCM formulation, we use here the constant mixed-layer thickness in both the ocean and the atmosphere. Therefore, in both the ocean and the atmosphere, entrainment is solely driven by the Ekman pumping. Neglecting vertical diffusion and convection in the present perturbation model (which is another difference from

Hogg et al., 2014), we write for the ocean, following McDougall and Dewar, 1998, Kravtsov et al., 2007:

$$\begin{aligned} {}^oF_m^{e+} &= {}^o\rho {}^oC_p {}^ow_{ek} ({}^oT_1 - {}^oT_m), \quad {}^oF_m^{e-} = 0, \quad \text{if } {}^ow_{ek} > 0 \\ {}^oF_m^{e+} &= 0, \quad {}^oF_m^{e-} = -{}^o\rho {}^oC_p {}^ow_{ek} ({}^oT_1 - {}^oT_m), \quad \text{otherwise;} \end{aligned} \quad (19)$$

cf. Eqs. (4.30–31) of Hogg et al., 2014. The entrainment in the ocean interior only occurs between layers 1 and 2, and is computed in the same way as in the original model:

$${}^oe_1 = \frac{{}^oF_m^{e-}}{\Delta_1^o T} \quad (20)$$

[Hogg et al., 2014, Eq. (4.32)]; following, again, Hogg et al., 2014,  ${}^oe_1$  is also corrected to have zero area integral by adding a spatially uniform offset value at each time step.

Similarly, in the atmospheric mixed layer

$$\begin{aligned} {}^aF_m^{e+} &= {}^a\rho {}^aC_p {}^aw_{ek} ({}^aT_m - {}^aT_1), \quad {}^aF_m^{e-} = 0, \quad \text{if } {}^aw_{ek} > 0 \\ {}^aF_m^{e+} &= 0, \quad {}^aF_m^{e-} = -{}^a\rho {}^aC_p {}^aw_{ek} ({}^aT_m - {}^aT_1), \quad \text{otherwise.} \end{aligned} \quad (21)$$

Here  ${}^aT_1$  is the perturbation temperature given by Eq. (12); in the mean state this temperature is set to  $\overline{{}^aT_m}$ . Using  ${}^aT_1$  instead of  $\theta_1$  in Eq. (19) is what keeps the instability described by Hogg et al., 2003 in check in the present version of the model with constant  ${}^aH_m$ . This is due to the fact that  ${}^aT_1$  is tied to the instantaneous vertical structure of the atmosphere, which limits the magnitude of entrainment heat fluxes (as  ${}^aT_1$  tends to be closer to  ${}^aT_m$  than  $\theta_1$ ) and also provides additional negative feedbacks in the quasi-geostrophic potential vorticity (QGPV) equations via the dependence of entrainment fluxes on  $\eta$ .

Finally, a major modification in the present version of the Q-GCM model is the formulation of entrainment fluxes in the interior of the atmosphere. In the previous version of the model, all entrainment was assumed to occur at the lowest interface, leading to unrealistically small vertical shears of horizontal velocity in the upper atmosphere. Here we correct this by allowing the thermal forcing of the upper troposphere and entrainment through both atmospheric interfaces. The perturbation heat conservation equations for the interior atmospheric layers can be obtained by setting the time derivatives on the left-hand side of the last three equations in Eq. (7) to zero and using the jump conditions (McDougall and Dewar 1998) at the interfaces:

$$\begin{aligned}
0 &= F_m^\uparrow + F_1^\downarrow + {}^a F_m^{e+} - (F_1^\uparrow + F_2^\downarrow + {}^a F_1^{e-}), \\
0 &= F_1^\uparrow + F_2^\downarrow + {}^a F_1^{e+} - (F_2^\uparrow + F_3^\downarrow + {}^a F_2^{e-}), \\
0 &= F_2^\uparrow + F_3^\downarrow + {}^a F_2^{e+} - F_3^\uparrow, \\
{}^a F_k^{e+} - {}^a F_k^{e-} &= -{}^a \rho {}^a C_p {}^a e_k \Delta_k^a T; \quad k = 1, 2
\end{aligned} \tag{22}$$

[compare this with Eqs. (4.10–4.12) of the Q-GCM User’s guide; Hogg et al., 2014]. Adding up the first three equations in Eq. (22) and using the fourth equation for the jump conditions allows one to write

$$\rho {}^a C_p ({}^a e_1 \Delta_1^a T + {}^a e_2 \Delta_2^a T) = F_m^\uparrow + F_1^\downarrow + {}^a F_m^{e+} - F_3^\uparrow \tag{23}$$

Hogg et al., 2014 assumed  ${}^a e_2 = 0$ . We modify this assumption by making the entrainments across the lower and upper atmospheric interface be linearly related, with the coefficient  $f_2$  (see below); this procedure can also be adapted for the use in an  $K$ -layer model by introducing additional free parameters analogous to  $f_2$ . To allow one a degree of freedom in controlling damping rates at each interface somewhat independently, we also introduce here a (small) vertical diffusion, using a linearized version of McDougall and Dewar, 1998 formulation:

$$\begin{aligned}
{}^a e_1 &= {}^a e'_1 + \mu_1^* \left( \frac{1}{{}^a H_1} + \frac{1}{{}^a H_2} \right) {}^a \eta_1 - \frac{\mu_1^*}{{}^a H_2} {}^a \eta_2, \\
{}^a e_2 &= {}^a e'_2 + \mu_2^* \left( \frac{1}{{}^a H_2} + \frac{1}{{}^a H_3} \right) {}^a \eta_2 - \frac{\mu_2^*}{{}^a H_2} {}^a \eta_1, \\
{}^a e'_2 &= f_2 {}^a e'_1
\end{aligned} \tag{24}$$

We can now solve the system Eq. (23) – (24) for the two unknown non-diffusive entrainment rates  ${}^a e'_1$  and  ${}^a e'_2$  and, hence, for the full entrainment rates  ${}^a e_1$  and  ${}^a e_2$ . We use the nominal value of  $0.0001 \text{ ms}^{-1}$  for both of  $\mu_1^*$  and  $\mu_2^*$  and initially set

$$f_2 = \frac{{}^a g'_1}{{}^a g'_2} \tag{25}$$

to ensure generation of similar velocity shears between atmospheric layers 1/2 and 2/3 by the thermal forcing of a given amplitude. Increasing  $f_2$  would tend to increase the geostrophic zonal velocity shear between the lower two atmospheric layers and decrease the velocity shear between the upper two atmospheric layers; setting  $f_2 = 0$  recovers the previous Q-GCM formulation. The optimal value of  $f_2$  is to be determined by trial-and-error tuning of the model.

### 2.3.3 Temperature-dependent flow in atmospheric mixed layer and partially coupled setup

We introduce temperature dependence of the AML winds by modifying the mixed-layer momentum equations in two ways, namely: (i) including, explicitly, temperature driven pressure gradients (which takes into account the mixed-layer hydrostatic adjustment to temperature contrasts: Lindzen and Nigam, 1987), following Feliks et al., 2004, 2007, 2011; and (ii) making the surface drag coefficient depend on the ocean–atmosphere temperature difference to parameterize changes in AML stability (Wallace et al., 1989), following Hogg et al.,



2009; see Small et al., 2008, Chelton and Xie, 2010 and Seo et al., 2023 for a review of these two mechanisms for mesoscale air–sea coupling. Putrasahan et al., 2013 demonstrated that, in the Kuroshio region, both mechanisms (i) and (ii) are important, with relative contributions depending on the spatial scale of the SST anomalies. Putrasahan et al., 2017 also concluded that heat advection by oceanic mesoscale currents plays a key role in creating such SST anomalies and forcing the MABL response in the Gulf of Mexico. To implement these changes, we write the AML momentum equations as:

$$\begin{aligned}
{}^a u_m &= {}^a u_1 + \alpha_T \frac{1}{2} \frac{g {}^a H_m}{\theta_0 f_0} \frac{\partial {}^a T_m}{\partial y} - \frac{{}^a \tau^y}{{}^a H_m f_0}, \\
{}^a v_m &= {}^a v_1 - \alpha_T \frac{1}{2} \frac{g {}^a H_m}{\theta_0 f_0} \frac{\partial {}^a T_m}{\partial x} + \frac{{}^a \tau^x}{{}^a H_m f_0}, \\
({}^a \tau^x, {}^a \tau^y) &= C_D \max(1 + \alpha \Delta T, 0.1) |{}^a \mathbf{u}_m - {}^o \mathbf{u}_m| ({}^a u_m - {}^o u_m, {}^a v_m - {}^o v_m),
\end{aligned} \tag{26}$$

where  $({}^a u_1, {}^a v_1)$  is the geostrophic velocity in the lowest atmospheric layer,  $({}^a \tau^x, {}^a \tau^y)$  is the wind stress,  $\Delta T = T_m^o - T_m^a$ ,  $\alpha_T = 1$  and  $\alpha = 0.15$ . Setting one of the  $\alpha$ -parameters to zero can be used to examine processes (i) and (ii) above independently; setting both of these parameters to zero would recover the previous, temperature-independent AML wind formulation (3.2) – (3.3) of Hogg et al., 2014. On top of these modifications, we also set the drag coefficient over ocean to 2/3 of the default value over land, following Marshall and Molteni, 1993.

Upon adding to Eq. (26) analogous equations for oceanic mixed layer in their original form (Hogg et al., 2014; Eqs. (3.4)–(3.5)), we end up with a closed system of equations for the unknown values of  $({}^a \tau^x, {}^a \tau^y)$  at each grid point, which can be solved analytically in the same way as before (see Hogg et al., 2014). Note that additional temperature gradients in the first two equations in Eq. (26) produce a non-divergent wind field with zero direct Ekman pumping

and, also, zero temperature advection contributions; their dynamical effect is thus purely indirect, via modifications to the wind-stress field; they also generate non-zero moisture advection in the moist version of the Q-GCM model, to be developed later in Chapter 4.

The temperature-dependent AML wind formulation (26) is associated with coupled feedbacks that tend to suppress oceanic turbulence and SST fronts (cf. Hogg et al., 2014; see also Chapters 3 and 5 here). In principle, realistic mesoscale ocean field can still be achieved in inherently more turbulent oceanic regimes at high Reynolds numbers, but this requires very high ocean resolution and is computationally demanding. An alternative fix is to apply partial momentum coupling of the oceanic and atmospheric mixed layers in which the atmosphere “sees” the wind stress as per the full version of Eq. (26), whereas the oceanic wind stress is computed from Eq. (26) in which  $\alpha_T = \alpha = 0$ . In this way the mesoscale feedbacks of temperature-dependent wind, which damp oceanic turbulence, are artificially suppressed, but their effect on the atmosphere is preserved, possibly leading to coupled dynamics involving large-scale low-frequency reorganization of the wind field and the ensuing ocean response.

#### 2.2.4 Lateral boundary conditions for mass and temperature equations

The original Q-GCM formulation employed no-through-flow conditions on the zonal boundaries of the atmospheric channel but effectively allowed the mass to leave/enter ocean mixed layer through side boundaries to avoid Ekman-pumping singularities there (via the direct use of Eqs. (3.5) and (3.18) to compute the oceanic Ekman pumping in Hogg et al., 2014); this means, among other things, that the area integral of Ekman pumping over the ocean basin does not

vanish. Although it is a lesser problem in the atmospheric set up, we modify the computation of the atmospheric Ekman pumping at the zonal boundaries accordingly to achieve a uniform model formulation and also to avoid an abnormal boundary pumping in the atmosphere. To do so, instead of setting  ${}^a v_m$  to zero at the zonal boundaries, we assign it the values computed by the second equation in Eq. (26), with the Ekman pumping computed as usual — in terms of the divergence of the mixed-layer horizontal velocity field — by Eq. (3.16) or, equivalently, via curl of the wind stress by Eq. (3.17) in Hogg et al., 2014).

Naturally, with open boundaries in both the ocean and the atmosphere, we also let the fluid leaving/entering the basin to have temperature determined by the Neumann boundary condition of zero temperature derivative in the direction normal to the boundary:

$$\frac{\partial T_m}{\partial n} = 0, \tag{27}$$

Where  $T_m$  denotes either atmospheric or oceanic mixed-layer temperature. With the open boundary condition augmented by Eq. (27), it is no longer necessary to specify the temperature at the ocean's equatorward boundary, as was done in Hogg et al., 2014.

## Chapter 3

### 3. Experiments with dry Q-GCM

#### 3.1 Experiments with the original Q-GCM modified to include SST-wind feedback

##### 3.1.1 Diagnosing the effects of temperature-dependent wind-stress parameterizations in high-resolution coupled Q-GCM simulations

Feliks et al., 2004, 2007, 2011 and Brachet et al., 2012 examined the response of the atmosphere to mesoscale sea-surface temperature (SST) anomalies through hydrostatic pressure adjustment in an idealized atmospheric model. They showed that resolving an ocean front and mesoscale eddies affects atmospheric climatology, intraseasonal modes, as well as decadal variability (when forced with the observed SST history) in their model (see also Nakamura et al., 2008). By modifying the atmospheric mixed-layer momentum equation, we included Feliks et al. parameterization of the SST-dependent ABPL boundary winds (see Section 2.3.3; Eq. (26), with  $\alpha = 0$ ) in the Q-GCM model. The SST front will tend to induce a similar front in the APBL temperature distribution, which will produce temperature-dependent wind stress and the associated pumping, forcing the oceanic and atmospheric QG interiors.

Another way of incorporating the mesoscale SST effects on air–sea coupling dynamics is by including SST dependence in the wind-stress drag coefficient, following Hogg et al., 2009 (see Section 2.3.3; Eq. (26);  $\alpha_T = 0$ ). This effect may be present physically in the real world too, but here its magnitude is substantially augmented to correspond, quantitatively, to the observed response of APBL winds to SST fronts (see below). Here, again, the temperature-dependent

wind stress would produce large Ekman-pumping anomalies over mesoscale SST features (and the associated forcing of the circulation in the interiors of both fluids).

We first performed the comparison of the two types of TDWS parameterization in the high-atmospheric-resolution coupled experiments described in more detail below (Section 3.1.2), by estimating the effect of SST gradients on the model's APBL winds. A number of studies have shown a linear correlation between the observed downwind (cross-wind) SST gradients and wind-stress divergence (curl) (Chelton et al., 2001; O'Neill et al., 2003; Chelton et al., 2004; O'Neill et al., 2005).

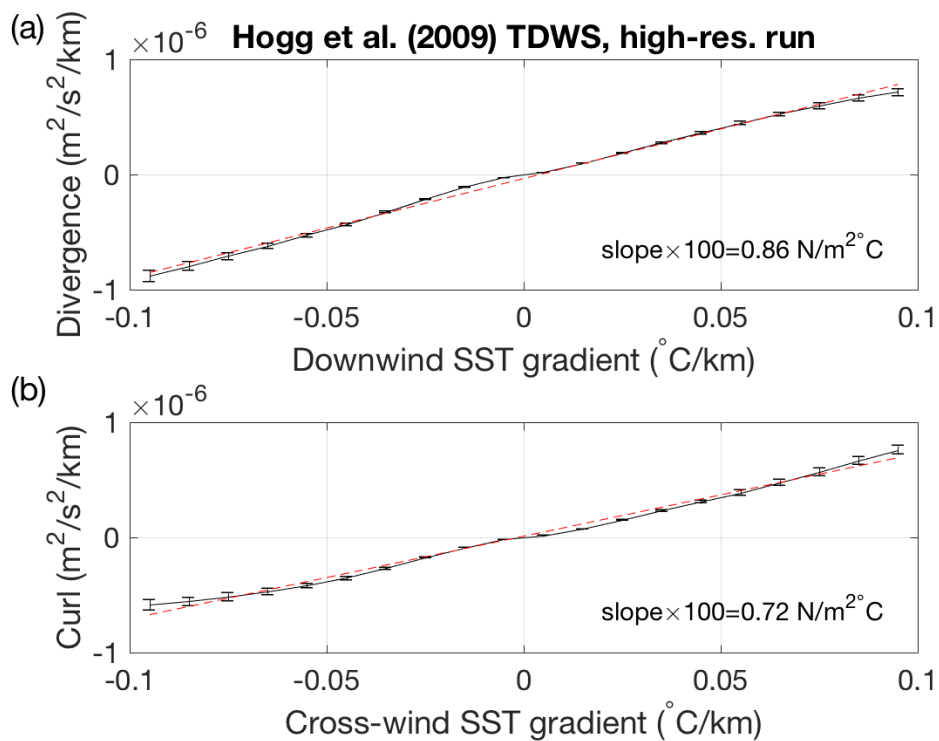


Figure 2 - Downwind (upper plot) and Cross-wind (bottom plot) SST gradient from Hogg et al., 2009 TDWS run.

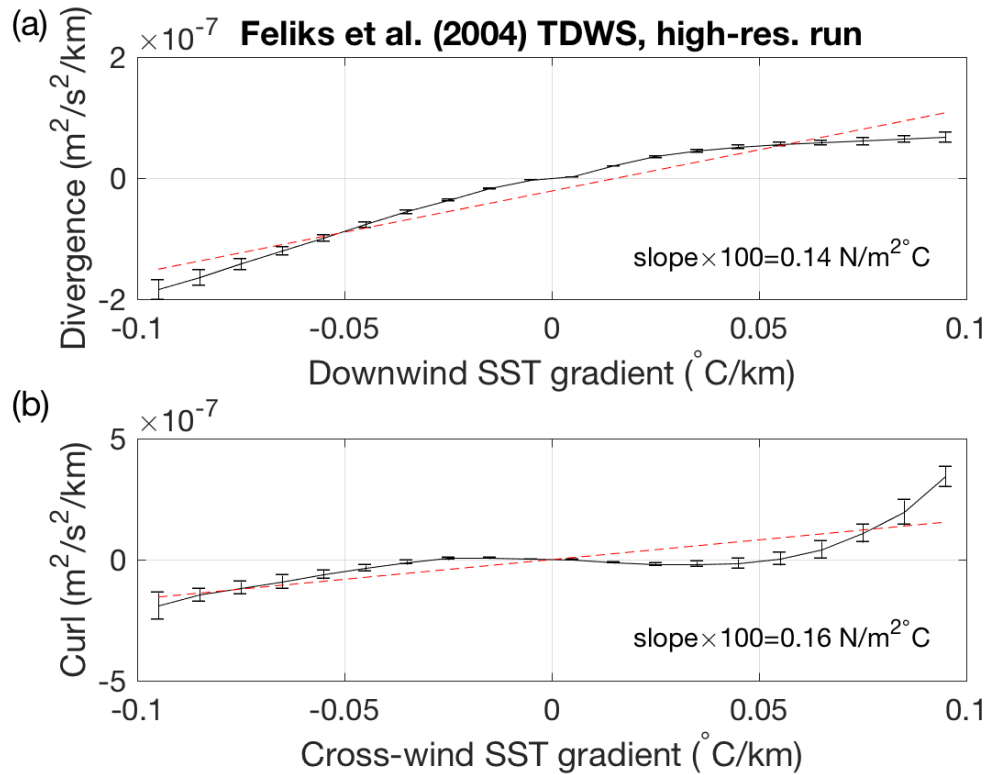


Figure 3 - Downwind (upper plot) and Cross-wind (bottom plot) SST gradient from Feliks et al., 2004 TDWS run

We computed these dependencies following the procedure established by Chelton et al., 2001 and adopted by Hogg et al., 2009 for Q-GCM simulations. Here we used 150-yr output of the high-atmospheric resolution (20-km) simulations with Hogg et al., 2009 (Figure 2) and Feliks et al., 2004 (Figure 3) TDWS parameterizations. In particular, we divided the data into 10-yr segments, spatially filtered to concentrate on mesoscale anomalies, and used the downwind (crosswind) temperature gradient at each data point to divide the wind stress divergence (curl) into bins and find the average within each bin. The same procedure applies to each 10-yr segment, after which the mean and standard deviation of the 15 segments can be found. The resulting dependencies from the simulation with Hogg et al., 2009 parameterization bear

striking qualitative and quantitative similarity with observations, which manifest linear relationships with similar slopes (for example, the slope of the divergence plot is 0.86, compared to 0.96 for the Kuroshio and 1.09 for the Gulf Stream; Chelton et al., 2004). On the other hand, these dependencies in the simulation with Feliks et al., 2004 TDWS parameterization are nonlinear and much too weak. This is, perhaps, due to the fact that the hydrostatic pressure adjustment (Feliks et al.'s parameterization) and APBL stability modifications (Hogg et al.'s parameterization) are most effective for perturbations of different spatial scales (Putrasahan et al., 2013; see Section 1.2.1); we didn't explore this possible scale dependence here, but simply retained both types of parameterizations in the final version of our modified coupled model.

### 3.1.2 Comparing the simulations with and without temperature-dependent APBL wind

We performed multi-century model simulations in the double-gyre configuration mimicking the North Atlantic setup, fixing the ocean resolution at 10 km and varying atmospheric resolution from 120 km in the coarse-resolution runs to 20 km in the high-resolution runs (horizontal viscosities and diffusivities adjusted accordingly to provide numerical stability). The high-resolution experiments were motivated by the results of Feliks et al., 2004, 2007, who argued that the mesoscale-resolving atmosphere would have a much-amplified response to the mesoscale SST gradients. First, we ran twin coarse-resolution experiments with (hereafter TDWS) and without (hereafter Control) temperature-dependent wind stress. Then we repeated these experiments in the model with a high-resolution (20 km) atmosphere (the results below

were reported at the 2019 European Geosciences Union meeting: Mastilovic and Kravtsov, 2019).

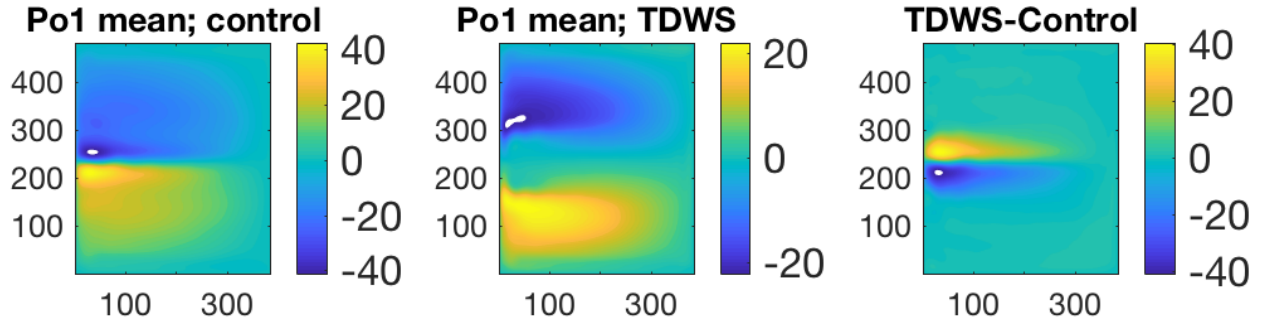


Figure 4 - Oceanic streamfunction climatology (Sv) of control (left plot), TDWS (middle plot) and the difference between Control and TDWS simulations (right plot); coarse resolution

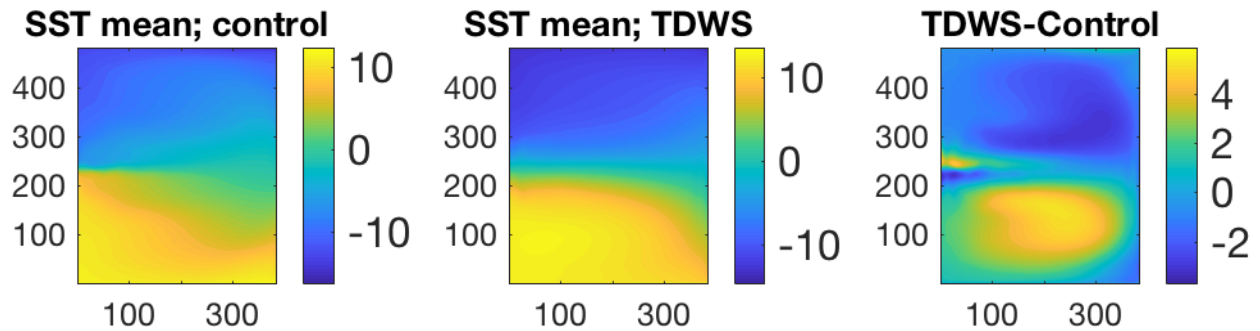


Figure 5 - SST climatology [anomaly with respect to the reference temperature] (K) of Control (left plot), TDWS (middle plot), and the difference between Control and TDWS simulations (right plot); coarse resolution

We start by comparing the experiments with and without TDWS parameterization of the model configuration with a low-resolution atmosphere. Shown here is the climatology of oceanic streamfunction (Sv) (Figure 4) and SST (degrees K) (Figure 5) in both runs, as well as their difference. The mesoscale air–sea coupling (with Feliks et al. parameterization in this case) leads to weaker oceanic turbulence resulting in a quite different oceanic climatology compared to the control run. In particular, the pronounced inertial recirculations evident in the control run are damped in the TDWS simulation, along with the associated SST front. Large-scale north–south



SST gradients in the TDWS run are, however, stronger. These results are consistent with previous work: **mesoscale perturbations in SST will affect the atmospheric winds, which in turn feed back onto the ocean through perturbation heat fluxes** (e.g., Nonaka and Xie, 2003; Xie, 2004; Jin et al., 2009) and Ekman pumping (Stern, 1965; McGillicuddy et al., 2007; Dewar and Flierl, 1987; Maloney and Chelton, 2006; Gaube et al., 2013, 2015; Chelton, 2013; Small et al., 2014). This feedback is negative, as it tends to reduce the intensity of the oceanic mesoscale perturbations that generated the wind anomalies in the first place. Hogg et al., 2009 speculated that the TDWS effect on oceanic eddy activity is indirect and occurs via modifications in the western boundary current stability characteristics.

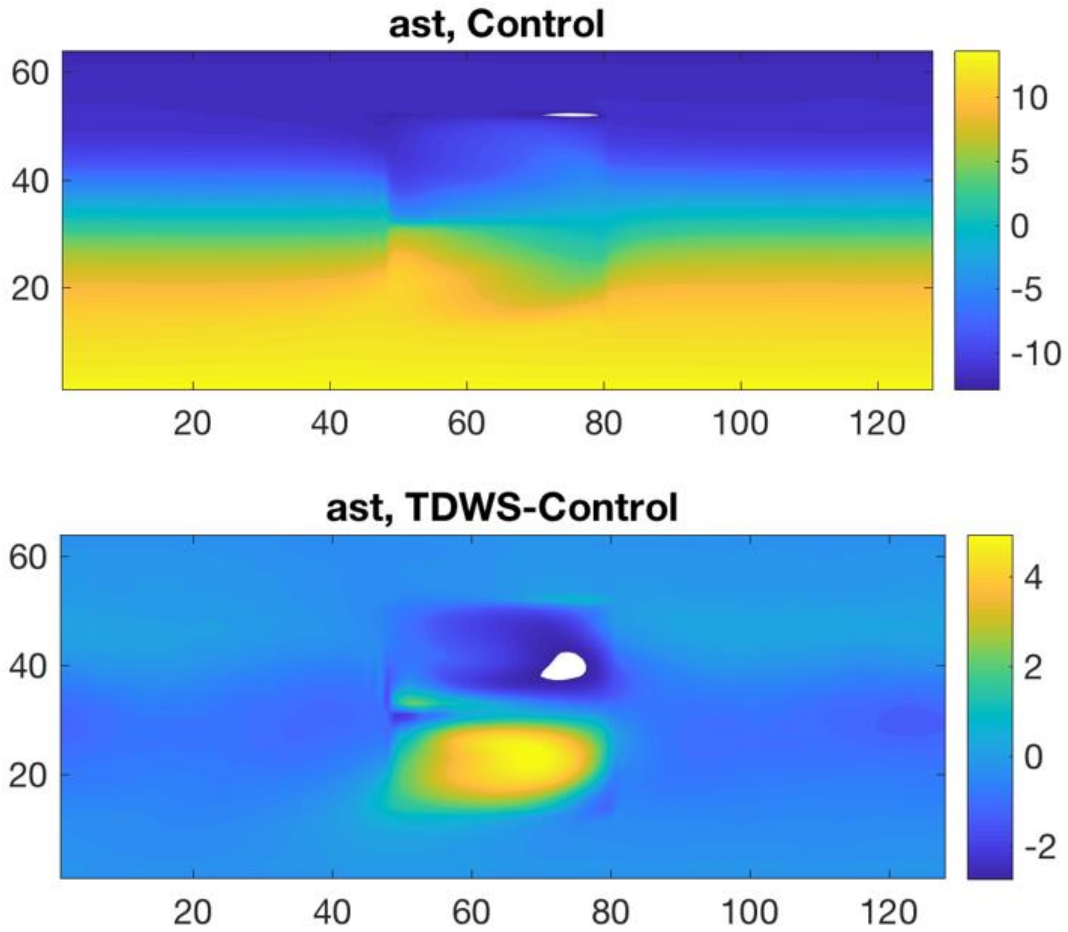


Figure 6 – ATS climatology (K) of control run (upper plot) and AST climatology differences (K) between TDWS and Control runs.

Substantial changes in the atmospheric surface temperature (AST) climatology also arise (Figure 6, bottom panel), consistent with oceanic circulation and SST changes. Enhanced large-scale N-S AST gradient also leads to a stronger climatological jet (not shown).

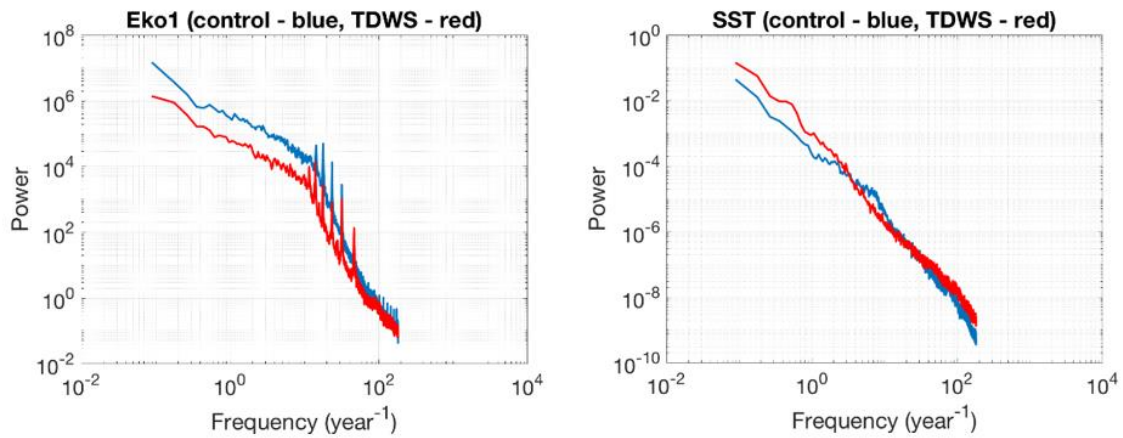


Figure 7 - Oceanic Kinetic Energy (left panel) and SST variability (right panel); Control – blue, TDWS – red.

Ocean kinetic energy (Figure 7, left panel) is lower in the TDWS run, consistent with muted mid-latitude ocean jet and suppressed overall ocean turbulence. However, the low-frequency SST variability (Figure 7, right panel) in the TDWS run is enhanced! This enhancement is due to a fundamental change in the character of the atmospheric low-frequency variability in the simulation with temperature-dependent currents in the atmospheric mixed layer (TDWS simulation; see below).

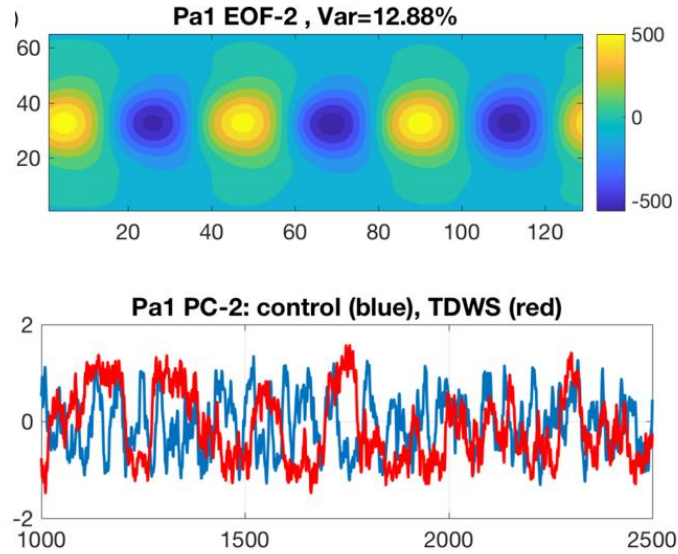


Figure 8 - Second EOF of the first atmo layer streamfunction (upper panel) and PC timeseries associated with the lower-layer streamfunction EOF-2

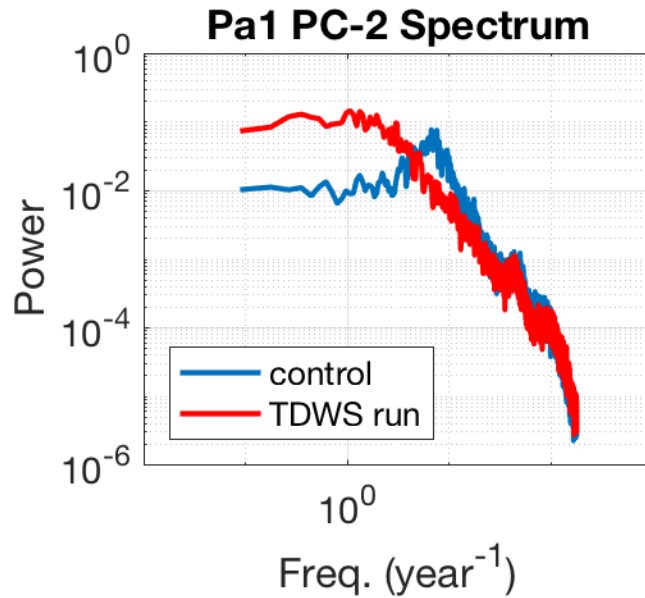


Figure 9 - PC-2 Spectrum

The changes in the atmospheric variability between control and TDWS runs are dominated by the behavior of the wave-3 EOF pair (Figure 8, upper panel). Evident are persistent switches of this mode's PC time series between different regimes (Figure 8, lower panel), which results in

much more intermittency and a low-frequency spectral enhancement in the TDWS run (Figure 9).

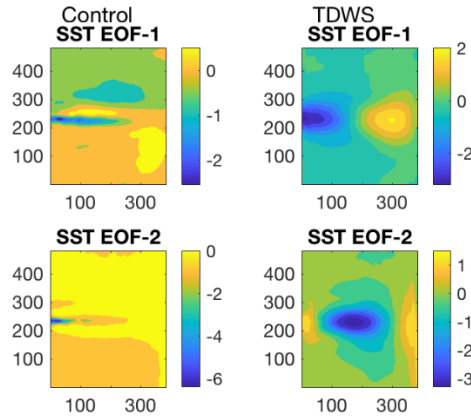


Figure 10 - EOF-1 (top row) and EOF-2 (bottom row) of SST from the Control (left column) and TDWS coupled simulation (right column)

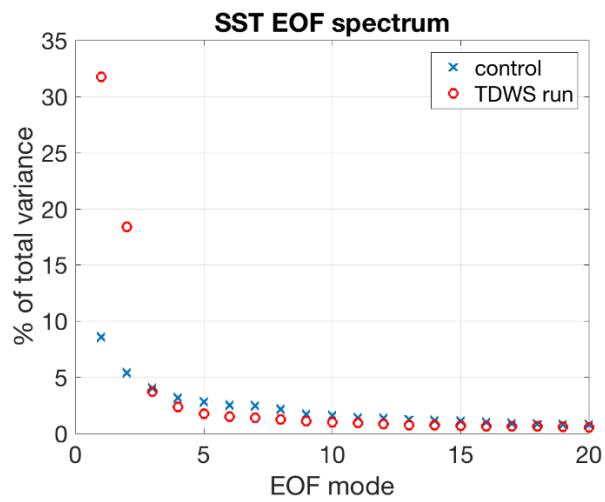
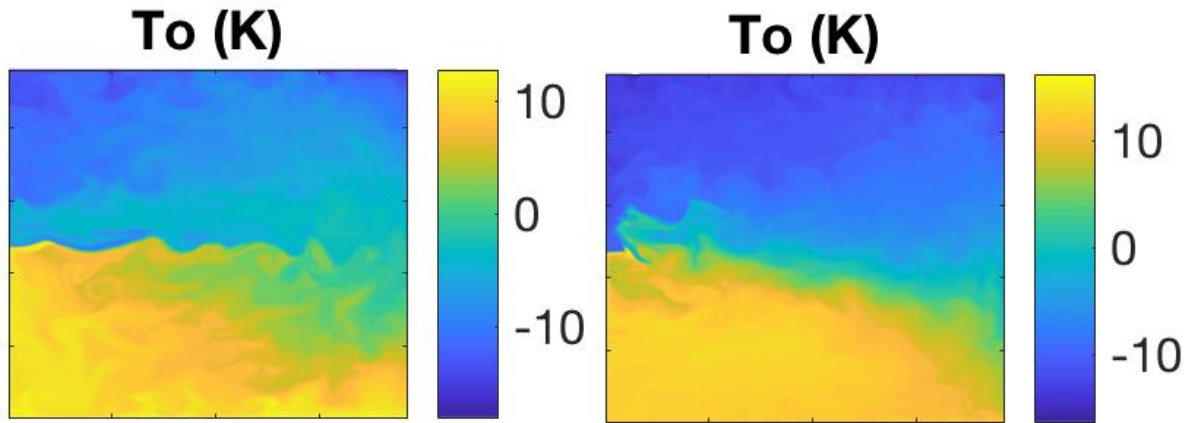


Figure 11 - Fraction of variance accounted for by SST EOFs in the Control (blue) and TDWS (red) coupled simulations.

Control run's SST EOFs (Fig. 10, left) are dominated, once again, by eddies around the climatological jet, while the leading EOFs of the TDWS run (Fig. 10, right) reflect, most likely, large-scale response to atmospheric anomalies. In particular, EOFs 1 and 2 (which sharply dominate the EOF spectrum in TDWS run; see Fig. 11), are clearly forced by the intermittent low-frequency wavenumber-3 patterns identified in Fig. 8, upper panel. The enhancement of the lower-frequency atmospheric variability in the TDWS run is thus not associated with the more efficient transfer of the ocean-induced low-frequency anomalies to the atmosphere, but rather with the combination of SST memory and atmospheric nonlinear dynamics leading to the emergence of low-frequency regime transitions associated with the wave-3 atmospheric mode.

Furthermore, analogous experiments with 20-km-resolution atmosphere produced behavior essentially identical to that in the corresponding runs with coarse-resolution (120-km) atmosphere. This was to be expected for the control experiment w/o TDWS parameterization, in which the Ekman pumping from APBL does not 'see' mesoscale SST gradients. On the other hand, in the coupled experiment that included the Feliks et al. TDWS parameterization, one possible reason for the absence of the mesoscale SST effect onto the atmospheric variability is the damping of oceanic turbulence and SST fronts by the mesoscale air-sea coupling, as per the discussion in Chapters 1 and 2.



*Figure 12 - SST snapshot from Control run (left) and TDWS run (right)*

Indeed, typical snapshots of SST from the control run (Figure 12, left panel) and TDWS run (Figure 12, right panel) demonstrate the lack of pronounced SST fronts in the latter experiment. Reduced and disorganized mesoscale SST gradients preclude the effective mesoscale communication between APBL and overlying free atmosphere even in the experiments with the high-resolution atmosphere.

The results of the experiments with an alternative ad-hoc TDWS parameterization of Hogg et al., 2009 produced similar results with regards to mesoscale air–sea coupling. This parameterization was also characterized by dynamical feedbacks onto the oceanic mean circulation and variability that damped the oceanic turbulence and SST fronts (not shown). In this case, however, there is also no amplification of nonlinear atmospheric variability due to the inclusion of temperature dependence in the atmospheric boundary-layer dynamics (as in the runs with Feliks et al. parameterization), and the atmospheric mean state and variability of the coarse-atmosphere resolution experiments with and without TDWS are very similar. Damping of ocean eddies and

SST fronts leaves no way for mesoscale air–sea coupling to become more important in the high-atmospheric-resolution experiments and, indeed, the variability in these runs is essentially the same with that in the corresponding coarse-atmospheric-resolution experiments.

**These results and observations eventually led us to adopt an ocean model configuration with a higher ocean resolution (of 5 km) and lateral (mixed) boundary conditions closer to the free-slip set up (following Martin et al., 2020); they also prompted the development of the partially coupled set up in the modified Q-GCM model (Section 2.3.3).** Both modifications were meant to enhance the oceanic turbulence and, simultaneously, eddy-driven jet coherence, to result in persistent oceanic jet shifts as the leading mode of oceanic variability (cf. Berloff and McWilliams, 1999a). **However, neither of these modifications resulted in the principal changes in the *free-atmosphere's* low-frequency variability between the control, TWDS and partially coupled simulations of the modified dry version of the Q-GCM model, irrespective of the atmospheric resolution,** which led to the development of the moist version of the Q-GCM model — MQ-GCM in Chapter 4.

We are not showing the results of the above coupled ‘dry’ coupled experiments here, as they turned out to be qualitatively similar to those with MQ-GCM version of the model, whose simulations are described and visualized in detail below in Chapter 5. Instead, we focus, in Sections 3.2 and 3.3 below, on the atmosphere-only experiments (with a modified version of dry Q-GCM model that includes the full TDWS parameterization) forced by zonally uniform SST fronts of different sharpness and position, to better understand the potential atmospheric modifications and responses to such forcing and the reason for the absence of an appreciable response like that in the coupled experiments.



## 3.2 Bimodal behavior in the atmosphere-only modified dry Q-GCM configuration

The results of the coupled experiments above with the original Q-GCM version augmented by the TDWS parameterization alluded to the presence, in the model dynamics, of nonlinear phenomena such as multiple atmospheric regimes characterized by persistent anomalies of the atmospheric state distinct from climatology. Such phenomena were documented before in the atmospheric models and observations (Koo et al., 2002; Kravtsov et al., 2005, 2006) and include the regimes characterized by the existence of two preferred states of the zonally averaged mid-latitude atmospheric jet displaced to the south and to the north of the climatological jet-axis location. In the probability density function (PDF) of the time series of the jet's instantaneous locations, these states manifest as the PDF's bimodality (the presence of two local maxima in the locations associated with the two regimes). **Such bimodality was not found** in the original version of the Q-GCM model (Andy Hogg, personal communication) although it was documented in a similar coupled QG setups by Kravtsov et al., 2005, 2006. We were excited to notice that the modified dry version of the Q-GCM model's atmosphere did exhibit the bimodality and spent quite a bit of time exploring the nonlinear sensitivity of this model (in atmosphere-only configuration) to the SST-front forcings. However, we will show below that the Q-GCM bimodality is not as pronounced and robust as in the Kravtsov et al., 2005, 2006 (two-layer QG model) studies and, most importantly, appears to die out in the experiments with higher atmospheric resolution, thus being, most likely, an artifact of under-resolving the Rossby radius in the low-resolution Q-GCM version. The hypothesis of possible nonlinear

sensitivity of Q-GCM atmosphere to SST-front-type forcing has thus been rejected (or, rather, the null hypothesis that the Q-GCM atmosphere is sensitive to such forcings couldn't).

Kravtsov et al., 2008 found that the bimodal behavior of the atmospheric jet in QG models may be important in the context of coupled ocean–atmosphere behavior in middle latitudes, as it amounts, in their studies, to nonlinear sensitivity of the atmosphere to small (in magnitude or spatial scale) SST perturbations in the situations where these anomalies lead to changes in the attractor basins and regime populations. Studying nonlinear phenomena such as atmospheric jet's bimodality requires long experiments and may be challenging and time-consuming at high model resolutions. Here, we performed an extensive set of experiments in order to investigate these phenomena in the Q-GCM as a function of the model's parameters including the SST-front sharpness and magnitude, drag coefficient, mean radiative forcing, and radiation perturbation magnitude. All experiments were done in the atmosphere-only configuration with and without TDWS parametrization; each experiment produced a 70-year-long atmospheric simulation at a daily sampling rate after a 10-year spin-up period.

We computed the daily jet position time series by locating the maximum of the zonal-mean zonal wind in the middle atmospheric layer. We also computed the leading PC of this layer's 2-D streamfunction; the two time series (of jet-position location and the leading EOF of the middle-layer streamfunction) are typically well correlated and lead to a similar diagnosis of the bimodality in its PDF. After some initial parameter and resolution sensitivity analysis, we found that the most prominent bimodality favors coarse resolution (120km), cold atmosphere (lower mean radiative forcing), higher equator-to-pole radiation contrast, lower drag coefficient values, as well as stronger sharpness and magnitude of the SST front.

However, since lower mean radiative forcing is associated with the unrealistically cold mean state of the atmosphere, while higher radiation contrast causes unrealistically strong wind, we restricted our parameter range somewhat to ensure the model exhibits realistic atmospheric mean-state conditions. In doing so, we documented bimodality in a dry model as a function of drag coefficient ( $C_D$ ) and the magnitude of the north–south insolation contrast ( $F'_s$ ), using the mean radiation forcing equal to  $\bar{F}_s = -240 \text{ W m}^{-2}$ . The experiments are performed with  $Cd = 1e - 3, 0.5e - 3$  and  $Fs' = 125, 135, 145, 150, 175 \text{ W m}^{-2}$ , with 4 different SST fronts (Figure 13), under the coarse and then high atmospheric resolutions.

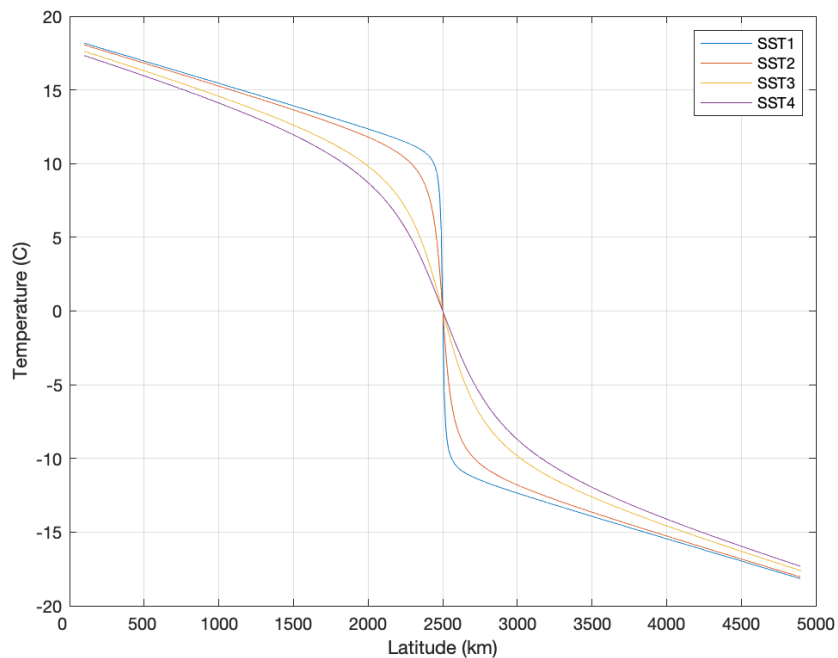


Figure 13 – Zonally uniform SST-front distributions used in the bimodality detection experiments.

Strongly non-Gaussian (bimodal or at least strongly skewed) PDFs were found for sufficiently high values of equator-to-pole radiative contrast ( $Fs'$ ), starting with the value of  $125 \text{ W/m}^2$

and higher, progressively more so for higher values of  $Fs'$  (not shown). Below we present the results from simulations with this parameter equal to  $175 \text{ W/m}^2$  and the drag coefficient set to  $0.5 \times 10^{-3}$  as the simulation with the most prominent bimodality. A more complete set of model parameters used in these experiments is listed in Table 5.

*Table 5 - Atmospheric parameters used in the experiments on identification of bimodality of Section 3.2*

<b>PARAMETER</b>	<b>VALUE</b>	<b>DESCRIPTION</b>
$C_D$	$0.5 \times 10^{-3}$	Drag coefficient
${}^aA_4$	$2 \times 10^{14} \text{ m}^4/\text{s}$	Biharmonic viscosity coefficient
${}^aK_2$	$2.7 \times 10^4 \text{ m}^2/\text{s}$ (30 and 40km)	Temperature diffusion coefficient
${}^aK_4$	$3 \times 10^{14} \text{ m}^4/\text{s}$	4th order diffusion coefficient
$K_\eta$	$2 \times 10^5 \text{ m}^2/\text{s}$	Diffusion coefficient
$Fs'$	$175 \text{ W/m}^2$	North-south contrast of insolation

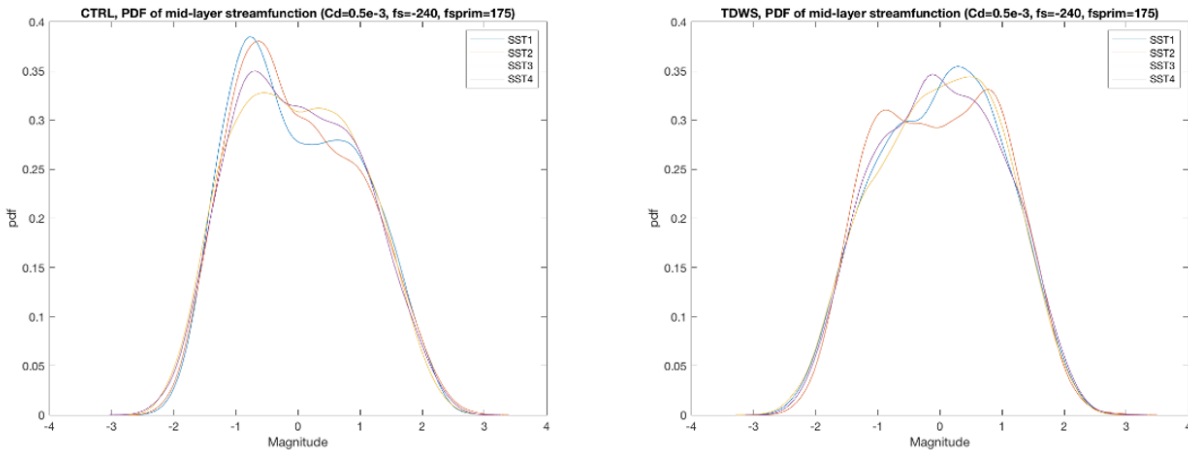


Figure 14 - PDF of mid-layer streamfunction as a function of SST-front magnitude. (a) Left: CTRL simulation; (b) right: TDWS simulation. different colored curves in each panel correspond to 4 different magnitudes of SST front (see Fig. 17), with SST1 denoting the strongest front and SST4 – the weakest front.

The most pronounced bimodality is found in the CTRL simulations (Fig. 14, left panel); this bimodality is, in turn, the strongest in the simulations with the strongest north–south SST contrasts. The bimodality in the TDWS simulations seems to also be present but is less robust than that in the CTRL simulations both in terms of the exact shape of the PDF and the sensitivity to the strength of the SST front (Fig. 14, right panel).

Furthermore, the bimodality disappears in the high-resolution (20km) experiments, with the PDFs of CTRL and TDWS simulations apparently insensitive to the magnitude of the SST front even in the experiments with large values of  $F_s'$  (not shown). The parameters of the high-resolution and coarse-resolution simulations were identical except for a lower value of horizontal superviscosity in the high-resolution simulation needed to conduct this simulation with as large time step as possible for numerical efficiency. To check whether this difference can explain the lack of bimodality in high-resolution experiments, we ran simulations with the 30-km and 40-km resolutions (Figs. 15 upper left and upper right plots) and kept the same

diffusivity values as in the coarse resolution (which required tiny time steps to achieve a stable simulation), then compared the results with those from the coarse-resolution simulation (Fig. 15 bottom left panel). In the experiments above, the same set of parameters was used in both high (30 and 40 km) and coarse resolution (120 km) except for the time step (which was larger in the coarse-resolution simulation). To confirm that the time step of the coarse resolution does not affect the bimodal regime, we also ran coarse-atmospheric resolution experiments with the tiny time step used in the 30-km-resolution simulation (Fig. 15 bottom right) and get the results identical with those of the larger time step coarse-resolution run (Fig. 15 bottom left).

The results in Fig. 15 show that the bimodality found in the coarse-resolution simulation of the atmospheric component of the Q-GCM model is an artifact of the excessively coarse resolution due, most probably, underresolved atmospheric Rossby radii (in the 120-km simulation we only have 2–3 points per either Rossby radius), as the bimodality disappears in the experiments with increased resolution under, otherwise, the completely identical set of model parameters. Therefore, there is no evidence of physical (rather than numerical) nonlinear sensitivity of the atmospheric component of the Q-GCM model to the details of the SST front in this model, at least for the parameter settings used here. This, of course, does not rule out the possibility of such behavior in different models and different parameter settings (cf. Kravtsov et al., 2005, 2006).

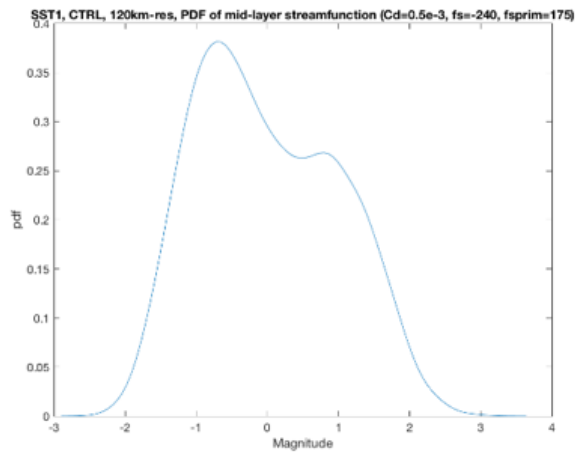
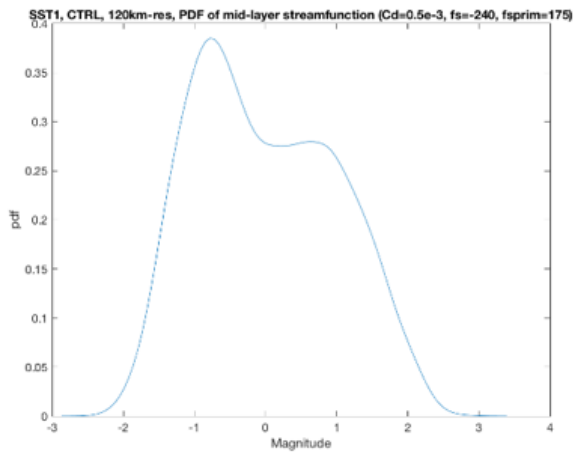
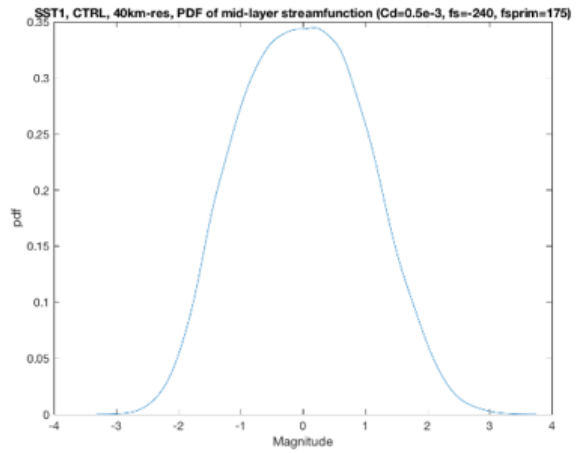
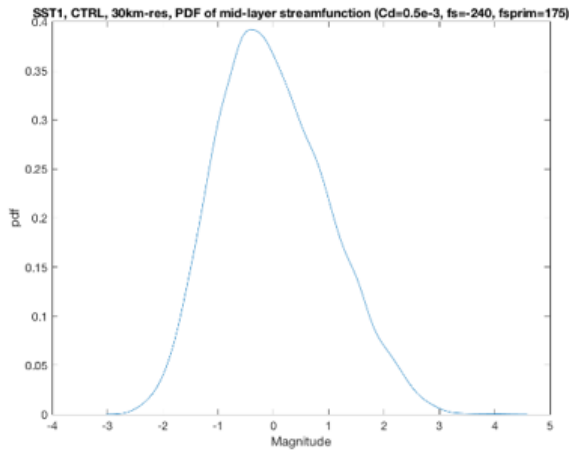


Figure 15 - PDF of the leading PC of mid-layer streamfunction in the simulation forced by the strongest SST front at the drag coefficient set to  $C_d=0.5e-3$  and equator-to-pole radiative contrast of  $f_s'=175W/m^2$ : (a) top left – 30 km resolution (b) top right – 40 km resolution; (c) bottom left – 120 km resolution; (d) bottom right – 120 km resolution [the same as (c)], but with the (tiny) time step of the 30-km-resolution simulation.

### 3.3 Sensitivity of the Q-GCM atmosphere to the permanent SST-front displacements

Motivated by the lack of any clear detectable effect of mesoscale air–sea coupling (through temperature dependent wind stress) on the circulation of the model’s free atmosphere, even under our modified dry Q-GCM formulation of Chapter 2 at both coarse (120 km) and high (20 – 40 km) horizontal resolutions, we performed a set of experiments to check the model’s sensitivity to the meridional position of the SST front, following Deremble et al., 2012. These authors, in experiments with a similar setup, although without the explicit APBL model, argued that it is the position of the SST front anchors the atmospheric jet at the corresponding latitude. Our documented insensitivity of the model’s atmosphere to the mesoscale air–sea coupling is in apparent contrast with these arguments, but we will argue below that our results are in fact consistent with theirs.

We used several SST fronts but only show the results for the stronger front (Figure 16), as no significant differences in the atmospheric variability were found between the cases with weaker and stronger SST fronts. The front location was fixed either in the middle of the ocean (Fig. 16 left plot; hereafter, the default configuration) or was displaced 1000 km to the south with respect to that in the default configuration (Fig. 16 right plot; hereafter, shifted configuration). We used 60 km and 120 km horizontal resolution with or without TDWS parameterization and showed that in all simulations, the free-atmosphere climatological-jet position is strongly attracted to the location of the SST front, irrespective of how sharp the front itself is.



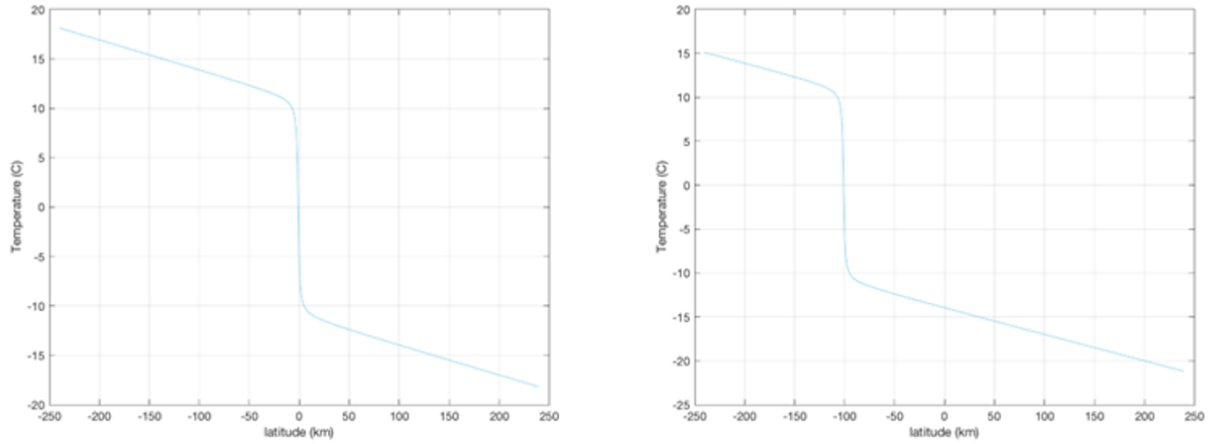


Figure 16 – Cross section of the idealized SST fronts along  $y$  axis used to force atmosphere-only Q-GCM sensitivity experiments. (a) Left: default configuration, with the front located in the middle of the ocean; (b) Right: shifted SST-front configuration, with the front located 1000 km to the south of the default position.

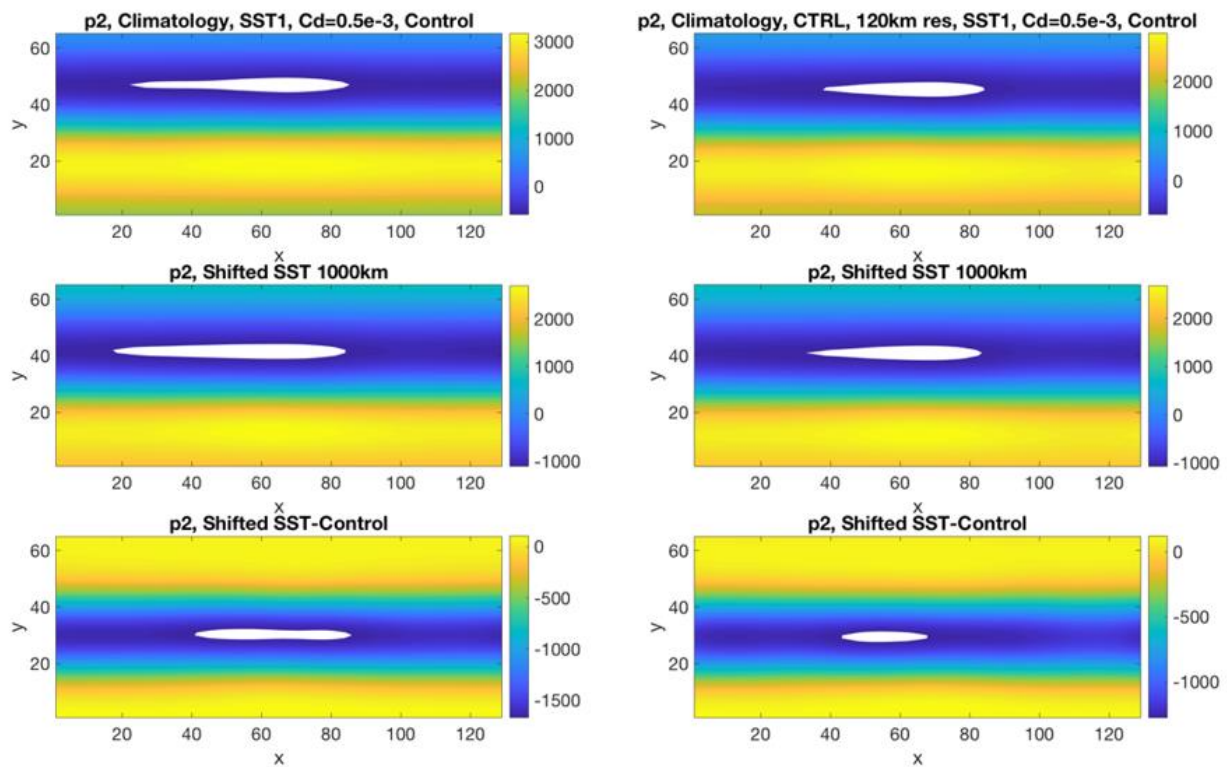


Figure 17 - Climatology of the mid-layer atmospheric dynamic pressure ( $m^2/s^2$ ) from the experiment forced by the default SST front (top), shifted SST front (middle) and the difference between the two (bottom). Left: the results from the 60-km resolution experiment; right: 120-km-resolution experiment. The  $x$  and  $y$  axes show grid points at the 120 km spacing in both cases.

An example of the control simulation (the one without temperature-dependent AML winds) is shown in Fig. 17. In both high- and coarse-horizontal-resolution runs, the atmospheric jet shifts to the south in response to the permanent displacement of the SST front, with somewhat greater anomalies generated in the higher-resolution experiments. Similar jet displacement also occurs in the other two atmospheric layers both with and without TDWS parametrization (not shown). Furthermore, the atmospheric variability around the climatology is statistically identical in each of the simulations conducted, aside from the meridional shift of the center of actions of this variability in accordance with a climatological jet position in a given simulation (not shown).

Thus, the radiation/heat exchange anomalous forcing of the atmosphere by the meridionally shifted fixed SST front is indeed sufficient to induce the permanent shift of the free-atmosphere jet towards the SST front (cf. Deremble et al., 2012), but this repositioning is due to large-scale heat-flux forcing redistribution, rather than the dynamical response of the AML winds to (mesoscale) SST anomalies. Hence, if one is to look for potential coupled decadal modes of midlatitude ocean–atmosphere variability, one must ensure that the ocean model is able to produce and maintain persistent meridional shifts of the western boundary currents’ eastward-jet extensions — something that can be expected in highly turbulent oceanic regimes (e.g., Berloff and McWilliams, 1999a). This clearly doesn’t happen in the relatively coarse-resolution 10-km ocean component of the coupled Q-GCM discussed thus far, prompting us to eventually adopt a more turbulent 5-km-resolution model version (Martin et al., 2020); Chapter 5.

On top of that, we still didn't detect any pronounced changes in the free-atmosphere variability in the simulations under coarser and higher atmospheric resolutions. This is different from the results of Feliks et al., 2004, 2007 for their idealized atmosphere forced by the Ekman pumping anomalies proportional to the Laplacian of SST (a theoretical expression for the effect of the hydrostatic pressure adjustment on the winds in the atmospheric boundary layer with temperature slaved to SST). In essence, compared to their model, our atmospheric mixed layer (with temperatures more independent of SST) doesn't appear to produce a sufficiently strong Ekman pumping of the atmospheric interior in the vicinity of the SST front. We hypothesize that a much stronger effective local communication between the surface and free atmosphere would be achieved in a moist version of the model, where the latent heat release is associated with the entrainment of moist AML air into the atmospheric interior would prompt substantially larger entrainment fluxes between interior atmospheric layers and, therefore, a much larger free-atmosphere response. Such a moist version of the Q-GCM model is thus developed next in Chapter 4.

## Chapter 4

### 4. Moist Quasi-Geostrophic Coupled Model (MQ-GCM) formulation

#### 4.1 Development of Moist Quasi-Geostrophic Coupled Model

The most important change to the original Q-GCM formulation is the inclusion of the hydrological cycle and latent-heat feedbacks, resulting in what we refer to as the Moist Quasi-Geostrophic Coupled Model (MQ-GCM). Indeed, Czaja and Blunt, 2011 proposed that the oceans can influence the troposphere through moist convection over the regions with strong mesoscale variability; see also Willison et al., 2013. To compute moisture variables in the model, we assume that the vertical temperature profile at a given  $(x, y)$  location is linear in  $z$ , temperature decreasing with altitude  $z$  above the sea level at the critical lapse rate:

$$T_k(z) = {}^a\overline{T}_m - (\Gamma_d - \gamma_c) \frac{{}^aH_m}{2} + {}^aT_k - \gamma_c z \quad (28)$$

Here  $T_k$  is the absolute temperature (in K) in layer  $k$  [ $k$  can be a symbol ( $m$ ) when referring to the AML temperature or an index ( $k=1, 2, 3$ ) when denoting the interior (quasi-geostrophic) layers of the atmospheric model], while  ${}^aT_k$  in the interior are given by Eq. (12). In such a constant-lapse-rate atmosphere, the pressure  $p(z)$  is related to temperature as

$$p(z) = p_0 \left( \frac{T(z)}{T(0)} \right)^{\frac{g}{R\gamma_c}}, \quad (29)$$

where  $g$  is the gravity acceleration and  $R$  is the ideal gas constant for dry air. Combining the latter two equations and the ideal gas law  $p = \rho RT$  at the basic state with  ${}^aT_k = 0$ , we can compute the representative densities of each layer by estimating them at the altitude  $z$  corresponding to the mid-layer height (e.g.,  $z = {}^aH_m/2$  for the mixed layer,  $z = {}^aH_m + {}^aH_1/2$  for layer 1, etc.); this gives, for the parameters in Table 1 and  $p_0 = 10^5 \text{ hPa}$ ,  $(\rho_m, \rho_1, \rho_2, \rho_3) = (1.16, 1, 0.77, 0.52) \text{ kg m}^{-3}$ . The saturation specific humidity  $h_s$  is given by

$$h_s = \varepsilon \frac{e_s}{p}; \quad e_s = e_o \exp\left(\frac{a(T - T_0)}{b(T - T_0) + T_r}\right), \quad (30)$$

where  $\varepsilon = R/R_v = 0.62$  is the ratio of the dry-air and water-vapor gas constants and the saturation water vapor pressure  $e_s$  is computed as in Bolton, 1980, using the parameters  $e_o = 611.2 \text{ hPa}$ ,  $a = 17.67$ ,  $b = 1$ ,  $T_r = 243.5 \text{ K}$  and  $T_0 = 273.5 \text{ K}$ . Given the AML perturbation temperature  ${}^aT_m$  and the atmospheric interface displacements  ${}^a\eta_1, {}^a\eta_2$  the Eq. (12), (28)–(30) can be used to compute the saturation specific humidity as a function of  $z$  at every grid point ( $x, y$ ) and within each atmospheric layer  $k = (m, 1, 2, 3)$ .

The moist version of the Q-GCM model has, compared with the original dry model, additional variables representing the specific humidity  $h_k(x, y, t)$  in each layer; these variables are discretized on the model's  $T$ -grid. The specific humidity is assumed to be independent of  $z$  except when used in the formulas parameterizing moisture fluxes at the top and bottom of the AML (see below). The humidity equations in both the AML and the atmospheric interior are largely analogous to the AML temperature Eq. (18) (cf. Deremble et al., 2013) and are given by

$$\begin{aligned}
h_{mt} + ({}^a u_m h_m)_x + ({}^a v_m h_m)_y + \frac{{}^a W_{ek} h_m}{{}^a H_m} &= {}^a K_2 \nabla_H^2 h_m - {}^a K_4 \nabla_H^4 h_m + \frac{1}{\rho_m {}^a H_m} (E - P_m - F_m^{e-}); \\
h_{kt} + ({}^a u_k^g h_k)_x + ({}^a v_k^g h_k)_y &= {}^a K_2 \nabla_H^2 h_k - {}^a K_4 \nabla_H^4 h_k + \frac{1}{\rho_k {}^a H_k} (F_{k-1}^{e+} - P_k - F_k^{e-});
\end{aligned} \tag{31}$$

Here  $({}^a u_k^g, {}^a v_k^g)$  are the geostrophic velocities in the atmospheric layer  $k$ ,  $E$  is the evaporation and  $P_k$  is the precipitation;  $F_k^{e-}$  and  $F_k^{e+}$  are the moisture entrainment fluxes below and above the interface  $k$ , respectively (all of these fluxes are in  $\text{kg m}^{-2} \text{ s}^{-1}$ ). Once again,  $k = (m, 1, 2, 3)$  and  $k - 1 \rightarrow m$  for  $k = 1$ . The biharmonic viscosity term on the right-hand side is, again, included mainly for numerical stability. The equations (31) also use boundary conditions analogous to those for temperature (Section 2.3.2).

The evaporation over the ocean is given by (Gill, 1982):

$$\begin{aligned}
\frac{E}{\rho_m} &= C_E |{}^a \mathbf{u}_m - {}^o \mathbf{u}_m| (h_s({}^o \overline{T}_m + {}^o T_m) - h_{m,r}); \\
h_{m,r} &= h_m \frac{h_s(T_m({}^a H_m/2))}{h_s(T_m(0))},
\end{aligned} \tag{32}$$

where the atmospheric specific humidity near the ocean surface  $h_{m,r}$  is computed assuming constant relative humidity in the AML, following Deremble et al., 2012; the coefficient  $C_E = 1.5 \times 10^{-3}$ . Over land, we specify the (fixed in time) evapotranspiration flux (which also includes the zonally averaged evaporation from other ocean basins absent in our one basin configuration; this allows us to achieve reasonable values characterizing the moist model's climatological distribution of specific humidity). In space, this  $y$ -dependent flux decreases linearly from the  $\frac{E}{\rho_w}$  maximum value of  $1 \text{ m year}^{-1}$  at the southern boundary of the atmospheric model (note the usage of water density  $\rho_w = 1000 \text{ kg m}^{-3}$  here, leading to precipitation

estimates in terms of the equivalent water depth per unit time) to the minimum value of 0.1 m year<sup>-1</sup> at the northern boundary.

Entrainment fluxes of moisture in Eq. (31) are formulated in a way analogous to the entrainment heat fluxes. In particular, at the top of the AML,

$$\begin{aligned}
 F_m^{e+} &= {}^a w_{ek} (\rho_m h_m - \rho_1 h_{1,r}), \quad F_m^{e-} = 0, \quad \text{if } {}^a w_{ek} > 0 \\
 F_m^{e+} &= 0, \quad F_m^{e-} = - {}^a w_{ek} (\rho_m h_m - \rho_1 h_1), \quad \text{otherwise;} \\
 h_{1,r} &= h_1 \frac{h_s (T_1 ({}^a H_m))}{h_s (T_1 ({}^a H_m + {}^a H_1/2))};
 \end{aligned} \tag{33}$$

compare with Eq. (21). Here, the layer-1 reference specific humidity just above the AML  $h_{1,r}$  is computed by assuming constant relative humidity in layer 1 (cf. Deremble et al., 2012 and Eq. (32)). Entrainment moisture fluxes in the geostrophic interior ( $k = 1, 2$ ) are given by

$$\begin{aligned}
 F_k^{e+} &= {}^a e_k (\rho_k h_k - \rho_{k+1} h_{k+1}), \quad F_k^{e-} = 0, \quad \text{if } {}^a w_{ek} > 0 \\
 F_k^{e+} &= 0, \quad F_k^{e-} = - {}^a e_k (\rho_k h_k - \rho_{k+1} h_{k+1}), \quad \text{otherwise,}
 \end{aligned} \tag{34}$$

with  $F_3^{e-} = 0$ ; the entrainment rates  ${}^a e_k$  are computed using *the original formulas* Eq. (23) and (24) of the *dry* Q-GCM model (see further discussion below).

The precipitation rates are computed following Laîné et al., 2011 methodology, except for using the linear (instead of Laîné et al.'s quadratic) local atmospheric temperature profiles Eq. (28). In particular, the moisture Eq. (31) are first stepped forward with all the precipitation rates set to zero to update the values of the specific humidity; recall that the specific humidity is assumed to be independent of  $z$  in each layer. Then the vertical integrals of the newly computed specific humidity excess over the saturated specific humidity (which is a function of  $z$ ) within each layer are computed [for numerical efficiency, this is done semi-analytically by fitting a quadratic

function of  $z$  to  $h_k - h_s(z)$ ]. This amount of moisture is set to fall out, over the period  $2\Delta t$  associated with the leap-frog time step, as the precipitation  $P_k$ , and the specific humidity in the corresponding layer is reduced accordingly.

The hydrological cycle above is coupled with the model dynamics via the associated latent heat exchange/release. In the MQ-GCM, Eq. (17) is only meant to describe the sensible heat exchange between the ocean and the atmosphere, with a reduced value of the sensible-heat exchange coefficient  $C_h = 7 \times 10^{-4}$ . In addition, the oceanic mixed layer is experiencing the (perturbation) latent heat loss (in  $Wm^{-2}$ ) of

$${}^oQ_L = L(E - \langle E \rangle) \quad (35)$$

and the atmospheric layers — the (perturbation) latent heat gain of

$${}^aQ_{L,k} = L(P_k - \langle P_k \rangle), \quad (36)$$

where  $L = 2.5 \times 10^6 \text{ J kg}^{-1}$  is the latent heat of vaporization of water and  $k = (m, 1, 2, 3)$ . Note that the full latent-heat fluxes  $LE, LP_k$  both include the part associated with the basic state of the model in its radiative–convective balance, but the Q-GCM is formulated as a perturbation model, which requires the subtraction of the basic-state latent-heat fluxes. We here assume that the basic-state part of  ${}^oQ_L$  and  ${}^aQ_{L,k}$  is approximately given by the spatial averages of these quantities over the oceanic basin and atmospheric channel, respectively (this assumption is justified post hoc by the moist model’s AML and OML climatological temperatures being close to those of a dry model) —  $\langle E \rangle$  and  $\langle P_k \rangle$ ; hence, we remove these



spatial averages at each time step in Eq. (35) and (36) to define the latent-heat flux anomalies that force our perturbation heat equations.

The fluxes  ${}^oQ_L$  and  ${}^aQ_{L,m}$  directly enter the right-hand side of the OML and AML (Eq. (18)), respectively. The interior latent-heat release  ${}^aQ_{L,k}$  is added to the right-hand side of the corresponding layer's heat equation in Eq. (22), so that the sum  $\sum_k^3 {}^aQ_{L,k}$  enters, as an additional term, the right-hand side of Eq. (23) and modifies the entrainment rates  ${}^ae_k$ . Note again, however, that the moisture Eq. (31) use the first-guess, unmodified ("dry") entrainment rates computed from the original Eq. (23) and (24), upon which the precipitation rates  $P_k$  and latent heat corrections  ${}^aQ_{L,k}$  are computed and used to adjust the entrainment rates as follows:

$$\begin{aligned} {}^ae_1 &\rightarrow {}^ae_1 + \Delta {}^ae_1; & e_2 &\rightarrow e_2 + f_2 \Delta {}^ae_1; \\ \Delta {}^ae_1 &= \frac{\sum_{k=1}^3 {}^aQ_{L,k}}{\rho {}^aC_p (\Delta_1^a T + f_2 \Delta_2^a T)} \end{aligned} \quad (37)$$

These modified entrainment rates are then used to timestep the atmospheric QGPV equations.

The above numerical scheme — with the first guess 'dry' entrainment driving the moisture equations to produce latent-heat driven corrections to the entrainment, which are then used to force the QG model interior, — can be further improved by iterating the solution of the moisture equations at a given time step to achieve mutually consistent estimates of both precipitation and entrainment in the interior QG layers. In this scheme, the interior entrainment fluxes at a given iteration would be used, along with the fixed advective and diffusive fluxes, to update the interior humidity and compute the precipitation rates until these rates (and entrainment rates) converge to a steady solution. This procedure is, however, much

more numerically challenging than its first guess ‘dry entrainment’ implementation. The latter ‘dry entrainment’ implementation may formally be justified if the “moist” corrections to the dry entrainment produce relatively small changes to the interior precipitation. To explore this issue further, we included, in the present version of the MQ-GCM model, an option that allows one to modify the ‘dry’ entrainment-based precipitation estimates via one additional iteration in which the interior moisture Eq. (31) are stepped with the entrainment moisture fluxes (Eq. (34)) utilizing the moisture corrected entrainment rates (Eq. (37)).

Moisture transport and latent heat release driving the atmospheric response in the areas away from the oceanic warm regions of evaporation are important elements of air–sea interaction over variable SST fronts, which are altogether missing in a dry version of the Q-GCM model (cf. Deremble et al., 2012).

## 4.2. MQ-GCM Simulations

This section documents key characteristics of the new model versions described in Chapter 2 and Section 4.1, focusing on the latter, moist version of the model. We set the amplitude of the variable incoming radiation to  $150 \text{ W m}^{-2}$  (as compared to  $80 \text{ W m}^{-2}$  in Hogg et al., 2014) and ran three 130-year simulations of the new dry version of the model, as well as three analogous simulations of the new moist model, MQ-GCM (six simulations total), using model setups with and without explicit temperature dependence in the atmospheric-mixed-layer wind. For both dry and moist versions of the model, the control run, without this dependence, was started

from the final state of the preliminary 100-year spin-up simulation (from rest); the partially coupled simulation was initialized by the final state of the control run; and the fully coupled temperature-dependent simulation continued from the final state of the partially coupled run. We disregarded the first 30 years to allow for model spin-up and adjustment (chosen based on the ocean energy diagnostic) and analyzed the last 100 years of each simulation. Below we describe the results from the moist-model runs only; in the present parameter regime, the qualitative and quantitative behavior of the companion dry model turned out to be very similar, and hence the dry-model results are not shown here (see Chapters 3 and 5 for further discussion).

The atmospheric mean state does not appear to depend substantially on whether the temperature feedback on AML wind is included in the model or not. In each case, the atmosphere is characterized by a straight climatological jet with a reasonable vertical shear (Fig. 18) and some zonal modulation; in particular, surface winds tend to be a bit stronger over ocean (due to reduced surface drag), but barotropic wind exhibits an opposite modulation (weaker wind over ocean), consistent with reduced temperature gradient over ocean (Fig. 19). On top of this mean state, the atmosphere is characterized by a vigorous synoptic turbulence (Fig. 20).

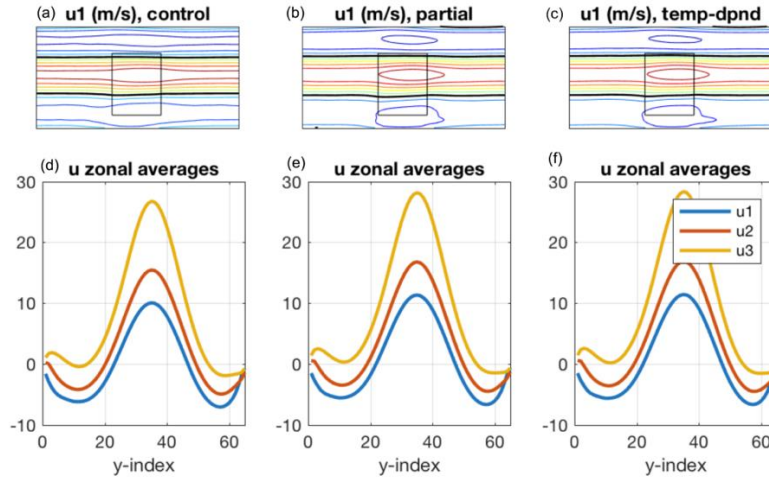


Figure 18 - Atmospheric mean state in control (a, d), partially coupled (b, e), and fully coupled (c, f) simulations involving temperature dependent wind in the atmospheric mixed layer. (a–c) Lower-layer zonal wind,  $Cl = 2 \text{ m s}^{-1}$ , the zero contour is black; rectangle in the middle (here and in other figures) marks the location of the ocean. (d–f) Zonally averaged zonal wind ( $\text{m s}^{-1}$ ) in all layers (see legend).

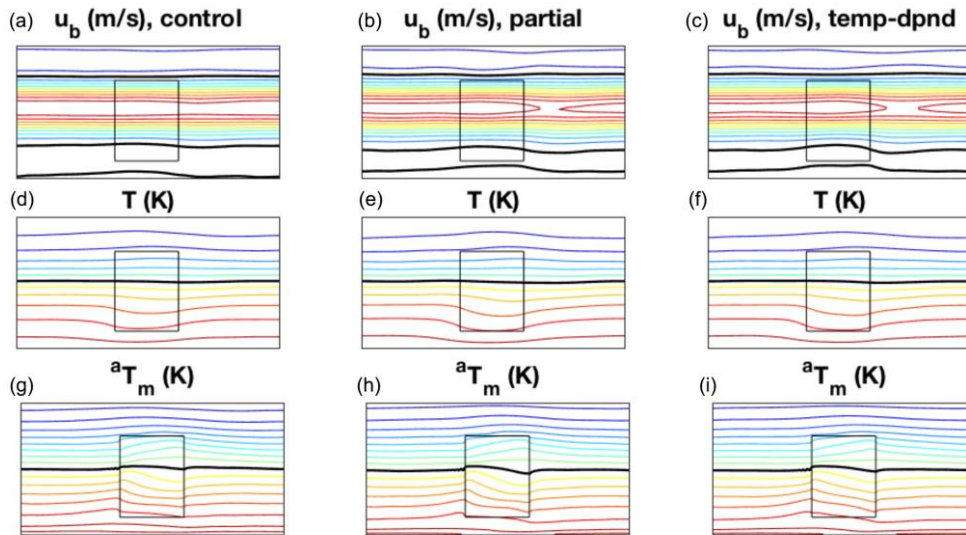


Figure 19 - Atmospheric mean state (continued). (a–c) Barotropic zonal wind,  $Cl = 2 \text{ m s}^{-1}$ ; (d–f) interior temperature perturbation according to Eq. (12),  $Cl = 2 \text{ K}$ ; (g–i) AML temperature,  $Cl = 2 \text{ K}$ .

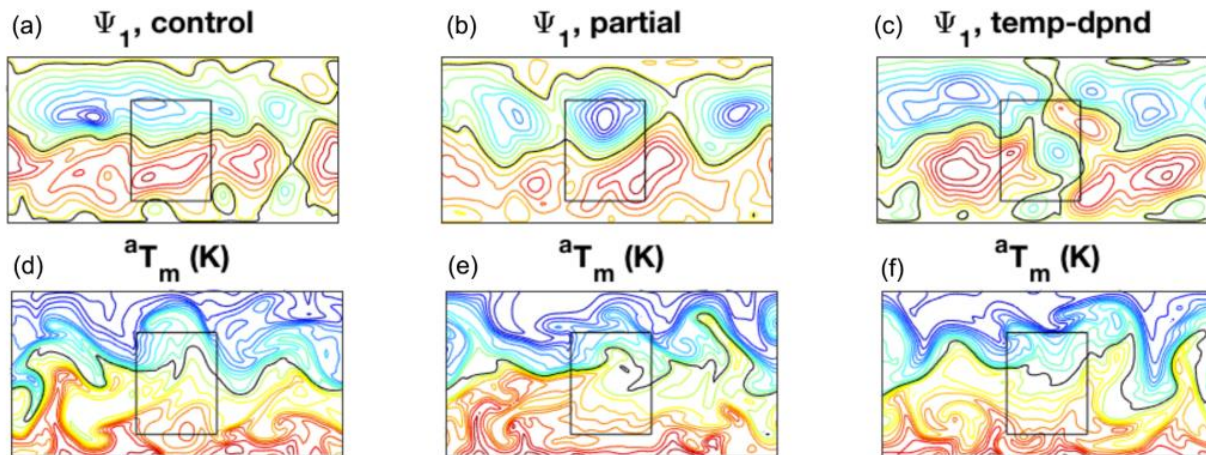


Figure 20 - Atmospheric snapshots from the three simulations. (a–c) Lower-layer streamfunction; (d–f) AML temperature perturbation,  $CI = 2\text{ K}$ . Black curves show the zero contour.

The time-mean ocean currents (Fig. 21) represent large-scale subtropical and subpolar gyres and strong inertial recirculation, which help maintain an intense eastward jet in the control and partially coupled simulations. The inertial recirculations largely collapse in the fully coupled simulation (see, for example, the discussion in Chapter 3 and Hogg et al., 2009), with barotropic transports there ( $\sim 40\text{ Sv}$ ) only about one-third of those in the control and the partially coupled runs.

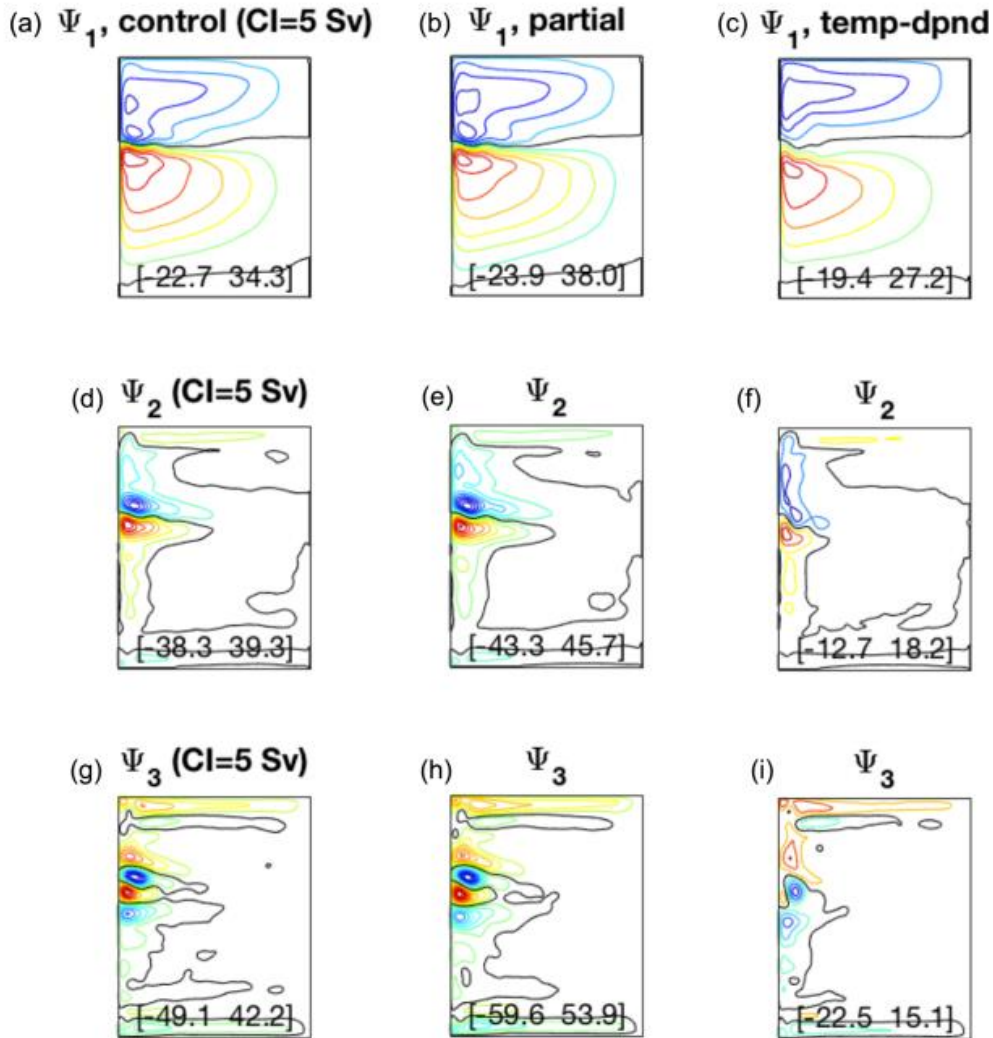


Figure 21 - Oceanic time-mean streamfunction (Sv) in control (a, d, g), partially coupled (b, e, h), and fully coupled (c, f, i) simulations involving temperature-dependent wind in the atmospheric mixed layer. Top, middle, and bottom layer results are shown in the corresponding rows of the figure. CI is shown in panel captions. Black curves show the zero contour. The panels also display the range of streamfunction in Sv.

Accordingly, the eastward jet becomes much weaker and so is the climatological SST front (Fig. 22); this has probably much to do with anomalous Ekman pumping structures over the inertial gyres seen in the fully coupled simulation (Fig. 22, bottom right). The ocean resolution (of 10 km) requires a relatively high viscosity (and low Reynolds number), and the ocean state is probably better characterized as eddy permitting rather than eddy resolving here (Fig. 23).

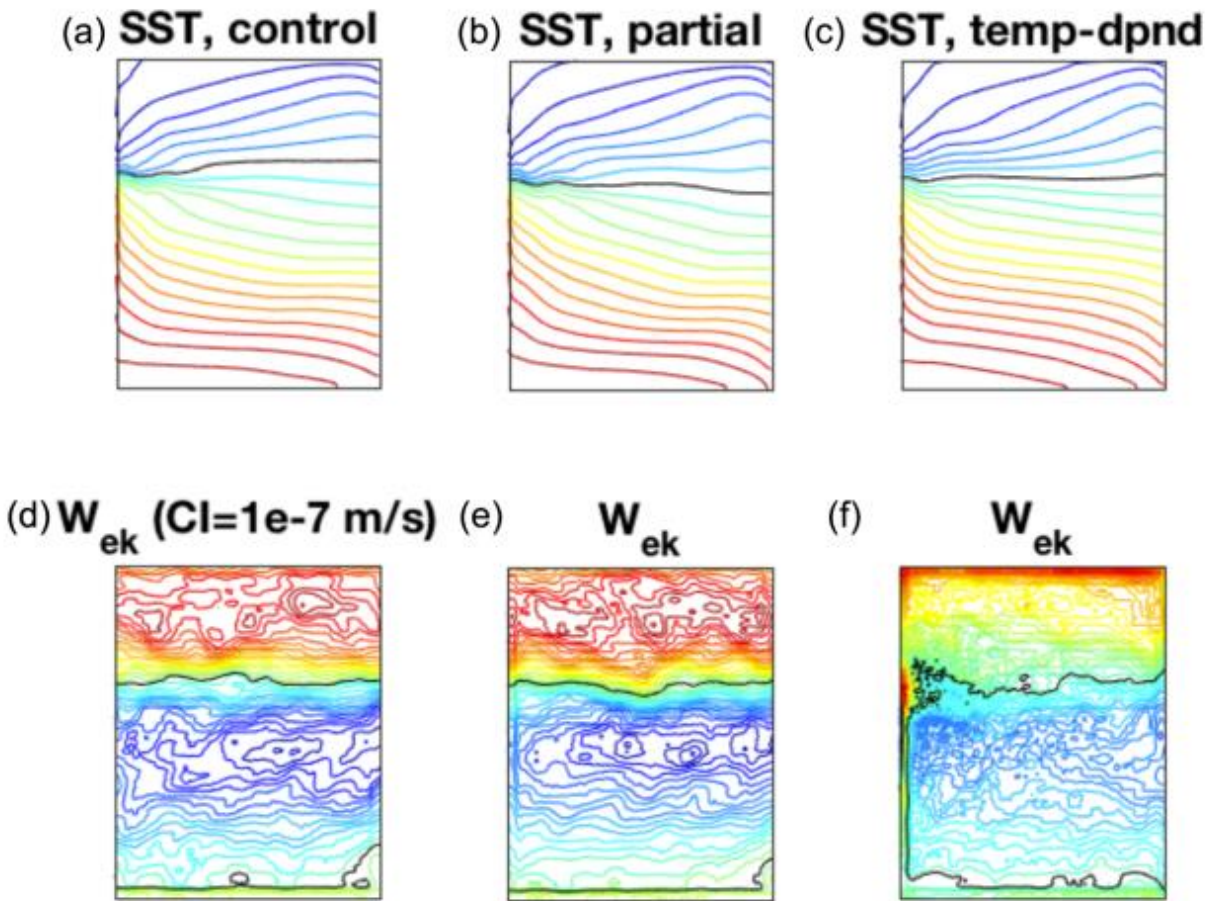


Figure 22 - Time-mean SST (a–c,  $CI = 1\text{ K}$ ) and ocean Ekman pumping (d–f,  $CI = 10^{-7}\text{ m s}^{-1}$ ) in control (a, d), partially coupled (b, e), and fully coupled (c, f) simulations involving temperature dependent wind in the atmospheric mixed layer. Black line on SST plots shows  $-2^\circ\text{C}$  anomaly with respect to the mean-state SST, approximately indicating the location of SST front; black line shows the zero contour on Ekman pumping plots.



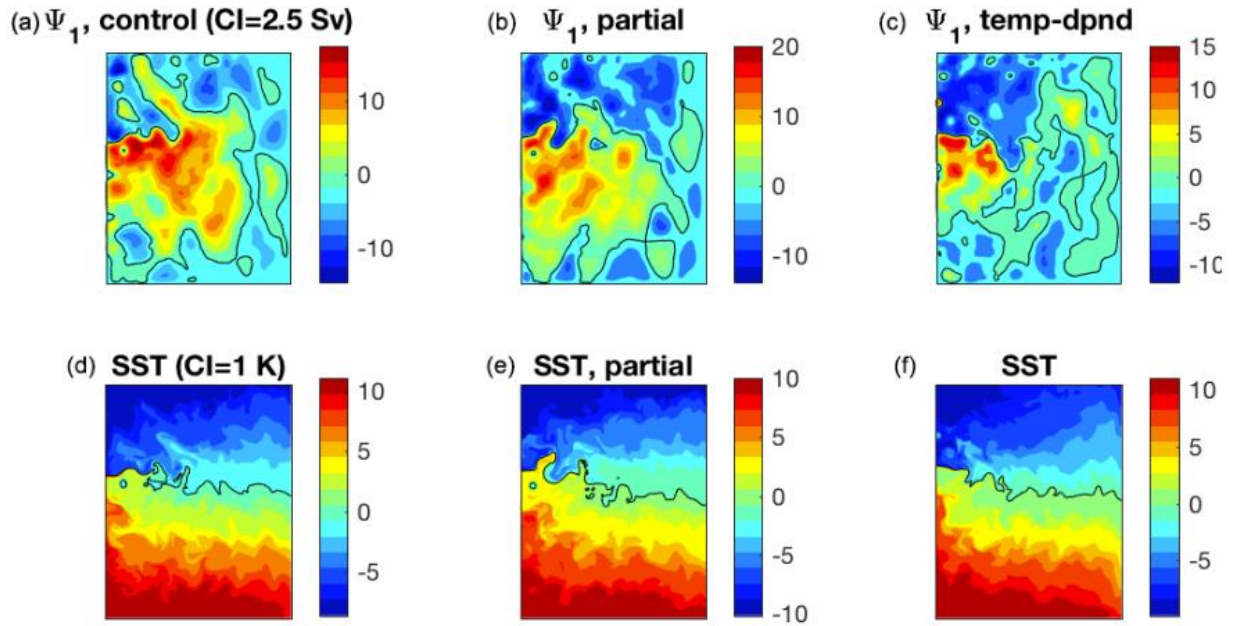


Figure 23 - Oceanic snapshots from the three simulations. (a–c) Upper layer streamfunction (Sv); (d–f) OML temperature perturbation (K).

We now show the moist characteristics of the model in the control simulation with dry entrainment formulation (23)– (24) of moisture entrainment fluxes in Eq. (34). Fig. 24 displays a segment of the basin-mean specific humidity time series for all three atmospheric layers, featuring a reasonable vertical distribution of this quantity. The basin-mean moisture budget time series are shown in Fig. 25. The net evaporation and precipitation in the model are both around  $0.6 \text{ m yr}^{-1}$ , which is lower than the observed global-mean values of about  $1 \text{ m yr}^{-1}$  due to the lack of tropical dynamics in the QG formulation. The basin-mean E–P is slightly unbalanced, indicating a small moisture flux of about  $0.1 \text{ m yr}^{-1}$  through the open boundaries of the model (see Sections 2.2.4 and 4.1).



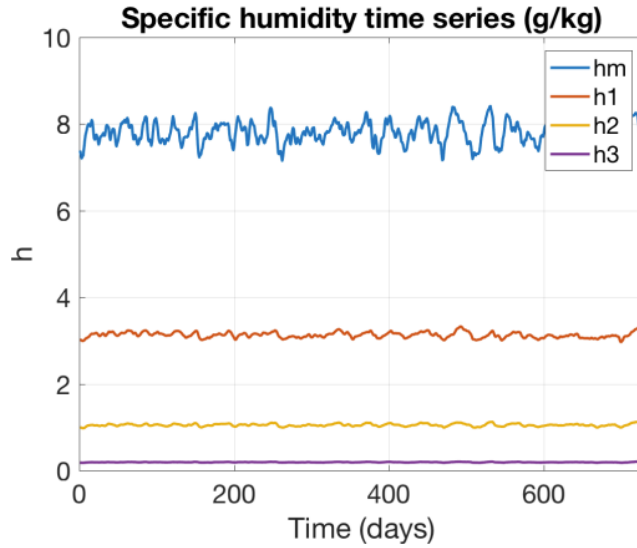


Figure 24 - Time series of the basin-mean specific humidity ( $\text{g kg}^{-1}$ ) in the four atmospheric layers (see the legend).

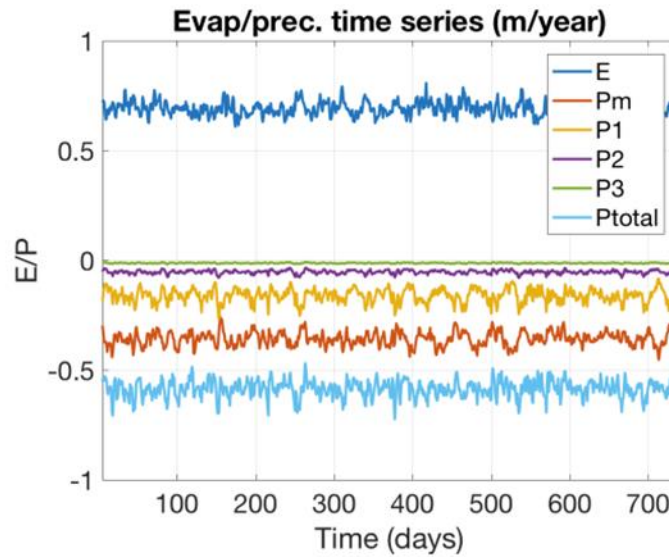


Figure 25 - Time series of the basin-mean evaporation (positive) and layer precipitation (negative) ( $\text{m yr}^{-1}$ ); see the legend.

The specific humidity climatological distributions (Fig. 26) are slightly zonally nonuniform due to land–sea contrast and have patterns generally consistent with the atmospheric temperature distributions in Fig. 19. The evaporation (Fig. 27, left) is prescribed and zonally uniform over land (see Section 4.1) but is active over ocean, exhibiting reduced values to the north and

enhancement along the southern and western boundary of the ocean and the double-gyre confluence zone.

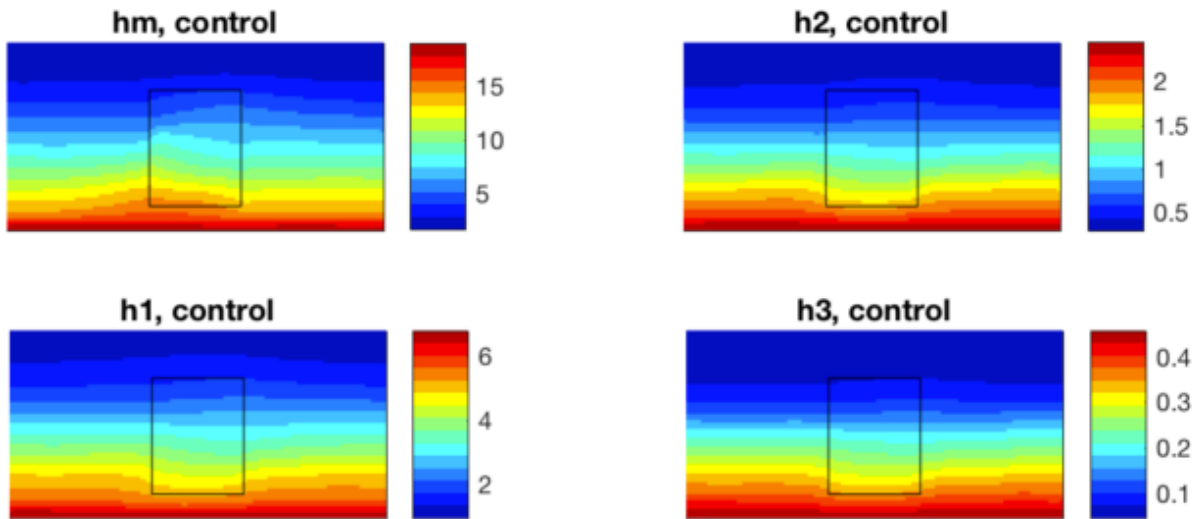


Figure 26 - Climatological distribution of specific humidity ( $g\ kg^{-1}$ ).

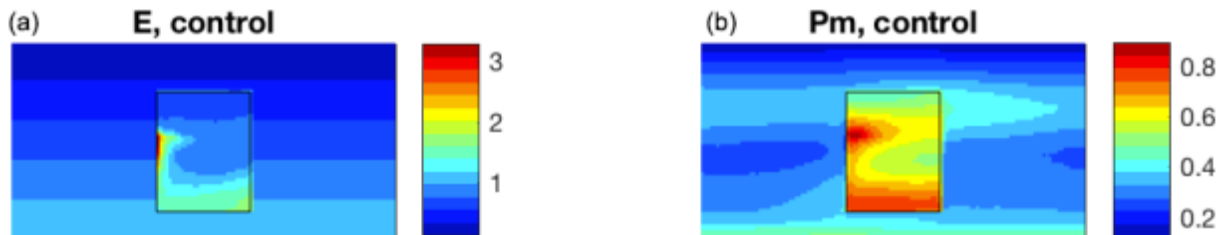


Figure 27 - Climatological distribution of evaporation (left) and precipitation in the mixed layer (right) ( $m\ yr^{-1}$ )

Atmospheric boundary layer precipitation is also enhanced over these areas (Fig. 27, right) and exhibits relative minima over the rest of the ocean. Globally, precipitation reaches local maximum at the southern boundary of the model and global minimum at the northern boundary and has a dipolar zonal structure around the axis of the channel, with precipitation minimum/maximum at the anticyclonic (equatorward)/cyclonic (poleward) flanks of the

midlatitude jet, respectively. These features also translate, to some extent, to the precipitation distribution in the atmospheric interior (Fig. 28), although land–sea contrast in precipitation in the interior is opposite in sign to the one within the atmospheric boundary layer.

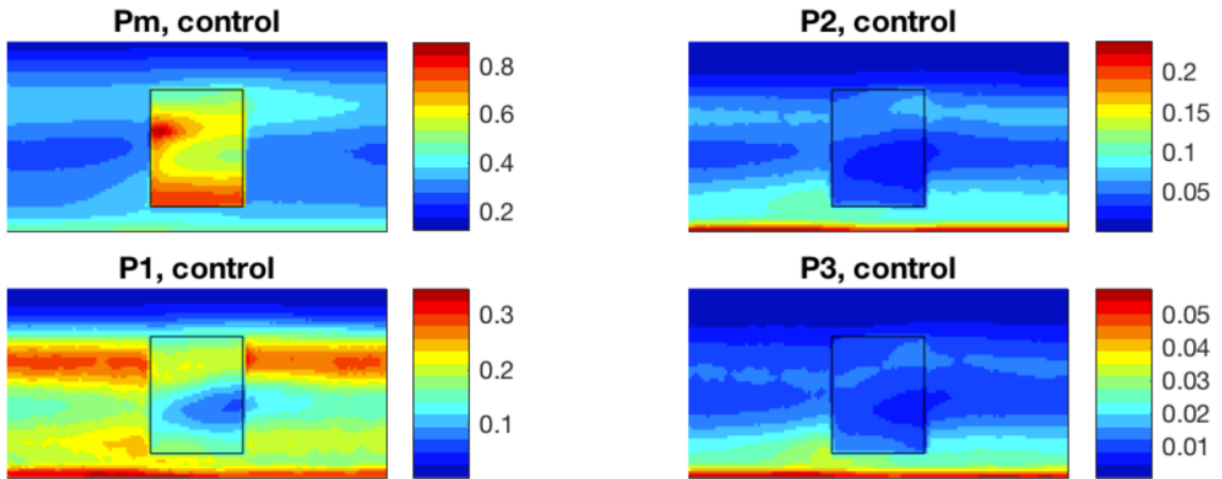


Figure 28 - Climatological distribution of precipitation ( $m\ yr^{-1}$ ); all layers.

The climatological distribution of precipitation is the result of averaging over intermittent, in space and time, precipitation episodes, as illustrated by a snapshot example in Fig. 29.

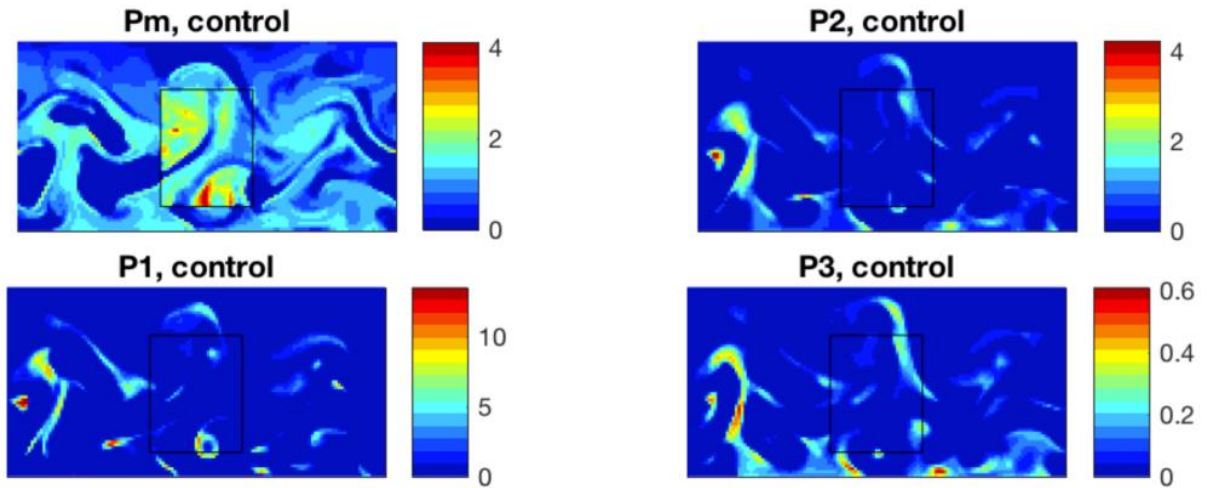


Figure 29 - Snapshot of precipitation ( $\text{mm d}^{-1}$ ); all layers.

Finally, we present here initial evidence for a possible important effect of the temperature-dependent wind-stress formulation on the low-frequency dynamics of MQ-GCM. This effect can be noticed in the behavior of the leading EOF of SST (Fig. 30), dominated, in all simulations, by a monopolar (in  $y$ ) SST pattern in the region of the ocean's eastward jet and its extension.

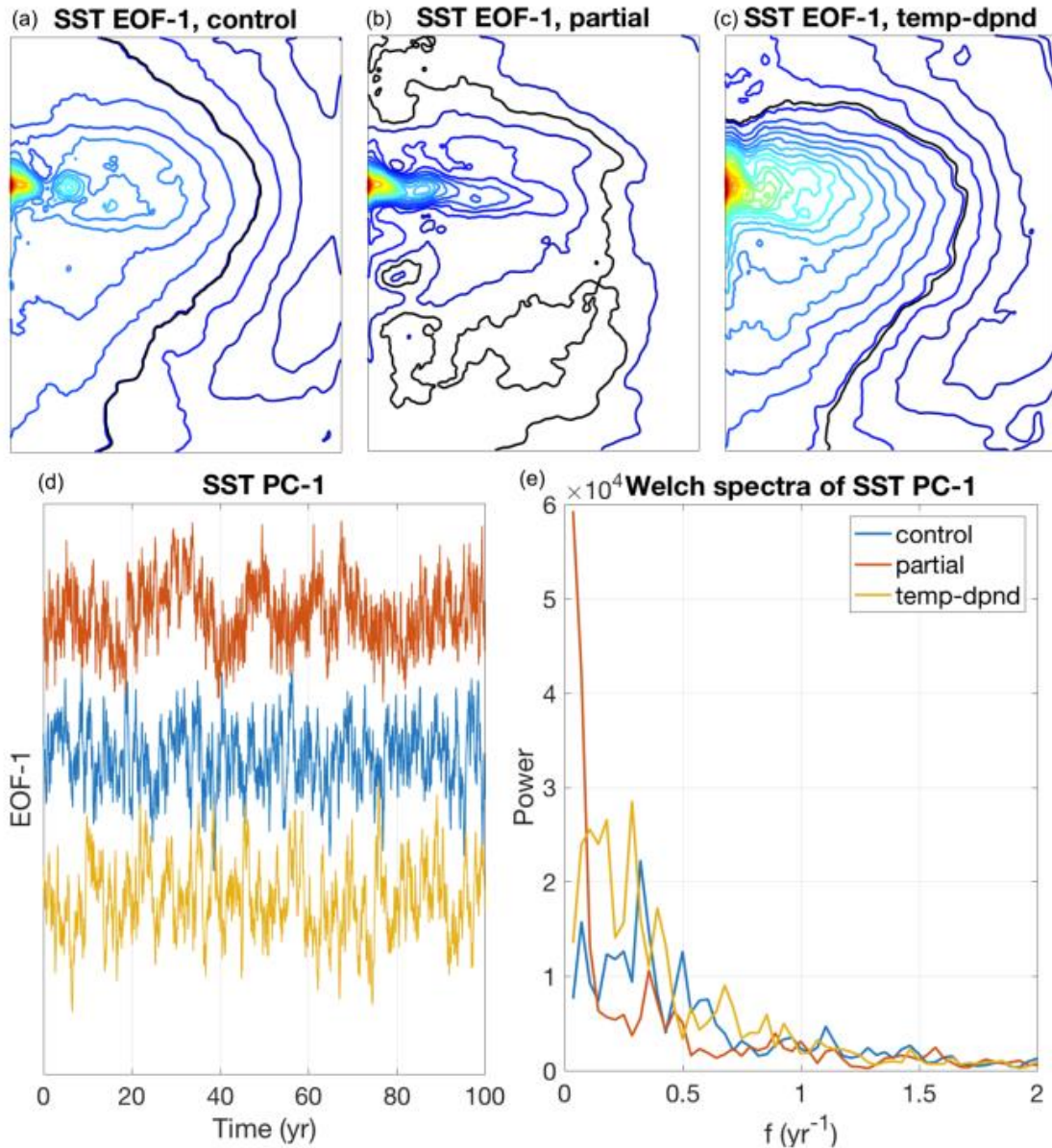


Figure 30 - The leading EOF of SST. (a-c) EOF pattern in control (a), partially coupled (b), and full temperature-dependent momentum coupling (c) simulations; the zero contour is black. (d, e) PC-1 (d) and Welch-periodogram spectra (e) (the type of the simulation corresponding to each curve shown is given in the legend).

The intensity, meridional localization, and west-to-east scale of this pattern are the largest in the partially coupled run, which has the strongest oceanic turbulence capable of affecting mesoscale winds above the oceanic eastward jet (Fig. 30, top middle panel). This variability tends to be suppressed in both the control run (with no direct SST effect on the AML winds: Fig. 30, top left panel) and the fully coupled run with active mesoscale coupling (but in which the

ocean eddies are partly suppressed: Fig. 30, top right panel), indicating the importance of both the ocean eddies and air–sea mesoscale coupling for this mode. Furthermore, this mode’s time dependence is characterized by a pronounced interdecadal variability in the partially coupled simulation, whereas the dominant timescales in the control and fully coupled simulations are shorter (interannual-to-decadal) and the associated variances are smaller (Fig. 30, bottom row), with the energy-density ratio of the partially coupled to control run of about 6 at low frequencies. It is not immediately clear, however, whether this mode imprints itself onto the atmosphere even in the partially coupled simulation. There are indications that this run’s leading jet-shifting EOF of the atmospheric streamfunction (analogous to that of the control run shown in the top panel of Fig. 31) has an enhanced energy at the low-frequency end of the spectrum compared to the control and fully coupled simulations (Fig. 31, bottom), but this enhancement is not statistically significant and may be due to sampling. Longer and – most importantly – higher-resolution simulations, in both the ocean and the atmosphere (cf. Martin et al., 2020), are likely to be required to gauge the potential of the active mesoscale air–sea coupling to fuel decadal climate modes.

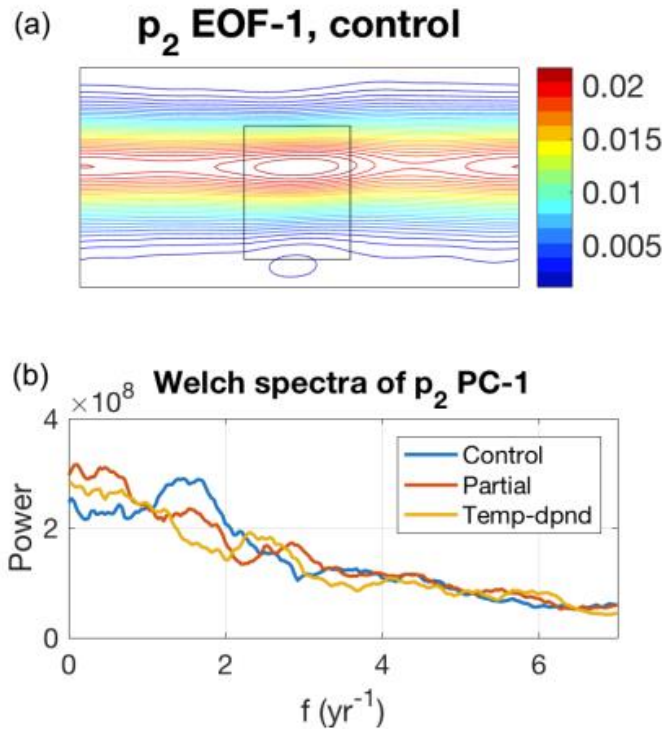


Figure 31 - The leading EOF of the mid-layer atmospheric streamfunction. (a) EOF pattern in the control simulation. (b) Smoothed Welch-periodogram spectra of PC-1 in each simulation (the type of the simulation corresponding to each curve shown is given in the legend).

In summary, the inclusion of moist dynamics in the Q-GCM model didn't translate into a substantial enhancement of free-atmosphere variance at decadal+ time scales in the model version with an eddy-permitting 10-km-resolution ocean and coarse-resolution (120-km) atmosphere (which is something that — we hypothesize — has to happen in an elusive model configuration conducive to multi-scale coupled modes of the type sought here). In fact, the behavior of the dry model is essentially the same as that of the moist model in all of the simulations (control, partially coupled and temperature-dependent wind-stress simulations) (not shown), and also, despite qualitative improvements, not that different from that of the original Q-GCM model (Chapter 3).

With this unfavorable result in mind, we describe in Chapter 5 our attempts to find a parameter regime leading to a more active multi-scale ocean–atmosphere coupling; these attempts also involved experimenting with oceanic and atmospheric model resolutions. To our frustration, these efforts haven’t proved either (Section 5.1). The puzzling lack of the effect of moist processes onto the dynamics of the MQ-GCM’s free atmosphere in the coupled simulations can in principle be due to (i) still insufficient persistence of ocean induced front-like SST anomalies able to exert substantial mesoscale forcing onto the atmosphere; and (ii) lack of the atmospheric sensitivity to such anomalies (even if the latter are relatively persistent and sufficiently strong). The final step of our analysis (Section 5.2) thus concentrated on the atmosphere-only experiments with time-dependent SST fronts meant to better differentiate between the hypotheses (i) and (ii) above.



## Chapter 5

### 5. Large-scale effects of mesoscale air–sea coupling in MQ-GCM

After detecting no enhanced atmospheric sensitivity to oceanic low-frequency variability in the Q-GCM simulations using model formulation with added moist dynamics (Chapter 4), we devoted quite a bit of time trying to answer the following three main questions:

1. How would the coupled model behavior change in a more turbulent oceanic parameter regime able to produce persistent oceanic eastward jet extension latitudinal shifts?
2. Does the behavior of the coupled model depend on the atmospheric model's horizontal resolution?
3. Is the moist version of the model more sensitive to variable mesoscale SST anomalies compared to the dry model?

#### 5.1 Multi-century simulations under alternative ocean parameter settings

The turbulence in quasi-geostrophic ocean models is known to be strongly controlled by several key parameters. The first one is, of course, *the horizontal viscosity*, whose lower values are associated with high Reynolds numbers and produce regimes with enhanced mesoscale turbulence (e.g., Berloff and McWilliams, 1999a; Primeau, 2002; Berloff et al., 2007; Hogg et al., 2003, 2005, 2009; Shevchenko et al., 2016, among many others). Decreasing viscosity in an

ocean model is numerically demanding as it generally requires finer horizontal resolution and smaller time steps for numerical stability.

Another important parameter affecting the nature of the oceanic circulation, at least in the closed-basin ocean models in the double-gyre configuration is *the ocean mixed boundary condition coefficient* ( $\alpha_{bc}$ ) (Hogg et al. 2014), setting which to zero corresponds to the free-slip boundary conditions, whereas infinite value — to the no-slip boundary conditions (Haidvogel et al., 1992; Berlof and McWilliams, 1999a, b; Hogg et al., 2005; Deremble et al., 2011; Hogg et al., 2014). Haidvogel et al., 1992 found a wide range of dynamical regimes controlled by the value of this coefficient. For example, they showed that a sufficiently large  $\alpha_{bc}$  results in the premature separation of the subtropical and subpolar western-boundary currents before their confluence, leading to the double eastward jet and two separated (subpolar and subtropical) gyres; this also produces a decrease in the basin-integrated mean and eddy kinetic energy. Note that how large the value of  $\alpha_{bc}$  is from the physical perspective depends on the scale of the flow, which is itself controlled by the frictional parameters in the vicinity of the boundaries, as well as by stratification parameters (Rossby radii, see below) through their effect on flow stability.

The latter parameters are thus the third subset among those controlling the flow regime in the quasi-geostrophic double-gyre ocean models. Note that in addition to their importance for the process of generating spontaneous oceanic variability, they are also obviously important in the Rossby wave propagation, which may by itself be central to the physics of ocean–atmosphere coupled modes (Jin 1997, Ferreira et al., 2001; Kravtsov and Robertson, 2002; Arzel and Huck,

2003). In the context of the three-layer QG model, the two internal Rossby radii are derived from known layer thicknesses and densities.

We began our parameter sensitivity analysis by borrowing the set of ocean parameters (resolution, viscosity, mixed boundary condition coefficient, reduced gravities) from Martin et al., 2020 in order to produce a more energetic ocean which would presumably lead to a stronger free atmosphere forced (or coupled) response. We, therefore, repeated the experiments from Section 4.2 using high horizontal resolution in both ocean and atmosphere, namely 40 km for the atmosphere and 5 km for the ocean, but, again, did not identify any substantial differences between the two sets of simulations (figure not shown).

Since no major differences were found to arise in the above experiments compared to analogous simulations in Section 4.2, another set of experiments was performed, this time with different values of the oceanic reduced-gravity parameters. In particular, the values from Martin et al., 2020 (0.015, 0.0075 m/s<sup>2</sup>) were replaced with the new reduced-gravity values of 0.04 m/s<sup>2</sup> for the first interface and 0.01 m/s<sup>2</sup> for the second interface, which gives deformation radii equal to 40 km for the first layer and 22 km for the second layer, mimicking the three-layer oceanic QG configuration of Kurashina and Berloff, 2023b. Again, we did not find any more pronounced response in the free atmosphere that is statistically different from that in the analogous coarser-resolution simulation with our default parameter set (Section 4.2), even with the increased horizontal resolution in the atmosphere (of 40 km).

Finally, we performed yet another set of control, partially and fully coupled (in terms of temperature-dependent wind stress) experiments by using different values of mixed BC coefficient  $\alpha_{bc}$ , with values ranging from 0.5 (closer to the no-slip conditions) to 0.2, 0.05 and

0.02 (progressively closer to the free-slip conditions), keeping the rest of parameters as suggested by Martin et al., 2020. In these experiments, we once again did not produce a free-atmospheric response more modulated at low frequencies (on interannual to decadal longer time scales) compared to the default MQ-GCM configuration.

These results suggest that the MQ-GCM's free atmosphere does not really "feel" oceanic anomalies irrespective of the ocean model jet's dynamical regime and the level of turbulence. To better diagnose and quantify this response in the moist and dry models, we resorted to atmosphere-only simulations similar to those in Chapter 3, but now with the SST fronts characterized by variable latitudinal position. These analyses are described in the next section.

## 5.2 Atmospheric response to variable SST fronts in dry and moist Q-GCM models

The goal of this set of experiments was to document and better quantify the lack of free-atmosphere sensitivity to mesoscale SST anomalies in control, mesoscale coupled (with temperature-dependent wind stress) and partially coupled simulations of dry and moist Q-GCM versions. Based on the analyses of coupled experiments (Sections 4.2, 5.1) we hypothesized that our model ocean is not able to generate the SST-front anomalies strong enough to produce a significant impact on the free atmosphere but that it would still be possible that the modified Q-GCM atmosphere, especially its version with moist dynamics, would exhibit a substantial large-scale response to larger (and more persistent, compared to those in the full coupled model) mesoscale SST anomalies. To check whether this is true, we resorted to atmosphere-

only configuration and analyzed the upper-level atmospheric jet responses to the SST fronts of different magnitudes and positions relative to the mid-ocean, including eventually the simulation with variable-position SST fronts, which allows us to compare the magnitudes of forced and internal atmospheric variability in dry and moist simulations.

#### 5.2.1 Atmospheric variability in the simulations forced by the SST fronts fixed in time

First, we repeated the experiments of Section 3.2 with static SST fronts, one located in the middle of the ocean and the other shifted by 1500 km to the south. As before, in both dry and moist Q-GCM, the position of the atmospheric jet's climatological position migrated closer to that of the SST front, irrespective of the atmospheric model resolution. We thus argue, again, that this adjustment is not really a manifestation of the SST front's mesoscale control of the atmospheric jet position (cf. Deremble et al., 2012) but rather the function of artificially maintained surface heat-flux anomaly associated with the pre-specified location of the SST front.

These results clearly indicate that the Q-GCM atmosphere would be sensitive to the low-frequency shifts of the SST-front position. To quantify such a response, we conducted experiments with variable-position SST fronts, first using linear in time southward displacement of the front, and then with the front whose position changes sinusoidally with a certain period. In each case, we used a very strong front, with the SST jump on the order of 20°C over the extent of about a 300-km-wide frontal zone (the magnitude of the front used in this section is shown in Fig. 36).

### 5.2.2 SST front slowly drifting southward

In order to investigate how the slow-moving SST front affects the free atmosphere we conducted the experiment in which the idealized SST front moved 1500 km to the south of its original position in the center of the ocean basin, linearly in time over the duration of 100 years (hereafter, slow-moving SST front) and compared the atmospheric variability in this simulation with that in the two experiments of Section 5.2.1. There, the front's position was fixed in the middle of the ocean in the control configuration and shifted by 1500 km to the south in the "shifted SST" configuration; the control and shifted configuration thus corresponded to the initial and final position of the front in the slow-moving SST front experiment. All these simulations were performed, once again, using both dry and moist versions of the Q-GCM model, with and without TDWS parametrization, and in coarse (120 km) and high (40 km) horizontal atmospheric resolution; this amounts to 8 simulations for each of the control, shifted SST and slow-moving SST cases, and the total of 24 simulations with 100-year duration each.

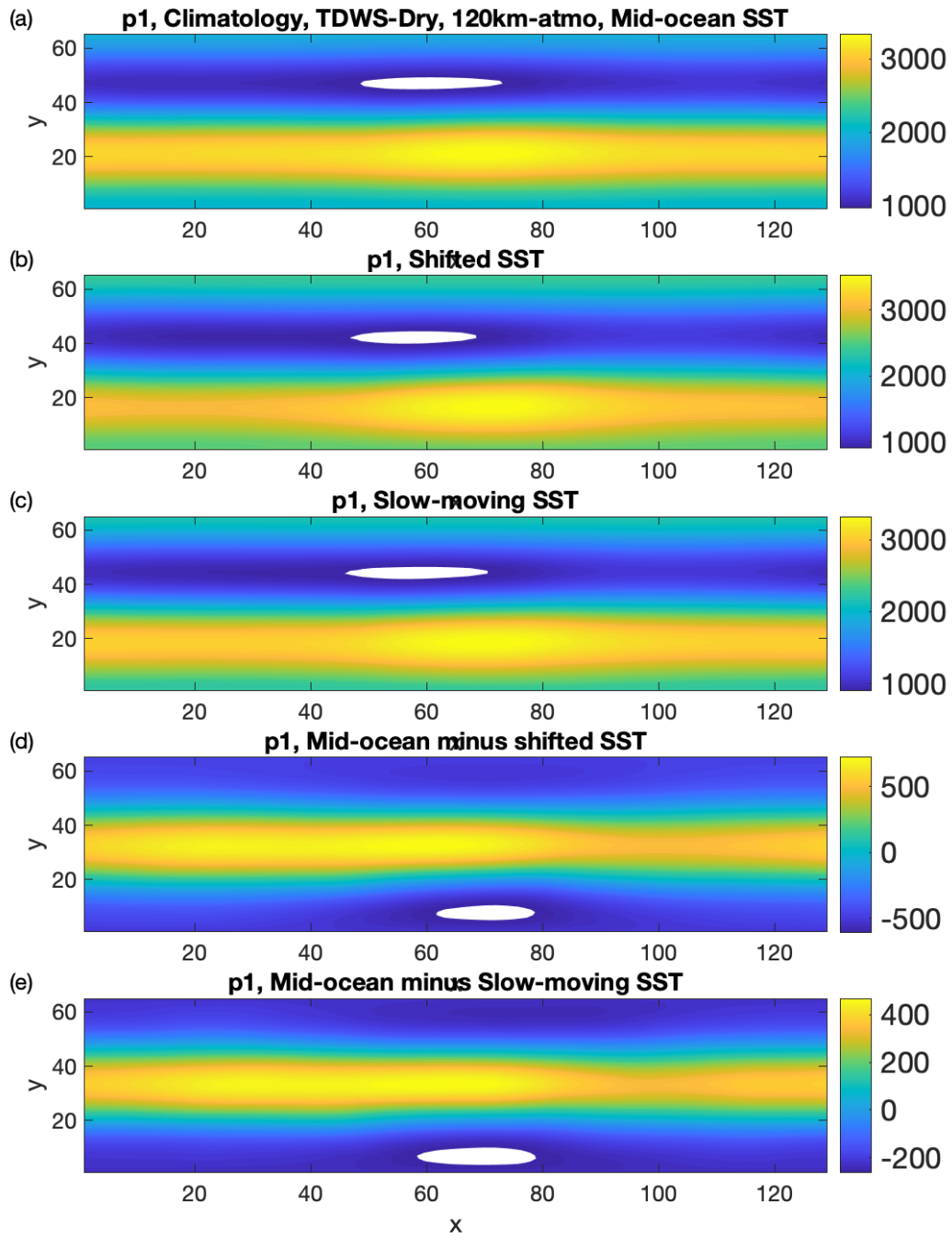


Figure 32 - Climatology of the lower-layer dynamic pressure ( $m^2/s^2$ ) from the coarse-resolution experiment of dry model with TDWS parametrization forced by: (a) default SST front; (b) shifted SST front; (c) slow-moving SST front. (d) The difference between (a) and (b); (e) the difference (a) and (c). The x and y axes show grid points at the 120 km spacing in both cases.

Not surprisingly, the climatological jet position is shifted to the south in both the shifted SST front and slowly moving SST front experiments relative to this position in the control configuration (Fig. 32). As expected, the shift is the strongest in the shifted SST case and is somewhat reduced in the slowly moving SST front case (where climatological SST front position is in between the initial and final front positions associated with the control and shifted SST cases). Similar climatological jet displacements are also present in the middle and upper atmospheric layers, as well as in the simulations with/without TDWS parameterization, and in both dry and moist versions of the model (not shown).

We now investigate the forced atmospheric response to the slowly shifting SST front (forced signal) by performing the EOF analysis of the lower-layer atmospheric streamfunction smoothed by 10-yr, 20-yr, and 30-yr boxcar running-mean filters. Using different filters allows us to assess and visualize the signal-to-noise ratios associated with the relative magnitude of the forced atmospheric jet shifts and internal jet-shifting variability that is typically the dominant low-frequency internal mode in the atmospheric models and, to some extent, observations.

Indeed, the leading EOF in all of the configurations shown in Fig. 33 — namely, the default SST front (upper plot), shifted SST front (middle plot), and slow-moving SST front (bottom plot) — is a near-zonally symmetric monopolar streamfunction anomaly with a maximum close to their respective SST fronts' climatological location, which describes meridional jet shifts with respect to the climatological axis of the jet. These shifts are entirely due to internal variability in the simulations with the fixed SST front location and are a combination of the internal and forced jet shifts in the simulation with the slow-moving SST front.



One can isolate the forced trend by smoothing the streamfunction time series prior to computing EOFs to reduce the magnitude of internal jet variations. In a dry model, 10-yr smoothing is clearly not enough to isolate the forced trend (Fig. 34a). This is seen from the fact that internal variations in the meridional position of the jet (in the fixed SST front simulations) are still large after averaging, and the long-term trends similar to the one in the simulation forced by the slow-moving SST front are visually quite likely to arise by chance in a finite-duration time series (for example, the simulation with mid-ocean SST front exhibits essentially the same long-term trends as the simulation with the slow-moving SST front). The internal variations are much smaller when averaged out by the 20-yr and even more so when averaged by the 30-yr running-mean filter (Figs. 34b, c, respectively) and the forced trend clearly dominates variability in the latter case.

Interestingly, the magnitude of internal jet-shifting variability is smaller in the TDWS simulations using MQ-GCM (Fig. 35), so that less averaging is necessary to isolate the jet-shifting signal there. This is indicative of a higher forced-signal to internal-noise ratio in the moist version of the model even if the sensitivity of the free atmosphere to shifts of the SST front is still weak in this model. In the next subsection, we will study whether this conclusion applies to the simulations forced by periodic variations of the SST front's meridional position.

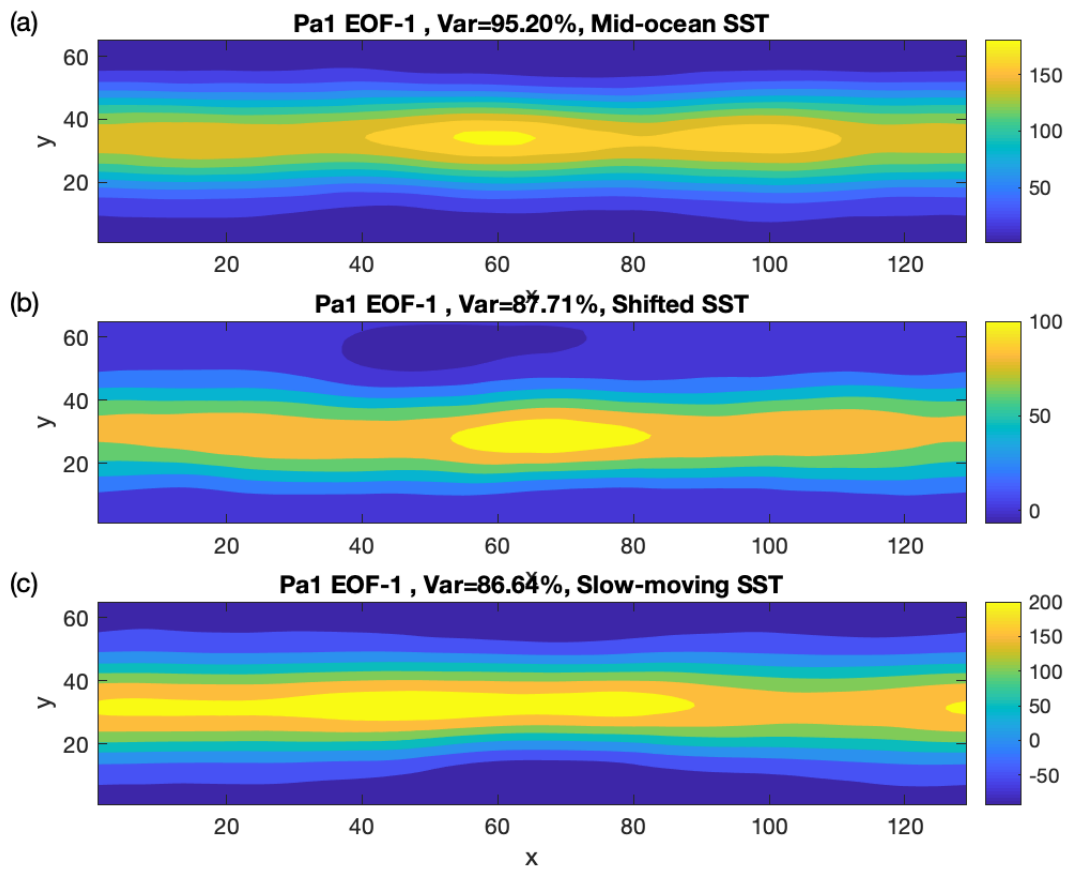


Figure 33 - The leading (dimensional) EOF of the lower layer dynamic pressure smoothed by the 10-yr running-mean boxcar filter, from the simulations of the dry version of Q-GCM model with TDWS parametrization, for (a) control simulation using the default SST front position in the middle of the ocean; (b) shifted SST front simulation; and (c) slow-moving SST front simulation. The x and y axes show grid points at the 120 km spacing in both cases.

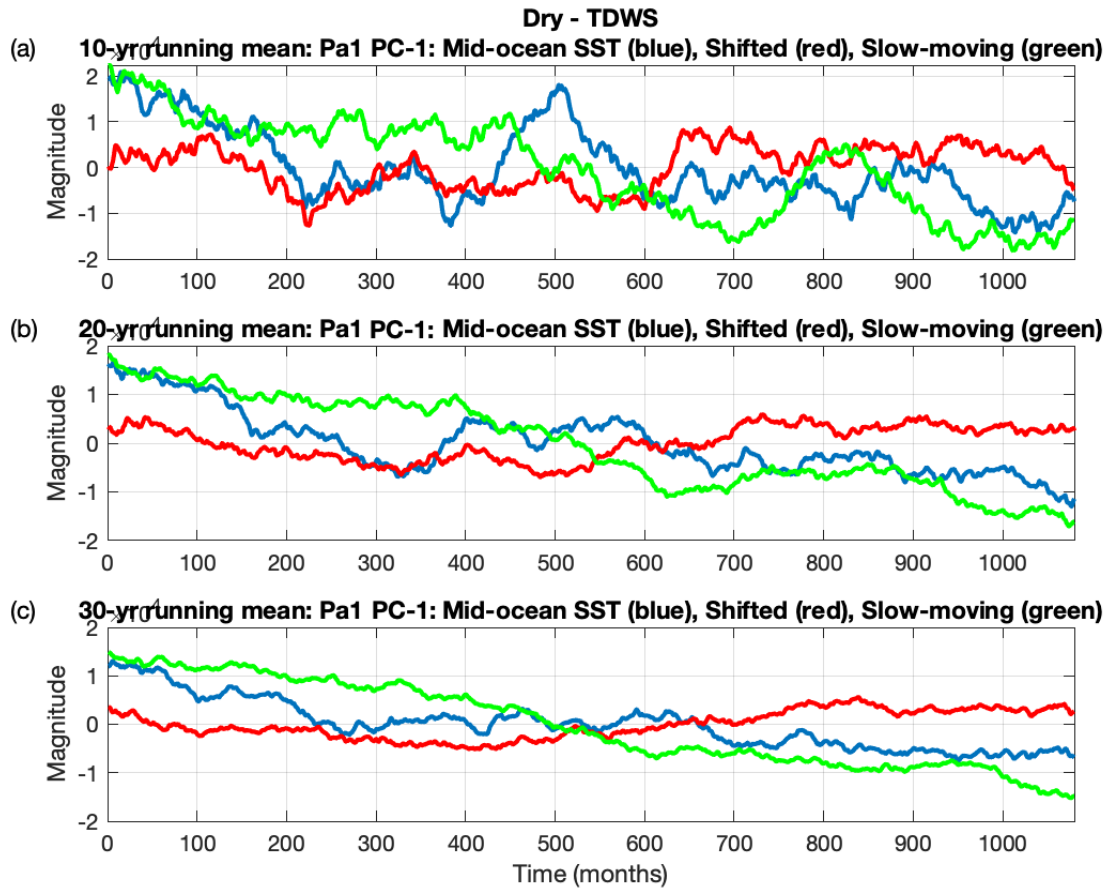


Figure 34 - Lower-layer streamfunction's (dimensional) PC-1 from the dry model version with TDWS parametrization for the data smoothed using: (a) 10-year boxcar running mean, (b) 20-year boxcar running mean, and (c) 30-year boxcar running mean.

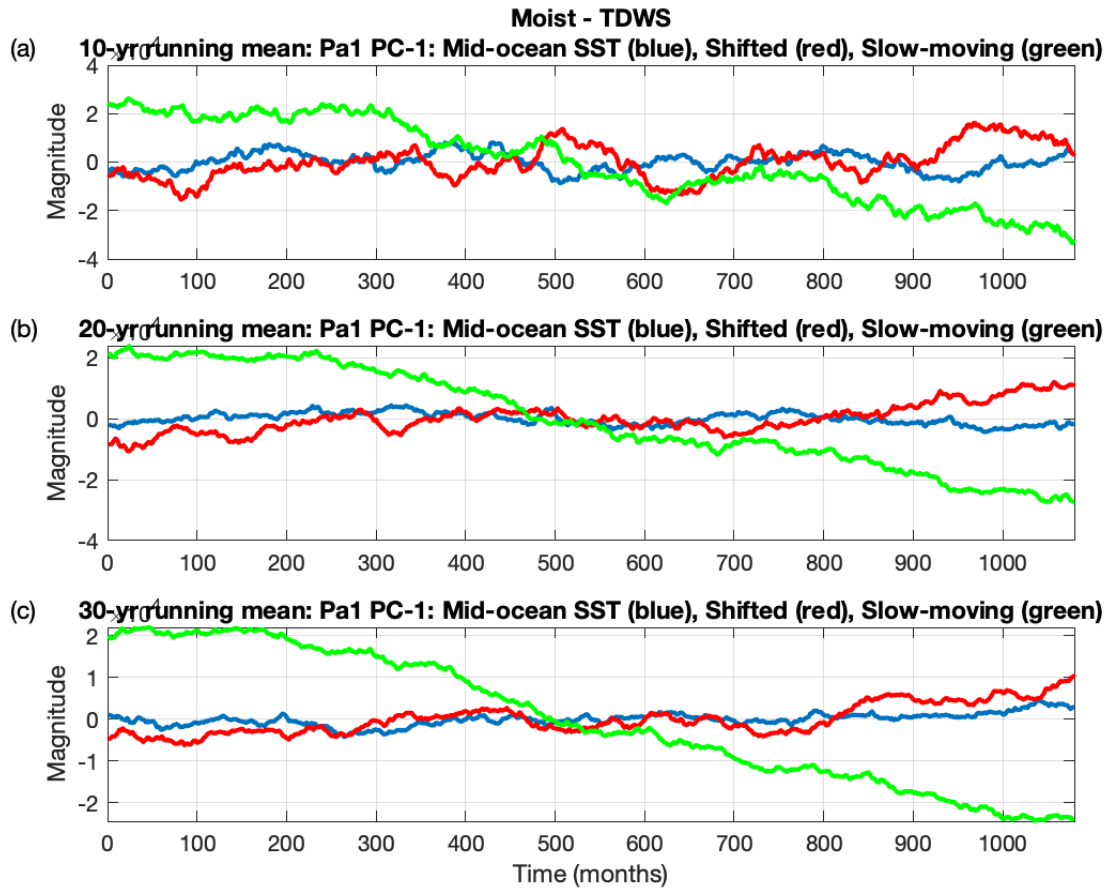


Figure 35 - Same as Fig. 34 but from the moist version of the model with TDWS.

### 5.2.3 Periodic SST front experiments

Designing the experiments with sinusoidal changes in the SST front position, as described below in this section, have the advantage of the forced signal being clearly identifiable in the background of a substantial internal jet-shifting variability of the Q-GCM atmosphere (cf. Section 5.2.2). In these experiments, we used the following variable SST front, which migrates back and forth around the central latitude  $y_0$  with the amplitude of  $A = 500$  km and period  $T_p = 3$  yr :

$$T(y) = 7 \arctan \left( \frac{1}{\Delta y} \left[ -(y - y_0) + A \sin \left( \frac{2\pi t}{T_p} \right) \right] \right) - \frac{0.03}{\Delta y} (y - y_0), \quad (38)$$

where  $y$  is the latitudinal distance,  $t$  is time and  $\Delta y = 10$  km (see Fig. 36). We performed 50-yr-long experiments using, again, dry and moist atmosphere-only versions of Q-GCM model with coarse/high (120/40 km) horizontal resolutions, with and without TDWS parameterization.

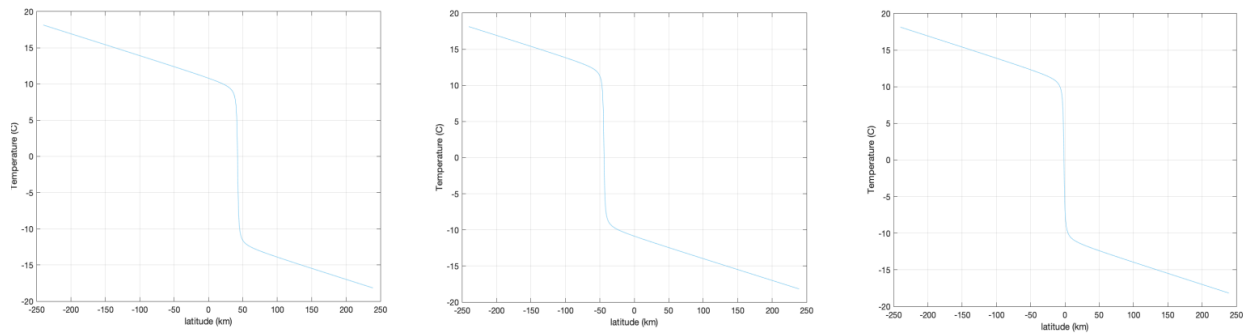


Figure 36 – Cross section of the SST front along the  $y$  axis for the amplitude  $A = 500$  km and period  $T_p=3$  years (equation 38) at: the first year (left plot), the second year (middle plot), and third year (right plot) of simulation, with  $y_0$  set to zero.

In view of the large internal variability associated with jet shifts, which masks the forced migrations of the jet latitude (Section 5.2.2), we smoothed the model output using a one-year

boxcar running mean filter prior to analyzing these simulations using the EOF analysis (note that this is a much shorter smoothing window than the one used to isolate the forced response to the slow-moving SST front in Section 5.2.2).

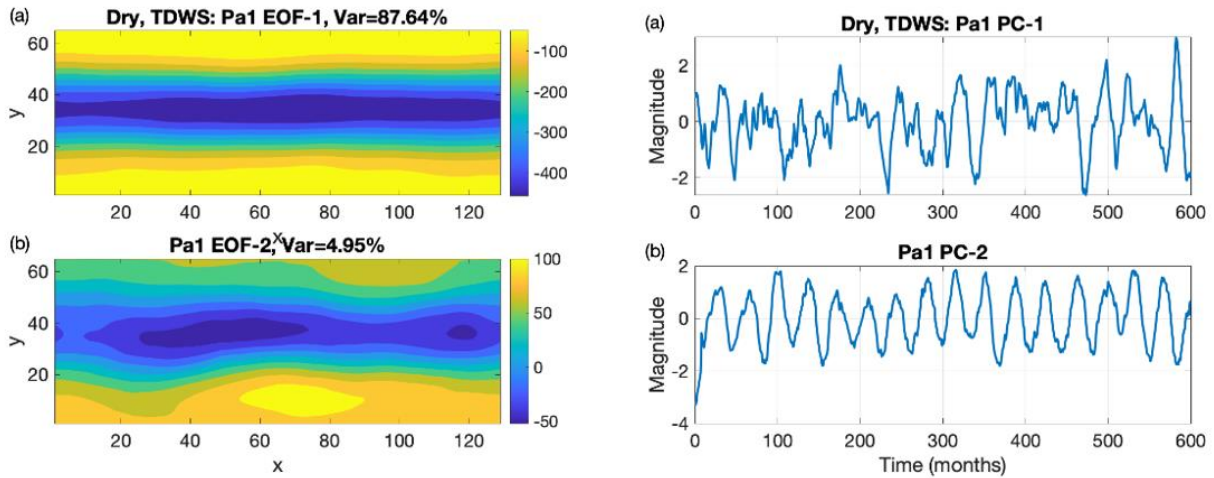


Figure 37 - Leading EOFs of lower-layer dynamic pressure from the periodic-front simulation using the dry version of Q-GCM model with TDWS parametrization: Left: EOF 1 and 2 patterns; right: the corresponding PC time series. Percentages in panel captions indicate the fraction of the total variance accounted for by each EOF.

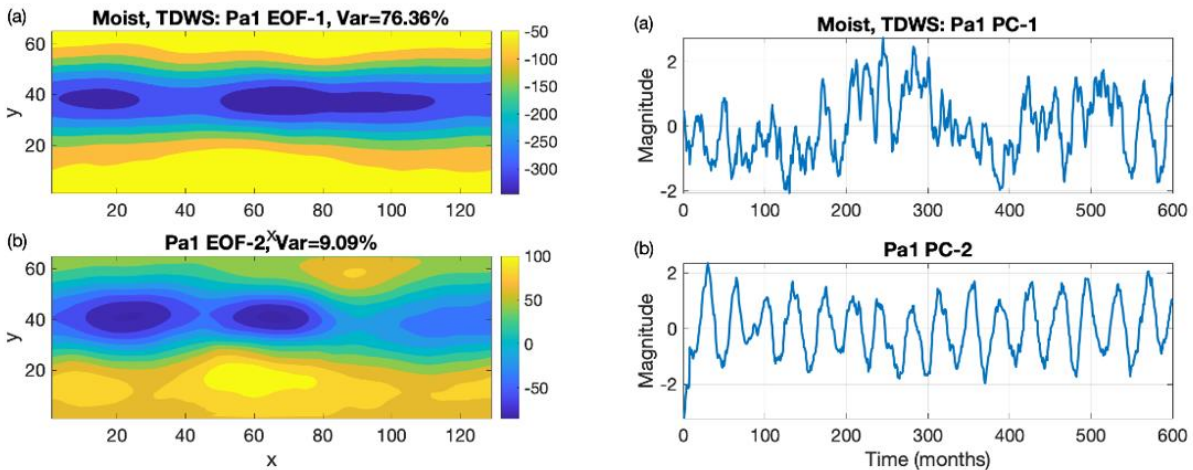


Figure 38 - Same as in Fig. 36 but from the simulation using the moist version of the Q-GCM with TDWS parametrization.

The leading EOF of the dry-model simulation with TDWS parameterization has a jet-shifting pattern and an irregular red-noise-like time series (Fig. 37, upper panels), most likely reflecting internal variations of the jet position. The forced response dominates EOF-2 mode though (Fig. 37, bottom panels), as indicated by a pronounced 3-yr periodicity of its PC time series. The pattern of EOF-2 is orthogonal to that of EOF-1 by construction, although the visible lack of periodic component in the PC-1 time series argues that the forced response is indeed, physically, distinct in its spatial signature from the dominant internal variability. In the dry version of the model, this forced response only accounts for about 5% of the total variance, and measures, in magnitude, at about 6% of the jet-shifting variance associated with EOF-1, which demonstrates an extremely low signal-to-noise ratio of jet-shifting variability in the dry version of the model.

Results from the moist version of the model (Fig. 38) are qualitatively analogous but feature a lower variance of the internal jet-shifting EOF-1 and a higher variance of the forced signal, leading to a signal-to-noise ratio of  $9/76 \times 100\% = 12\%$ , which is about twice as high as that in the dry model, but still very low. We therefore conclude that (i) the free atmosphere is sensitive to the periodically shifting SST front, even in the coarse-resolution experiments; and (ii) this sensitivity, expressed through signal-to-noise ratio is higher in the moist version of the model, but is still very low. We will argue in Section 6 that developing a fully nonlinear self-consistent version of the latent-heat driven entrainment parameterization (see the discussion at the end of Section 4.1) might substantially increase the atmospheric sensitivity to front-like SST anomalies, which is a part of our plans for future work.

# Chapter 6

## 6. Summary, conclusions, and outlook

### 6.1 Summary and discussion

In this work, we hypothesized that the climate system may possess internal climate modes due to multi-scale ocean–atmosphere interactions involving (i) decadal variations in the meridional location and magnitude of the narrow (mesoscale, 100-km wide) sea-surface temperature (SST) fronts associated with the eastward-jet extension of oceanic western boundary currents (such as Gulf Stream); (ii) mesoscale response of the atmospheric planetary boundary layer (APBL) winds and, most importantly, ensuring large-scale (basin-scale-to-global-scale) response of the free atmosphere to these mesoscale SST anomalies; and (iii) subsequent modifications in the large-scale oceanic wind-driven gyres and further changes in the location and/or magnitude of the SST fronts. Individual dynamical elements of such a hypothetical mode have been extensively studied before, with a wealth of literature on oceanic and atmospheric, largely quasi-geostrophic turbulence of the mid-latitude atmospheric jet and the oceanic wind-driven circulation (Berloff, P. and McWilliams, 1999a; Hogg et al., 2005; Berloff et al., 2007; Shevchenko et al., 2016), as well as on the atmospheric response to ocean-induced large-scale and mesoscale SST anomalies, including, in particular the effect of the latter anomalies on the atmospheric jet stream and storm tracks (Miller and Schneider, 2000; Nakamura et al., 2008; Kelly et al., 2010; Small et al., 2014; Ma et al., 2015, 2017, O’Reilly et al., 2017; Kuwano-Yoshida and Minobe, 2017 among many others). Yet, the unambiguous demonstration of a concerted action of these elements to result in the coherent decadal and longer internal climate variability



has remained elusive, partly because modeling these dynamics requires at least semi-hemispheric-extent coupled ocean–atmosphere climate models with high horizontal resolution in both fluids; long, multidecadal simulations using these models are challenging to achieve due to their enormous computational expense.

The goal of this work was to test our hypothesis above in a more idealized, numerically efficient model, yet the one containing the requisite dynamics required in the elements (i), (ii), (iii) of the proposed multi-scale coupled decadal climate modes. The model versions we developed and used here (see Chapters 2 and 4) are based on the Quasi-Geostrophic Coupled Model (Q-GCM) of Hogg et al., 2003, 2006, 2009, 2014, which was revamped and modified to include a parameterized effect of SST anomalies on APBL wind, a new radiation/heat exchange parameterization meant to invigorate the coupling between the surface and free atmosphere, and, finally, the moisture dynamics and the associated latent heat sources that are likely to be essential in the large-scale atmospheric response to mesoscale SST anomalies; the moist model version was dubbed the MQ-GCM model. Despite these modifications, we have to report that we did not thus far identify, in this model, the parameter regime conducive to the multi-scale coupled ocean–atmosphere modes we were looking for. The two main stumbling blocks we encountered were the inability of the ocean model to produce persistent self-sustained meridional shifts of the midlatitude SST front implied in (i), and the weak forced response of the model’s free atmosphere to variable SST fronts, even in the MQ-GCM model, which affects leg (ii) of the proposed feedback sequence. Section 6.2 below contains suggestions for future work to rectify these issues.

The dynamical core of the present (M)Q-GCM model is identical to that of the original Q-GCM model, which has already been used in a suite of studies addressing mid-latitude climate variability, while some of our newly added physics elements have been tested and verified in ocean-only or atmosphere-only settings (e.g., temperature-dependent wind stress: Feliks et al., 2004, 2007; Hogg et al., 2009) or are largely analogous, in their numerical formulation, to the previous Q-GCM elements (e.g., the moisture advection and time stepping scheme is analogous to that of the mixed-layer temperature), or are borrowed from similar ocean-only or coupled models (e.g., our evaporation/precipitation parameterizations have elements borrowed Deremble et al., 2012, 2013). The novelty of the present model is that all these elements are brought together in a fully coupled setting, which makes it a unique numerically efficient tool for exploring possible dynamics of the midlatitude coupled climate variability. While of intermediate complexity, the model is still fairly involved, and no reference analytical solutions to directly verify the accuracy of its numerical implementation are available.

Our explorations started with introducing a temperature-dependent wind-stress (TDWS) parameterization (based on earlier work of Feliks et al., 2004, 2007 and Hogg et al., 2009) to the original version of Q-GCM model and performing the control and TDWS-parameterization-enhanced simulations in the oceanic eddy-permitting regime (at 10-km resolution) under both standard (120-km) and high (20-km) atmospheric resolutions (Section 3.1). While we did find a novel interannual mode centrally involving TDWS coupling, this mode was primarily associated with the coupled behavior of the atmosphere and surface ocean mixed layer, rather than mesoscale SST anomalies induced by internal oceanic quasi-geostrophic turbulence. Furthermore, the TDWS coupling resulted in the suppression of the latter turbulence in the

ocean, leading in turn to the dilution of mesoscale SST fronts and, thus eliminating the potential for the proposed multi-scale coupled modes. Accordingly, the model behavior did not differ between the versions using standard or high atmospheric resolution within a given setup (with or without TDWS coupling).

To address the unrealistic suppression of the oceanic turbulence we developed a partially coupled model configuration (Section 2.3.3), in which the TDWS wind corrections are only felt by the atmosphere, with the ocean “seeing” the AML winds computed in the absence of such corrections. Of course, this partially coupled setup does not fully address the necessity to explore more turbulent oceanic regimes in the fully mesoscale-coupled model by increasing the oceanic resolutions and Reynolds numbers, but it provides much needed computational efficiency and permits to complete multiple multi-centuries coupled simulations in a reasonable time. However, even these partially (mesoscale-)coupled experiments with the original (apart from the TDWS parameterization) Q-GCM model, while preserving realistic levels of oceanic turbulence and reasonable SST fronts in the partially coupled TDWS simulation, still did not manage to produce any substantial differences in the decadal+ atmospheric variability between these simulations and the control simulation without TDWS, *irrespective* of the atmospheric model resolution.

It is the latter less desired outcome that prompted the development of a modified Q-GCM version with constant-depth AML formulation and a new radiative-convective transfer formulation (Chapter 2). Unfortunately, the control and partially coupled versions of TDWS simulations of the Q-GCM model so modified produced, once again, very similar results irrespective of the atmospheric horizontal resolution, meaning that the Q-GCM modifications

we introduced did not result in the emergence of the new multi-scale decadal climate modes in the model used (these results are not shown in the main text, as they are analogous to those presented in Section 4.2 for the moist version of the model; see below). The apparent lack of atmospheric sensitivity to mesoscale coupling (including non-linear sensitivity associated with potential atmospheric regime behavior; Section 3.2) and atmospheric model resolution motivated the development of the moist version of the model, MQ-GCM (Chapter 4; Section 4.1).

However, repeating the control, TDWS, and partially coupled simulations with MQ-GCM did not produce any detectable changes in the low-frequency variability of the model's free atmosphere — which would be a proxy indicator of the multi-scale coupled dynamics at work — either, again, irrespective of the atmospheric model resolution (Section 4.2). In fact, the behaviors of the dry and moist versions of the model turned out to be visually very similar (figures not shown here).

This situation persisted in the models with the ocean configuration at higher horizontal resolution (of 5 km), lateral (mixed) boundary conditions closer to the free-slip setup (following Martin et al., 2020) and an alternative ocean stratification (Kurashina and Berloff, 2023), all of which were explored as a potential way of enhancing the oceanic turbulence and eddy-driven jet coherence in the present model (Section 5.1). After all, it still seems to be the case that the ocean module of our coupled model is unable to produce more persistent eastward-ocean-jet-extension shifts and the resulting shifts in the meridional location of the SST front at the confluence of the oceanic western boundary currents as the leading mode of oceanic variability. Rectifying this behavior is therefore an important area for further research (see Section 6.2).

Assuming the configuration with persistent internally generated meridional displacements of SST front at the boundary between the subtropical and subpolar ocean gyres is a possibility, another area for further studies is the forced response of the free atmosphere to such displacements. We took initial steps in quantifying this response by performing the atmosphere-only simulations under fixed-position (Sections 3.3 — original Q-GCM, 5.2.1 — modified Q-GCM) and time-varying SST fronts (modified atmospheric component of Q-GCM and MQ-GCM models, under latitudinally shifting SST fronts, with linear trend or periodic time dependence; Sections 5.2.2 and 5.2.3, respectively). These experiments followed analogous studies by Feliks et al., 2004, 2007, 2011, Brachet et al., 2012, as well as Deremble et al., 2012.

We showed that the Q-GCM's atmospheric climatological jet's position is strongly attracted to the pre-specified location of the SST front, which is formally analogous to the conclusion of Deremble et al., 2012. However, these authors attribute the controlling influence of the SST front on the atmospheric jet to the moist atmospheric dynamics and latent-heat forcing of the atmospheric interior in the vicinity of the front. By contrast, we identify similar climatological effects of the SST front location in *all* versions of Q-GCM model, including the original dry version with and without TDWS feedbacks (Section 3.3), as well as both the dry and moist versions of the modified the Q-GCM model (Section 5.2.1), once again, *irrespective* of the model's horizontal resolution. We thus conclude that these differences are likely to result from large-scale redistribution of the atmospheric surface heat-flux forcing redistribution, rather than the response of the AML winds to SST anomalies and the associated moist dynamics.

While the meridional location of the jet is sensitive to the SST front's position, the atmospheric jet's variability around this mean state is not; furthermore, this variability is very similar in the

simulations with the standard (coarse) and high atmospheric resolutions. This behavior is in contrast to the one reported by Feliks et al., 2004, 2007, where the internal atmospheric variability above the SST front underwent qualitative and quantitative large-scale changes depending on whether the front was well resolved by the atmospheric model or not. These authors argued, however, that under-resolved SST front experiments could be corrected by artificially augmenting the mesoscale forcing associated with the front (such a correction is also implicit in the tuning of the vertical moisture fluxes in the coarse-resolution model of Deremble et al., 2012). One possible reason behind the discrepancy between their results and our results reported here is that the atmospheric mixed layer in Feliks et al. formulation is assumed to be in equilibrium with SST, whereas our more independent atmospheric mixed layer is unable to produce a sufficiently strong Ekman pumping of the atmospheric interior in the vicinity of the SST front. Possible future steps in addressing this hypothesis are discussed below in Section 6.2. Alternatively — and this is the explanation we lean towards — the Feliks et al. model and our model are explored in very different parameter regimes, with their regime closer to the roots of the bifurcation tree leading to the fully developed quasi-geostrophic turbulence and our regime well within the latter turbulent parameter range. Hence, Feliks et al. are able to document more sensitivity to model parameters (including the model resolution) in their more deterministic (and, statistically, more sensitive) parameter range, then there actually is in a more chaotic regime further “up” the bifurcation tree.

One promising result of Section 5.2 concerns the role of moist processes in the Q-GCM model in amplifying the forced jet-shift signal over the internally generated, random atmospheric jet shifts, as expressed through the signal-to-noise ratio: this ratio is the highest in the moist

version of the model with added TDWS parametrization. The enhancement of the signal-to-noise ratio is significant, but still fairly small, which may be related to some shortcuts we undertook in developing the parameterization for the latent-heat driving of the atmospheric interior; possible improvements in this parameterization discussed in the next section is another promising direction for future work.

## 6.2. Future directions

Within our hypothesis put forward in Section 6.1, the key ingredient of the proposed multi-scale coupled variability is the ocean model's ability to produce and maintain persistent (decadal) meridional shifts of the western boundary currents' eastward-jet extensions and the associated persistent perturbations in the position of SST front between oceanic subtropical and subpolar gyres. We couldn't find such a parameter regime in our coupled model, and this argues for the need of a more extensive parameter sensitivity analysis of an ocean model to do so.

Another aspect of the current model formulation that needs improvement regards the (currently excessively weak) communication between the AML and the atmospheric interior, possibly rooted in the self-consistent parameterization of latent-heat based entrainment rates between the atmospheric interior layers; stronger rates would lead to stronger free-atmospheric forced response to the oceanic variability. Recall that the current version of the MQ-GCM model uses "dry" estimates of these entrainment rates (Section 4.1) in computing the

moisture vertical fluxes and condensation rates within each QG layer. This makes it very likely that all of these fluxes are underestimated, as the latent heat release can most definitely contribute strongly to and modify the entrainment rates as well. One way to improve the current formulation is by iterating the solution of the moisture equations at a given time step to achieve mutually consistent estimates of both precipitation and entrainment in the interior QG layers. This way, the interior entrainment fluxes at a given iteration would be used, along with the fixed advective and diffusive fluxes, to update the interior humidity and compute the precipitation rates until these rates (and entrainment rates) converge to a steady solution which would, we believe, lead to the more prominent effects of the moist processes and thus increase the signal to noise ratio in the free atmosphere.

Another interesting possibility, especially given the fast development of the AI/ML techniques and methods in geosciences, is to replace the atmospheric formulation in Q-GCM by a statistical model trained using SST, near-surface atmospheric temperature and surface wind data from the latest high-resolution satellite observations or output of high-resolution state-of-the-art regional or global climate models. For example, Bodner and Zanna, 2022 used the high-resolution ocean model output and chose different regions over the global ocean to train the Neural Network to predict the subgrid sub mesoscale-induced vertical fluxes as a function of relevant coarse-resolution variables.” For our purposes, an analogous procedure would be used to derive a model that predicts, given a current distribution of SST, near-surface atmospheric temperature, and surface wind, the distributions of the atmospheric variables at the next time step, to be combined with the SST predictions by the ocean component of Q-GCM to provide the surface momentum and heat fluxes and, therefore, the next-time-step forcing for the ocean



model. This hybrid model would thus make use of the empirically derived connections between SST and multi-scale atmospheric anomalies in the background of the stochastically forced internal atmospheric variability.

## References

Arzel, O., and T. Huck: Decadal oscillations in a simplified coupled model due to unstable interactions between zonal winds and ocean gyres. *Dyn. Atmos. Oceans*, 37, 245–270, <https://doi.org/10.1016/j.dynatmoce.2003.08.001>, 2003.

Barsugli, J. J. and Battisti, D. S.: The basic effects of atmosphere–ocean thermal coupling on midlatitude variability, *J. Atmos. Sci.*, 55, 477–493, [https://doi.org/10.1175/1520-0469\(1998\)055%3C0477:TBEAOA%3E2.0.CO;2](https://doi.org/10.1175/1520-0469(1998)055%3C0477:TBEAOA%3E2.0.CO;2), 1998.

Berloff P. and McWilliams J.: Quasigeostrophic dynamics of the western boundary current. *J Phys Oceanogr* 29:2607–2634, [https://doi.org/10.1175/1520-0485\(1999\)029%3C2607:QDOTWB%3E2.0.CO;2](https://doi.org/10.1175/1520-0485(1999)029%3C2607:QDOTWB%3E2.0.CO;2), 1999b.

Berloff, P. and McWilliams, J.: Large-scale low-frequency variability in wind-driven ocean gyres, *J. Phys. Oceanogr.*, 29, 1925–1949, [https://doi.org/10.1175/1520-0485\(1999\)029%3C1925:LSLFVI%3E2.0.CO;2](https://doi.org/10.1175/1520-0485(1999)029%3C1925:LSLFVI%3E2.0.CO;2), 1999a.

Berloff, P., Hogg, A., and Dewar, W.: The turbulent oscillator: A mechanism of low-frequency variability of wind-driven ocean gyres, *J. Phys. Oceanogr.*, 37, 2363–2386, <https://doi.org/10.1175/JPO3118.1>, 2007.

Bodner, A. S. and Zanna, L., “A Data-Driven Approach for the Submesoscale Parameterization”, vol. 2022, 2022.

Bolton, D.: The computation of equivalent potential temperature, *Mon. Weather Rev.*, 108, 1046–1053, [https://doi.org/10.1175/1520-0493\(1980\)108%3C1046:TCOEPT%3E2.0.CO;2](https://doi.org/10.1175/1520-0493(1980)108%3C1046:TCOEPT%3E2.0.CO;2), 1980.

Brachet, S., Codron, F., Feliks, Y., Ghil, M., Le Treut, H., and Simonnet, E.: Atmospheric circulations induced by a midlatitude SST front: a GCM study, *J. Climate*, 25, 1847–1853, <https://doi.org/10.1175/JCLI-D-11-00329.1>, 2012.

Brown, P.T., M. S. Lozier, M. S., R. Zhang, and W. Li: The necessity of cloud feedback for a basin-scale Atlantic Multidecadal Oscillation, *Geophys. Res. Lett.*, 43, 3955–3963, <https://doi.org/10.1002/2016GL068303>, 2016.

Bryan, F. O., Tomas, R., Dennis, J. M., Chelton, D. B., Loeb, N. G., and McClean, J. L.: Frontal scale air–sea interaction in high-resolution coupled climate models, *J. Climate*, 23, 6277–6291, <https://doi.org/10.1175/2010JCLI3665.1>, 2010.

Chang, P., and Coauthors, 2020: An unprecedented set of high-resolution Earth system simulations for understanding multiscale interactions in climate variability and change. *J. Adv. Model. Earth Syst.*, 12, e2020MS002298, <https://doi.org/10.1029/2020MS002298>, 2020.

Chelton D.: Ocean–atmosphere coupling: Mesoscale eddy effects, *Nat. Geosci.*, 6, 594–595, <https://doi.org/10.1038/ngeo1906>, 2013.

Chelton, D. and Coauthors: Observations of coupling between surface wind stress and sea surface temperature in the eastern tropical Pacific. *J. Climate*, 14, 1479–1498, [https://doi.org/10.1175/1520-0442\(2001\)014%3C1479:OOCBSW%3E2.0.CO;2](https://doi.org/10.1175/1520-0442(2001)014%3C1479:OOCBSW%3E2.0.CO;2), 2001.

Chelton, D. and Xie, S.-P.: Coupled ocean-atmosphere interaction at oceanic mesoscales, *Oceanography*, 23, 52–69, <https://doi.org/10.5670/oceanog.2010.05>, 2010.

Chelton, D., M. G. Schlax, M. H. Freilich, and R. F. Milliff: Satellite measurements reveal persistent small-scale features in ocean winds. *Science*, 303, 978–983, <https://doi.org/10.1126/science.1091901>, 2004.

Czaja, A. and Blunt, N.: A new mechanism for ocean–atmosphere coupling in midlatitudes, *Q. J. Roy. Meteor. Soc.*, 137, 1095–1101, 2011.

Czaja, A. and Marshall, J.: Observations of atmosphere–ocean coupling in the North Atlantic, *Q. J. Roy. Meteor. Soc.*, 127, 1893–1916, <https://doi.org/10.1002/qj.49712757603>, 2001.

Czaja, A., C. Frankignoul, S. Minobe, and B. Vanniere: Simulating the midlatitude atmospheric circulation: What might we gain from high-resolution modeling of air–sea interactions? *Curr. Climate Change Rep.*, 5, 390–406, <https://doi.org/10.1007/s40641-019-00148-5>, 2019.

Deremble B., Hogg A., Berlof P., and Dewar W. K.: On the application of no-slip lateral boundary conditions to ‘coarsely’ resolved ocean models. *Ocean Model* 39(3–4):411–415, <https://doi.org/10.1016/j.ocemod.2011.05.002>, 2011

Deremble, B., Lapeyre, G., and Ghil, M.: Atmospheric Dynamics Triggered by an Oceanic SST Front in a Moist Quasigeostrophic Model, *J. Atmos. Sci.*, 69, 1617–1632, <https://doi.org/10.1175/JAS-D-11-0288.1>, 2012.

Deremble, B., Wienders, N., and Dewar, W. K.: CheapAML: a simple atmospheric boundary layer model for use in ocean-only calculations, *Mon. Weather Rev.*, 141, 12, <https://doi.org/10.1175/MWR-D-11-00254.1>, 2013.

Deser, C. and Blackmon, M. L.: Surface climate variations over the North Atlantic Ocean during winter: 1900–1989, *J. Climate*, 6, 1743–1753, [https://doi.org/10.1175/1520-0442\(1993\)006%3C1743:SCVOTN%3E2.0.CO;2](https://doi.org/10.1175/1520-0442(1993)006%3C1743:SCVOTN%3E2.0.CO;2), 1993.

Dewar, W. and Flierl, G.: Some effects of the wind on rings, *J. Phys. Oceanogr.*, 17, 1653–1667, [https://doi.org/10.1175/1520-0485\(1987\)017%3C1653:SEOTWO%3E2.0.CO;2](https://doi.org/10.1175/1520-0485(1987)017%3C1653:SEOTWO%3E2.0.CO;2), 1987.

Eade, R., D. Smith, A. Scaife, E. Wallace, N. Dunstone, L. Hermanson, and N. Robinson: Do seasonal-to-decadal climate predictions underestimate the predictability of the real world? *Geophys. Res. Lett.*, 41, 5620–5628, <https://doi.org/10.1002/2014GL061146>, 2014.

Evan, A. T., R. J. Allen, R. Bennartz, and D. J. Vimont: The modification of sea surface temperature anomaly linear damping time scales by stratocumulus clouds, *J. Climate*, 26, 3619–3630, <https://doi.org/10.1175/JCLI-D-12-00370.1>, 2013.

- Fan, M. and Schneider, E. K.: Observed Decadal North Atlantic Tripole SST Variability. Part I: Weather Noise Forcing and Coupled Response, *J. Atmos. Sci.*, 69, 35– 50, <https://doi.org/10.1175/JAS-D-11-018.1>, 2012.
- Feliks, Y., Ghil, M., and Robertson, A. W.: The atmospheric circulation over the North Atlantic as induced by the SST field, *J. Climate*, 24, 522–542, <https://doi.org/10.1175/2010JCLI3859.1>, 2011.
- Feliks, Y., Ghil, M., and Simonnet, E.: Low-frequency variability in the midlatitude atmosphere induced by an oceanic thermal front, *J. Atmos. Sci.*, 61, 961, [https://doi.org/10.1175/1520-0469\(2004\)061%3C0961:LVTMA%3E2.0.CO;2](https://doi.org/10.1175/1520-0469(2004)061%3C0961:LVTMA%3E2.0.CO;2), 2004.
- Feliks, Y., Ghil, M., and Simonnet, E.: Low-frequency variability in the midlatitude baroclinic atmosphere induced by an oceanic thermal front, *J. Atmos. Sci.*, 64, 97–116, <https://doi.org/10.1175/JAS3780.1>, 2007.
- Ferreira, D., C. Frankignoul, and J. Marshall: Coupled Ocean–atmosphere dynamics in a simple midlatitude climate model. *J. Climate*, 14, 3704–3723, [https://doi.org/10.1175/1520-0442\(2001\)014%3C3704:COADIA%3E2.0.CO;2](https://doi.org/10.1175/1520-0442(2001)014%3C3704:COADIA%3E2.0.CO;2), 2001.
- Foussard, A., Lapeyre, G., and Plougonven, R.: Storm Track Response to Oceanic Eddies in Idealized Atmospheric Simulations, *J. Climate*, 32, 445–463, <https://doi.org/10.1175/JCLI-D-18-0415.1>, 2019.
- Frankignoul, C. and Hasselmann, K.: Stochastic climate models, part II: Application to sea-surface temperature anomalies and thermocline variability, *Tellus*, 29A, 289–305, <https://doi.org/10.1111/j.2153-3490.1977.tb00740.x>, 1977.
- Frankignoul, C.: Sea surface temperature anomalies, planetary waves, and air-sea feedback in the middle latitudes, *Rev. Geophys.*, 23, 357–390, <https://doi.org/10.1029/RG023i004p00357>, 1985.
- Frenger, I., Gruber, N., Knutti, R., and Munnich, M.: Imprint of Southern Ocean eddies on winds, clouds and rainfall, *Nat. Geosci.*, 6, 608–612, <https://doi.org/10.1038/ngeo1863>, 2013.
- Gaube, P., Chelton, D. B., Samelson, R. M., Schlax, M. G., and O’Neill, L. W.: Satellite observations of mesoscale eddy-induced Ekman pumping, *J. Phys. Oceanogr.*, 45, 104–132, <https://doi.org/10.1175/JPO-D-14-0032.1>, 2015.
- Gaube, P., Chelton, D. B., Strutton, P. G., and Behrenfeld, M. J.: Satellite observations of chlorophyll, phytoplankton biomass, and Ekman pumping in nonlinear mesoscale eddies, *J. Geophys. Res.*, 118, 6349–6370, <http://dx.doi.org/10.1002/2013JC009027>, 2013.
- Gill, A. E.: *Atmosphere–Ocean Dynamics*, Academic Press, 662 pp., ISBN 9780122835223, eBook ISBN 9780080570525, 1982.
- Haidvogel D, McWilliams J, Gent P.: Boundary current separation in a quasigeostrophic, eddy-resolving ocean circulation model. *J Phys Oceanogr* 22:882–902, [https://doi.org/10.1175/1520-0485\(1992\)022%3C0882:BCSIAQ%3E2.0.CO;2](https://doi.org/10.1175/1520-0485(1992)022%3C0882:BCSIAQ%3E2.0.CO;2), 1992.

- Hasselmann, K.: Stochastic climate models: Part I. Theory, *Tellus*, 28A, 473–485, <http://dx.doi.org/10.3402/tellusa.v28i6.11316>, 1976.
- Hayasaki, M., R. Kawamura, M. Mori, and M. Watanabe: Response of extratropical cyclone activity to the Kuroshio large meander in northern winter. *Geophys. Res. Lett.*, **40**, 2851–2855, <https://doi.org/10.1002/grl.50546>, 2013.
- Hirata, H., R. Kawamura, M. Nonaka, and K. Tsuboki: Significant impact of heat supply from the Gulf Stream on a “superbomb” cyclone in January 2018. *Geophys. Res. Lett.*, 46, 7718–7725, <https://doi.org/10.1029/2019GL082995>, 2019.
- Hogg, A. M. and Blundell, J. R.: Interdecadal variability of the Southern Ocean, *J. Phys. Oceanogr.*, 36, 1626–1645, <https://doi.org/10.1175/JPO2934.1>, 2006.
- Hogg, A. M., Blundell, J. R., Dewar, W. K., and Killworth, P. D.: Formulation and users’ guide for Q-GCM, Version 1.5.0, <http://www.q-gcm.org/downloads/q-gcm-v1.5.0.pdf>, 2014.
- Hogg, A. M., Dewar, W. K., Berloff, P. S., Kravtsov, S., and Hutchinson, D. K.: The effects of mesoscale ocean-atmosphere coupling on the large-scale ocean circulation, *J. Climate*, 22, 4066–4082, <http://dx.doi.org/10.1175/2009JCLI2629.1>, 2009.
- Hogg, A. M., Dewar, W. K., Killworth, P. D., and Blundell, J. R.: A quasigeostrophic coupled model (Q-GCM), *Mon. Weather Rev.*, 131, 2261–2278, [http://dx.doi.org/10.1175/1520-0493\(2003\)131%3C2261:AQCMQ%3E2.0.CO;2](http://dx.doi.org/10.1175/1520-0493(2003)131%3C2261:AQCMQ%3E2.0.CO;2), 2003.
- Hogg, A. M., Dewar, W. K., Killworth, P. D., and Blundell, J. R.: Decadal variability of the midlatitude climate system driven by the ocean circulation, *J. Climate*, 19, 1149–1166, <https://doi.org/10.1175/JCLI3651.1>, 2006.
- Hogg, A. M., Killworth, P. D., Blundell, J. R., and Dewar, W. K.: Mechanisms of decadal variability of the wind-driven ocean circulation, *J. Phys. Oceanogr.*, 35, 512–531, <https://doi.org/10.1175/JPO2687.1>, 2005.
- Hogg, A. M., Killworth, P. D., Blundell, J. R., and Dewar, W. K.: Low Frequency Ocean Variability: Feedbacks Between Eddies and the Mean Flow, in: *Turbulence and Coherent Structures in Fluids, Plasmas and Granular Flows*, edited by: Fredriksen, J. and Denier, J., 171–185, World Scientific, [http://dx.doi.org/10.1142/9789812771025\\_0007](http://dx.doi.org/10.1142/9789812771025_0007), 2007.
- Hogg, A. M., Meredith, M. P., Blundell, J. R., and Wilson, C.: Eddy heat flux in the Southern Ocean: Response to variable wind forcing, *J. Climate*, 21, 608–620, <https://doi.org/10.1175/2007JCLI1925.1>, 2008.
- Hutchinson, D. K., Hogg, A. McC., and Blundell, J. R.: Southern Ocean response to relative velocity wind stress forcing, *J. Phys. Oceanogr.*, 40, 326–339, <https://doi.org/10.1175/2009JPO4240.1>, 2010.
- Infanti, J. M., and B. P. Kirtman: A comparison of CCSM4 high-resolution and low-resolution predictions for south Florida and southeast United States drought. *Climate Dyn.*, 52, 6877–6892, <https://doi.org/10.1007/s00382-018-4553-0>, 2019.

Jin X, Dong C, Kurian J, McWilliams J, Chelton D, Li Z.: SST–wind interaction in coastal upwelling: Oceanic simulation with empirical coupling. *J. Phys. Oceanogr.*39: 2957– 2970, <https://doi.org/10.1175/2009JPO4205.1>, 2009.

Jin, F-F.: A theory of interdecadal climate variability of the North Pacific ocean–atmosphere system. *J. Climate*, 10, 1821–1835, [https://doi.org/10.1175/1520-0442\(1997\)010%3C1821:ATOICV%3E2.0.CO;2](https://doi.org/10.1175/1520-0442(1997)010%3C1821:ATOICV%3E2.0.CO;2), 1997.

Joyce, T. M., Y.-O. Kwon, H. Seo, and C. C. Ummenhofer: Meridional Gulf Stream shifts can influence wintertime variability in the North Atlantic storm track and Greenland blocking. *Geophys. Res. Lett.*, 46, 1702–1708, <https://doi.org/10.1029/2018GL081087>, 2019.

Kelly, K. A., Small, R. J., Samelson, R. M., Qiu, B., Joyce, T. M., Kwon, Y., and Cronin, M. F.: Western Boundary Currents and Frontal Air–Sea Interaction: Gulf Stream and Kuroshio Extension, *J. Climate*, 23, 5644–5667, <https://doi.org/10.1175/2010JCLI3346.1>, 2010.

Kirtman, B. P., Cecilia Bitz, Frank Bryan, William Collins, John Dennis, Nathan Hearn, James L. Kinter III, Richard Loft, Clement Rousset, Leo Siqueira, Cristiana Stan, Robert Tomas, Mariana Vertenstein: Impact of ocean model resolution on CCSM climate simulations, *Climate Dyn.*, 39, 1303–1328, <http://dx.doi.org/10.1007/s00382-012-1500-3>, 2012.

Koo, S., and M. Ghil: Successive bifurcations in a simple model of atmospheric zonal-flow vacillation. *Chaos*, 12, 300–309, <https://doi.org/10.1063/1.1468249>, 2002.

Kravtsov, S. K., Dewar, W. K., Ghil, M., Berloff, P. S., and McWilliams, J. C.: North Atlantic climate variability in coupled models and data, *Nonlin. Processes Geophys.*, 15, 13–24, <https://doi.org/10.5194/npg-15-13-2008>, 2008.

Kravtsov, S., Berloff, P., Dewar, W. K., Ghil, M., and McWilliams, J. C.: Dynamical origin of low-frequency variability in a highly nonlinear mid-latitude coupled model, *J. Climate*, 19, 6391–6408, <https://doi.org/10.1175/JCLI3976.1>, 2006.

Kravtsov, S., Dewar, W. K., Berloff, P., McWilliams, J. C., and Ghil, M.: A highly nonlinear coupled mode of decadal variability in a mid-latitude ocean–atmosphere model, *Dyn. Atmos.-Oceans*, 43, 123–150, <https://doi.org/10.1016/j.dynatmoce.2006.08.001>, 2007.

Kravtsov, S., Kamenkovich, I., Hogg, A. M., and Peters, J. M.: On the mechanisms of late 20th century sea-surface temperature trends over the Antarctic Circumpolar Current, *J. Geophys. Res.- Oceans*, 116, C11034, <https://doi.org/10.1029/2011JC007473>, 2011.

Kravtsov, S., M. G. Wyatt, J. A. Curry, and A. A. Tsonis: Two contrasting views of multidecadal climate variability in the twentieth century. *Geophys. Res. Lett.*, 41, 6881– 6888, <https://doi.org/10.1002/2014GL061416>, 2014.

Kravtsov, S., Mastilovic, I., Hogg, A. M., Dewar, W. K., Blundell, J. R., and Killworth, P.: MQ-GCM (v2.0.0), Zenodo [code], <https://doi.org/10.5281/zenodo.5250828>, 2021b.

Kravtsov, S., Mastilovic, I., Hogg, A. McC., Dewar, W. K., and Blundell, J. R.: The Moist Quasi-Geostrophic Coupled Model: MQ-GCM 2.0, *Geosci. Model Dev.*, 15, 7449–7469, <https://doi.org/10.5194/gmd-15-7449-2022>, 2022.

Kravtsov, S., Mastilovic, I., Hogg, A., Dewar, W. K., and Blundell, J. R.: MQ-GCM2.0 model, Zenodo [code], <https://doi.org/10.5281/zenodo.4916720>, 2021a.

Kravtsov, S., Robertson, A. W., and Ghil, M.: Bimodal behavior in the zonal mean flow of a baroclinic-channel model, *J. Atmos. Sci.*, 62, 1746–1769, <https://doi.org/10.1175/JAS3443.1>, 2005.

Kravtsov, S.: Pronounced differences between observed and CMIP5 simulated multidecadal climate variability in the twentieth century. *Geophys. Res. Lett.*, 44, 5749– 5757, <https://doi.org/10.1002/2017GL074016>, 2017.

Kravtsov, S., and A. Robertson: Midlatitude ocean-atmosphere interaction in an idealized coupled model. *Climate Dyn.*, 19, 693–711, <http://dx.doi.org/10.1007/s00382-002-0256-6>, 2002.

Kurashina, R., Berloff, P.: Low-frequency variability enhancement of the midlatitude climate in an eddy-resolving coupled ocean–atmosphere model—part II: ocean mechanisms. *Clim Dyn.* <https://doi.org/10.1007/s00382-023-06767-x>, 2023a.

Kurashina, R., Berloff, P.: Low-frequency variability enhancement of the midlatitude climate in an eddy-resolving coupled ocean–atmosphere model. Part I: anatomy. *Clim Dyn.* <https://doi.org/10.1007/s00382-023-06782-y>, 2023b.

Kushnir, Y., W. A. Robinson, I. Bladé, N. M. J. Hall, S. Peng, and R. Sutton: Atmospheric GCM response to extratropical SST anomalies: Synthesis and evaluation. *J. Climate*, 15, 2233–2256, [https://doi.org/10.1175/1520-0442\(2002\)015%3C2233:AGRTES%3E2.0.CO;2](https://doi.org/10.1175/1520-0442(2002)015%3C2233:AGRTES%3E2.0.CO;2), 2002.

Kushnir, Y.: Interdecadal variations in North Atlantic sea surface temperature and associated atmospheric circulation, *J. Climate*, 7, 141–157, <http://www.jstor.org/stable/26197832>, 1994.

Kuwano-Yoshida, A., and S. Minobe: Storm track response to SST fronts in the northwestern Pacific region in an AGCM. *J. Climate*, 30, 1081–1102, <https://doi.org/10.1175/JCLI-D-16-0331.1>, 2017.

Kuwano-Yoshida, A., Minobe, S., and Xie, S.-P.: Precipitation response to the Gulf Stream in an atmospheric GCM, *J. Climate*, 23, 3676–3698, <https://doi.org/10.1175/2010jcli3261.1>, 2010.

Laîné, A., Lapeyre, G., and Rivière, G.: A Quasigeostrophic Model for Moist Storm Tracks, *J. Atmos. Sci.*, 68, 1306–1322, <https://doi.org/10.1175/2011JAS3618.1>, 2011.

Lindzen, R. S. and Nigam, S.: On the role of sea surface temperature gradients in forcing low-level winds and convergence in the tropics, *J. Atmos. Sci.*, 44, 2418–2436, [https://doi.org/10.1175/1520-0469\(1987\)044%3C2418:OTROSS%3E2.0.CO;2](https://doi.org/10.1175/1520-0469(1987)044%3C2418:OTROSS%3E2.0.CO;2), 1987.



- Liu, W., A. V. Fedorov, S.-P. Xie, and S. Hu: Climate impacts of a weakened Atlantic meridional overturning circulation in a warming climate. *Sci. Adv.*, 6, eaaz4876, <https://doi.org/10.1126/sciadv.aaz4876>, 2020.
- Liu, X., and Coauthors: Ocean fronts and eddies force atmospheric rivers and heavy precipitation in western North America. *Nat. Commun.*, 12, 1268, <https://doi.org/10.1038/s41467-021-21504-w>, 2021.
- Ma, X., Chang, P., Saravanan, R., Montuoro, R., Hsieh, J.-S., Wu, D., Lin, X., Wu, L., and Jing, Z.: Distant influence of Kuroshio eddies on North Pacific weather patterns?, *Sci. Rep.-UK*, 5, 17785, <https://doi.org/10.1038/srep17785>, 2015.
- Ma, X., Chang, P., Saravanan, R., Montuoro, R., Nakamura, H., Wu, D., Lin, X., and Wu, L.: Importance of Resolving Kuroshio Front and Eddy Influence in Simulating the North Pacific Storm Track, *J. Climate*, 30, 1861–1880, <https://doi.org/10.1175/JCLI-D-16-0154.1>, 2017.
- Maloney, E. D. and Chelton, D. B.: An assessment of sea surface temperature influence on surface winds in numerical weather prediction and climate models. *J. Climate*, 19, 2743–2762, <https://doi.org/10.1175/JCLI3728.1>, 2006.
- Manabe, S. and Strickler, R. F.: Thermal Equilibrium of the Atmosphere with a Convective Adjustment, *J. Atmos. Sci.*, 21, 361–385, [https://doi.org/10.1175/1520-0469\(1964\)021%3C0361:TEOTAW%3E2.0.CO;2](https://doi.org/10.1175/1520-0469(1964)021%3C0361:TEOTAW%3E2.0.CO;2), 1964.
- Manabe, S. and Wetherald, R. T.: Thermal Equilibrium of the Atmosphere with a Given Distribution of Relative Humidity, *J. Atmos. Sci.*, 24, 241–259, [https://doi.org/10.1175/1520-0469\(1967\)024%3C0241:TEOTAW%3E2.0.CO;2](https://doi.org/10.1175/1520-0469(1967)024%3C0241:TEOTAW%3E2.0.CO;2), 1967.
- Marshall, J. and Molteni, F.: Toward a Dynamical Understanding of Planetary-Scale Flow Regimes, *J. Atmos. Sci.*, 50, 1792–1818, [https://doi.org/10.1175/1520-0469\(1993\)050%3C1792:TADUOP%3E2.0.CO;2](https://doi.org/10.1175/1520-0469(1993)050%3C1792:TADUOP%3E2.0.CO;2), 1993.
- Martin, E. R., C. Thorncroft, and B. B. Booth: The multidecadal Atlantic SST— Sahel rainfall teleconnection in CMIP5 simulations, *J. Climate*, 27, 784–806, <https://doi.org/10.1175/JCLI-D-13-00242.1>, 2014.
- Martin, P. E., Arbic, B. K., Hogg, A. McC., Kiss, A.E., Munroe, J. R., and Blundell, J. R.: Frequency-domain analysis of the energy budget in an idealized coupled ocean–atmosphere model, *J. Climate*, 33, 707–726, <https://doi.org/10.1175/JCLI-D-19-0118.1>, 2020.
- Mastilovic, I. and Kravtsov, S.: Climatic effects of mesoscale ocean–atmosphere interaction in an idealized coupled model, *Geophys. Res. Abstr.*, 21, EGU2019-8383, EGU General Assembly 2019, <https://meetingorganizer.copernicus.org/EGU2019/EGU2019-8383.pdf>, 2019.
- McDougall, T. and Dewar, W.: Vertical mixing and cabbeling in layered models, *J. Phys. Oceanogr.*, 28, 1458–1480, [https://doi.org/10.1175/1520-0485\(1998\)028%3C1458:VMACIL%3E2.0.CO;2](https://doi.org/10.1175/1520-0485(1998)028%3C1458:VMACIL%3E2.0.CO;2), 1998.



- McGillicuddy, D., Laurence A. Anderson, Nicholas R. Bates, Thomas Bibby, Ken O. Buesseler, Craig A. Carlson, Cabell S. Davis, Courtney Ewart, Paul G. Falkowski, Sarah A. Goldthwait, Dennis A. Hansell, William J. Jenkins, Rodney Johnson, Valery K. Kosnyrev, James R. Ledwell, Qian P. Li, David A. Siegel, Deborah K. Steinberg: Eddy/wind interactions stimulate extraordinary mid-ocean plankton blooms. *Science*, 316, 1021– 1026, <https://doi.org/10.1126/science.1136256>, 2007.
- Meredith, M. P. and Hogg, A. M.: Circumpolar response of Southern Ocean eddy activity to a change in the Southern Annular Mode, *Geophys. Res. Lett.*, 33, <https://doi.org/10.1029/2006GL026499>, 2006.
- Miller, A. J. and Schneider, N.: Interdecadal climate regime dynamics in the North Pacific Ocean: Theories, observations and ecosystem impacts, *Prog. Oceanogr.*, 47, 355–379, [https://doi.org/10.1016/S0079-6611\(00\)00044-6](https://doi.org/10.1016/S0079-6611(00)00044-6), 2000.
- Minobe, S., Kuwano-Yoshida, A. , Komori, N., Xie, S.-P., and Small, R. J.: Influence of the Gulf Stream on the troposphere, *Nature*, 452, 206–209, <https://doi.org/10.1038/nature06690>, 2008.
- Nakamura, H. and Yamane, S.: Dominant anomaly patterns in the near-surface baroclinicity and accompanying anomalies in the atmosphere and oceans. Part I: North Atlantic Basin. *J. Climate*, 22, 880–904, <https://doi.org/10.1175/2008JCLI2297.1>, 2009.
- Nakamura, H., A. Nishina, and S. Minobe: Response of Storm Tracks to Bimodal Kuroshio Path States South of Japan. *J. Climate*, 25, 7772–7779, <https://doi.org/10.1175/JCLI-D-12-00326.1>, 2012.
- Nakamura, H., Sampe, T., Goto, A., Ohfuchi, W., and Xie, S.-P.: On the importance of midlatitude oceanic frontal zones for the mean state and dominant variability in the tropospheric circulation, *Geophys. Res. Lett.*, 35, L15709, <https://doi.org/10.1029/2008GL034010>, 2008.
- Nonaka, M., and Xie, S.-P.: Covariations of Sea Surface Temperature and Wind over the Kuroshio and Its Extension: Evidence for Ocean-to-Atmosphere Feedback. *Journal of Climate*, 16(9), 1404–1413. <http://www.jstor.org/stable/26249708>, 2003.
- O’Neill, L. W., Chelton, D. B., and Esbensen, S. K.: Covariability of surface wind and stress responses to sea surface temperature fronts, *J. Climate*, 25, 5916–5942, <https://doi.org/10.1175/JCLI-D-11-00230.1>, 2012.
- O’Neill, L. W., Chelton, D. B., and Esbensen, S. K.: The effects of SST-induced surface wind speed and direction gradients on midlatitude surface vorticity and divergence, *J. Climate*, 23, 255–281, <https://doi.org/10.1175/2009JCLI2613.1>, 2010.
- O’Neill, L. W., D. B. Chelton, and S. K. Esbensen: Observations of SST-induced perturbations of the wind stress field over the Southern Ocean on seasonal timescales. *J. Climate*, 16, 2340–2354, <https://doi.org/10.1175/2780.1>, 2003.

O'Neill, L. W., D. B. Chelton, S. K. Esbensen, and F. J. Wentz: High-Resolution Satellite Measurements of the Atmospheric Boundary Layer Response to SST Variations along the Agulhas Return Current. *J. Climate*, **18**, 2706–2723, <https://doi.org/10.1175/JCLI3415.1>, 2005.

O'Reilly, C. H. and Czaja, A.: The response of the Pacific storm track and atmospheric circulation to Kuroshio Extension variability, *Q. J. Roy. Meteor. Soc.*, **141**, 52–66, <https://doi.org/10.1002/qj.2334>, 2015.

O'Reilly, C. H., S. Minobe, and A. Kuwano-Yoshida, and T. Woollings: The Gulf Stream influence on wintertime North Atlantic jet variability. *Quart. J. Roy. Meteor. Soc.*, **143**, 173–183, <https://doi.org/10.1002/qj.2907>, 2017.

O'Reilly, C. H., S. Minobe, and A. Kuwano-Yoshida: The influence of the Gulf Stream on wintertime European blocking. *Climate Dyn.*, **47**, 1545–1567, <https://doi.org/10.1007/s00382-015-2919-0>, 2016.

Parfitt, R., Czaja, A., Kwon, Y.-O.: The impact of SST resolution change in the ERA-Interim reanalysis on wintertime Gulf Stream frontal air-sea interaction, *Geophys. Res. Lett.*, **44**, 3246–3254, <https://doi.org/10.1002/2017GL073028>, 2017.

Perlin, N., De Szoeko, S. P., Chelton, D. B., Samelson, R. S., Skillingstad, E. D., and O'Neill, L. W.: Modeling the atmospheric boundary layer wind response to mesoscale sea surface temperature perturbations, *Mon. Weather Rev.*, **142**, 4284–4307, <https://doi.org/10.1175/MWR-D-13-00332.1>, 2014.

Piazza, M., Terray, L., Boé, J., Maisonnave, E., and Sanchez-Gomez, E.: Influence of small-scale North Atlantic sea surface temperature patterns on the marine boundary layer and free troposphere: A study using the atmospheric ARPEGE model, *Clim. Dynam.*, **46**, 1699–1717, <https://doi.org/10.1007/s00382-015-2669-z>, 2016.

Primeau, F. W.: Multiple equilibria and low-frequency variability of the wind-driven ocean circulation, *J. Phys. Oceanogr.*, **32**, 2236–2252, [https://doi.org/10.1175/1520-0485\(2002\)032%3C2236:MEALFV%3E2.0.CO;2](https://doi.org/10.1175/1520-0485(2002)032%3C2236:MEALFV%3E2.0.CO;2), 2002.

Putrasahan, D. A., Kamenkovich, I., Le Henaff, M., and Kirtman, B. P.: Importance of oceanic mesoscale variability for air-sea interactions in the Gulf of Mexico, *Geophys. Res. Lett.*, **44**, 6352–6362, <https://doi.org/10.1002/2017GL072884>, 2017.

Putrasahan, D. A., Miller, A. J., and Seo, H.: Isolating mesoscale coupled ocean–atmosphere interactions in the Kuroshio Extension region, *Dyn. Atmos. Oceans*, **63**, 60–78, <https://doi.org/10.1016/j.dynatmoce.2013.04.001>, 2013.

Ramanathan, V. and Coakley, J. A.: Climate modeling through radiative-convective models, *Rev. Geophys.*, **16**, 465–489, <https://doi.org/10.1029/RG016i004p00465>, 1978.

Schneider, N. and Qiu, B.: The atmospheric response to weak sea surface temperature fronts, *J. Atmos. Sci.*, **72**, 3356–3377, <https://doi.org/10.1175/JAS-D-14-0212.1>, 2015.

Seo, H., and Coauthors: Ocean Mesoscale and Frontal-Scale Ocean–Atmosphere Interactions and Influence on Large-Scale Climate: A Review. *J. Climate*, 36, 1981–2013, <https://doi.org/10.1175/JCLI-D-21-0982.1>, 2023.

Seo, H., Miller, A. J., and Norris, J. R.: Eddy-wind interaction in the California Current System: dynamics and impacts, *J. Phys. Oceanogr.*, 46, 439–459, <https://doi.org/10.1175/JPO-D-15-0086.1>, 2016.

Shevchenko, I., Berloff, P., Guerrero-Lopez, D., and Roman, J.: On low-frequency variability of the midlatitude ocean gyres, *J. Fluid Mech.*, 795, 423–442, [doi:10.1017/jfm.2016.208](https://doi.org/10.1017/jfm.2016.208), 2016.

Siebert, S., D. B. Stephenson, P. G. Sansom, A. A. Scaife, R. Eade, and A. Arribas: A Bayesian Framework for Verification and Recalibration of Ensemble Forecasts: How Uncertain is NAO Predictability? *J. Climate*, 29, 995–1012, <http://dx.doi.org/10.1175/JCLI-D-15-0196.1>, 2016.

Siqueira, L. and Kirtman, B. P.: Atlantic near-term climate variability and the role of a resolved Gulf Stream, *Geophys. Res. Lett.*, 43, 3964–3972, <https://doi.org/10.1002/2016GL068694>, 2016.

Siqueira, L., B. P. Kirtman, and L. C. Laurindo: Forecasting remote atmospheric responses to decadal Kuroshio stability transitions. *J. Climate*, 34, 379–395, <https://doi.org/10.1175/JCLI-D-20-0139.1>, 2021.

Small, R. J., De Szoeki, S. P., Xie, S.-P., O’Neill, L., Seo, H., Song, Q., Cornillon, P., Spall, M., and Minobe, S.: Air–sea interaction over ocean fronts and eddies, *Dyn. Atmos. Oceans*, 45, 274–319, <https://doi.org/10.1016/j.dynatmoce.2008.01.001>, 2008.

Small, R., Tomas, A., and Bryan, F. O.: Storm track response to ocean fronts in a global high-resolution climate model, *Clim. Dynam.*, 43, 805–828, <https://doi.org/10.1007/s00382-013-1980-9>, 2014.

Stern, M.: Interaction of a uniform wind stress with a geostrophic vortex. *DeepSea Res. Oceanogr. Abstr.*, 12, 355–367, [https://doi.org/10.1016/0011-7471\(65\)90007-0](https://doi.org/10.1016/0011-7471(65)90007-0), 1965.

Stockdale, T. N., F. Molteni and L. Ferranti: Atmospheric initial conditions and the predictability of the Arctic Oscillation, *Geophys. Res. Lett.*, 42, 1173–1179, <https://doi.org/10.1002/2014GL062681>, 2015.

Sugimoto, S., B. Qiu, and N. Schneider: Local Atmospheric Response to the Kuroshio Large Meander Path in Summer and Its Remote Influence on the Climate of Japan. *J. Climate*, 34, 3571–3589, <https://doi.org/10.1175/JCLI-D-20-0387.1>, 2021.

Taguchi, B., Nakamura, H., Nonaka, M., and Xie, S.-P.: Influences of the Kuroshio/Oyashio Extensions on air–sea heat exchanges and storm-track activity as revealed in regional atmospheric model simulations for the 2003/04 cold season, *J. Climate*, 22, 6536–6560, <https://doi.org/10.1175/2009JCLI2910.1>, 2009.

- Tsopouridis, L., C. Spensberger, and T. Spengler: Cyclone intensification in the Kuroshio region and its relation to the sea surface temperature front and upper-level forcing. *Quart. J. Roy. Meteor. Soc.*, 147, 485–500, <https://doi.org/10.1002/qj.3929>, 2021.
- Wallace, J. M., Mitchell, T. P., and Deser, C.: The influence of sea-surface temperature on surface wind in the eastern equatorial Pacific: seasonal and interannual variability, *J. Climate*, 2, 1492– 1499, [https://doi.org/10.1175/1520-0442\(1989\)002%3C1492:TIOSST%3E2.0.CO;2](https://doi.org/10.1175/1520-0442(1989)002%3C1492:TIOSST%3E2.0.CO;2), 1989.
- Willison, J., Robinson, W. A., and Lackmann, G. M.: The importance of resolving mesoscale latent heating in the North Atlantic storm track, *J. Atmos. Sci.*, 70, 2234–2250, <https://doi.org/10.1175/JAS-D-12-0226.1>, 2013.
- Wills, S. M., and D. W. J. Thompson and L. M. Ciasto: On the observed relationships between variability in Gulf Stream Sea surface temperatures and the atmospheric circulation over the North Atlantic. *J. Climate*, 29, 3719–3730, <https://doi.org/10.1175/JCLI-D-15-0820.1>, 2016
- Wyatt, M. G., and J. A. Curry: Role for Eurasian Arctic shelf sea ice in a secularly varying hemispheric climate signal during the 20th century, *Climate Dyn.*, 42, 2763– 2782, <http://dx.doi.org/10.1007/s00382-013-1950-2>, 2014.
- Xie, S.-P.: Satellite observations of cool ocean–atmosphere interaction, *B. Am. Meteorol. Soc.*, 85, 195–208, <https://doi.org/10.1175/BAMS-85-2-195>, 2004.
- Yuan, T., Lazaros Oreopoulos, Mark Zelinka, Hongbin Yu, Joel R. Norris, Mian Chin, Steven Platnick, and Kerry Meyer: Positive low cloud and dust feedbacks amplify tropical North Atlantic Multidecadal Oscillation, *Geophys. Res. Lett.*, 43, 1349–1356, <https://doi.org/10.1002/2016GL067679>, 2016.

# Appendices

## Appendix A: Summary of model updates and code modifications

Changes to the model formulation are summarized below in Table A1. Table A2 outlines the corresponding changes in the Q-GCM source code.

Table A1 - Differences between updated and original Q-GCM formulation.

UPDATES	ORIGINAL MODEL
New radiative-convective scheme to derive the atmospheric mean state and perturbation equations	Purely radiative equilibrium
Constant thickness, gray-body atmospheric mixed layer	Variable thickness, blackbody atmospheric mixed layer
Reduced gravities (and, hence, Rossby radii) in the atmosphere computed using the mean-state parameters derived from the radiative-convective equilibrium above	Reduced gravities (and Rossby radii) specified independently of the radiative-equilibrium mean-state parameters
Modified entrainment parameterization: <ul style="list-style-type: none"> <li>• Ekman driven, upwind differencing in the oceanic mixed layer.</li> <li>• Ekman driven, upwind differencing in the atmospheric mixed layer, with effective interior temperature depending on atmospheric state, resulting in stable formulation.</li> <li>• Interior entrainment active in both lower and upper atmosphere, optional addition of weak vertical diffusion.</li> </ul>	<ul style="list-style-type: none"> <li>• Ekman driven, central differences.</li> <li>• Turbulence driven, depending on variable mixed layer thickness, with zero contribution to interior thermal forcing to achieve stability.</li> <li>• Interior entrainment in the lower atmosphere only.</li> </ul>
Sensible/latent-heat exchange with (relative) wind speed dependence in the bulk formula.	No dependence on wind speed in the bulk formulas.
Reduced surface drag over ocean.	Uniform surface drag
Convection is neglected	Convective adjustment in both mixed layers
Temperature-dependent mixed-layer winds, with a possibility of a partially coupled setup, in which ocean and atmosphere experience different wind stress	Mixed-layer winds that do not depend on temperature
Open boundary conditions for mass and temperature equations in the mixed-layer formulation for both ocean and atmosphere	No-flow (for atmosphere only) insulating conditions (for both mixed layers), except for the specified temperature at the oceanic mixed layer's southern boundary (in the Northern Hemisphere formulation)
Addition of an active hydrological cycle, including moisture advection and latent-heat feedbacks in the atmosphere	Dry model

Table A2 - Changes in the source code.

FILE NAME	SUMMARY OF CHANGES
Makefile	Modified to account for new hra_out (high-resolution atmospheric output) module, as well as for new dependencies between modules
make.config	Includes new model options using flags highres_output (high-resolution atmospheric output over ocean), temp_fdbck (temperature-dependent AML winds), and partial_coup (partial temperature dependent wind-stress coupling); note: do not activate sb_hflux or nb_hflux options due to new – open boundary – conditions in ocean mixed layer; the new moist-model formulation is activated by the flag moist; the option dry_latent uses the dry entrainment estimates (Eqs. 23–24) in computing the moisture entrainment fluxes in Eq. (34); without this flag, the updated estimates as per Eq. (37) are used.
input.params	The spaces previously used for optical depths are now used for the corresponding layer emissivity, stored in zm, zopt(k); note that the atmospheric and oceanic mean-state parameters, including atmospheric reduced gravities, are now overwritten in radsubs.f; for the moist model: several new parameters are added, in particular the parameters $C_h$ and $C_e$ ; new output options are included as well
out_param.f	Modified to output additional parameters associated with the new radiative-convective scheme and the moist-model formulation
parameters_data.f	Added parameters related to high-resolution atmospheric output over ocean; moved the placement of the ocean off the axis of the atmospheric channel to break north–south symmetry
atstate_data.f	Added workspace for entrainment across the upper atmospheric interface entat1
atconst_data.f	For the moist model, added atmospheric-layer representative densities
inrfac_data.f	Added ssta: the atmospheric-resolution SST field over ocean obtained by averaging ocean-resolution SST within the boundaries of atmospheric cells; for the moist model: added evapa (evaporation at atmospheric resolution) and new heat-exchange coefficient variables $C_e$ and $C_h$
radiate_data.f	Modified to include parameters of entrainment formulation across both atmospheric interfaces (rather than only for the lower interface, as before)
hra_out.f, highresout.f	New module/additional code performing high-resolution atmospheric output over ocean
radsubs.f	New radiative-convective scheme; for the moist model: new moist-model parameters – initial humidities, atmospheric-layer densities, and initialization of evaporative flux over land
xfosubs.f	xforc: temperature-dependent AML wind (involving, among other things, an additional bicubic interpolation of AML temperature to ocean resolution), partial coupling option, updated formulation of AML and OML forcing, including wind-speed dependence of the sensible/latent-heat exchange; the parameters $\alpha T$ and $\alpha$ are specified within xforc and can be zeroed out individually to test different mechanisms of temperature-dependent wind; code in bcuini modified to compute the actual (non-zero) wind stress at the atmospheric zonal boundaries, with an option (in comments) to close the boundary by imposing the no-through-flow condition; for the moist model: modified formulation of the sensible/latent heat exchange
amlsubs.f	aml: constant AML thickness, new radiation and entrainment model, convection neglected; amladf: open boundaries for advection; for the moist model: step atmospheric humidity equations, modify latent-heat corrections to the interior entrainment
omlsubs.f	oml: upwind advection for Ekman-driven entrainment (in the current form, the OML entrainment is set to use the climatological difference between OML and layer-1 temperature: this results in a bit larger and more realistic SST north–south SST contrasts); omladf: open boundaries for advection
qgasubs.f	Added PV sources due to entrainment in the upper atmosphere (across the upper interface)
q-gcm.f	modified to include the high-atmospheric-resolution output module; call to radiat (Fortran code’s radiate module) moved up to update and record the mean-state parameters computed and overwritten by radsubs.f (these are atmospheric and oceanic mean temperatures, atmospheric reduced gravities); for the moist model: new I/O specifications and initialization
nc_subs.f	for the moist model: new netCDF I/O

## Appendix B: QGPV equation in a layered atmospheric model

Consider an ideal-gas dry atmosphere comprised of layers with constant potential temperatures  $\theta_k$ . Using the definition of potential temperature, using the ideal gas law, and assuming hydrostatic balance (and dropping, in this section, the left superscript “a” that denotes atmospheric variables in the main text),

$$\theta = T \left( \frac{P_0}{P} \right)^{\frac{R}{C_p}}; \quad P = \rho RT; \quad \frac{\partial P}{\partial z} = -\rho g \quad (39)$$

one can express the pressures within each layer  $P_k$  as

$$P_k^{\frac{R}{C_p}} = -P_0^{\frac{R}{C_p}} \frac{z}{H_{\theta k}} + C_k(x, y); \quad H_{\theta k} \equiv \frac{C_p \theta_k}{g} \quad (A2)$$

The perturbation fields  $C_k$  can be found by requiring the pressure to be continuous across each atmospheric interface, namely

$$P_1|_{H_m} = P_m(x, y, t); \quad P_1|_{H_m+H_1+\eta_1} = P_2|_{H_m+H_1+\eta_1}; \quad P_2|_{H_m+H_1+H_2+\eta_2} = P_3|_{H_m+H_1+H_2+\eta_2} \quad (A3)$$

where  $P_m$  is the pressure at the top of the atmospheric mixed layer. For example, from Eqs.

(A1)–(A3) we have, for the first atmospheric layer

$$T_1 = \theta_1 F_1; \quad P_1 = P_0 F_1^{\frac{C_p}{R}}; \quad \rho_1 = \frac{P_0}{R \theta_1} F_1^{\frac{C_p}{R}-1} \quad (A4a)$$

where



$$F_1(x, y, z, t) = \left(\frac{P_m}{P_0}\right)^{\frac{R}{C_p}} - \frac{(z - H_m)}{H_{\theta_1}} \quad (\text{A4b})$$

From Eq. (A4), the horizontal pressure gradient force in this layer is

$$-\frac{1}{\rho_1} \nabla P_1 = -\nabla C_p \theta_1 \left(\frac{P_m}{P_0}\right)^{\frac{R}{C_p}} = -\nabla \psi_1 f_0 \quad (\text{A5a})$$

Here, the lower layer streamfunction  $\psi_1$  is given by

$$\psi_1 = \frac{C_p \theta_1}{f_0} \left(\frac{P_m}{P_0}\right)^{\frac{R}{C_p}} \approx \frac{C_p \bar{\theta}}{f_0} \left(\frac{P_m}{P_0}\right)^{\frac{R}{C_p}}, \quad (\text{A5b})$$

where  $\bar{\theta} \sim 300K$  is the representative atmospheric potential temperature taken here to be equal, approximately, to the vertical average of individual-layer potential temperatures. In an analogous way, we find, for streamfunctions in layers 2 and 3,

$$\psi_2 = \frac{C_p \theta_2}{f_0} \left( \left(\frac{P_m}{P_0}\right)^{\frac{R}{C_p}} - \left(\frac{1}{H_{\theta_1}} - \frac{1}{H_{\theta_2}}\right) \eta_1 \right) \approx \psi_1 - \frac{g'_1 \eta_1}{f_0}, \quad (\text{A5c})$$

$$\psi_3 = \frac{C_p \theta_3}{f_0} \left( \left(\frac{P_m}{P_0}\right)^{\frac{R}{C_p}} - \left(\frac{1}{H_{\theta_1}} - \frac{1}{H_{\theta_2}}\right) \eta_1 - \left(\frac{1}{H_{\theta_2}} - \frac{1}{H_{\theta_3}}\right) \eta_2 \right) \approx \psi_2 - \frac{g'_2 \eta_2}{f_0}, \quad (\text{A5d})$$

where we assumed that the differences between the potential temperatures of individual layers are small compared to  $\bar{\theta}$  and estimated reduced gravities as

$$g'_k = g \frac{\theta_{k+1} - \theta_k}{\bar{\theta}} \quad (\text{A6})$$

From Eq. (A5) it follows that

$$\eta_k = f_0 \frac{\psi_k - \psi_{k+1}}{g'_k} \quad (\text{A7})$$

and that the “dynamic pressures”  $^a p_k$  in Hogg et al., 2014 are equal to  $f_0 \psi_k$ . Furthermore, under synoptic scaling, the continuity equation in each layer is approximately

$$\frac{\partial u}{\partial x} + \frac{\partial v}{\partial y} + \frac{\partial w}{\partial z} - \frac{w}{H_{\theta k}} = 0, \quad (\text{A8})$$

but the last term on the right-hand side of Eq. (A8) – approximating  $\frac{w}{\rho} \frac{\partial \rho}{\partial z}$  – is smaller than other terms and can be neglected under QG scaling, since  $H_{\theta k} \simeq 30 \text{ km}$  and  $H_k / H_{k\theta} \sim 0.1$  is on the order of the Rossby number.

Thus, the above scaling arguments and calculations demonstrate the validity of Boussinesq approximation for quasi-geostrophic compressible atmosphere and justify the uniform treatment of oceanic and atmospheric dynamics in Hogg et al., 2014.

## Appendix C: Code availability

The MQ-GCM model is available from Zenodo at <https://doi.org/10.5281/zenodo.5250828> (Kravtsov et al., 2021b). The model's code is now under GNU General Public License v3.0 or later. The updated code alongside basic instructions on its use (see readme file there) and restart files for the six simulations described in Section 4.2 are also publicly available from GitHub at <https://github.com/GFDANU/q-gcm> and from Zenodo at <https://doi.org/10.5281/zenodo.4916720> (Kravtsov et al. 2021a). To use the code, one should replace the routines and scripts of the original source code (publicly available at <http://www.q-gcm.org>) summarized in Table 3 by their updated versions (contained in the new MQ-GCM folder on GitHub) and compile/run the resulting executable in the same way as in original version (see Hogg et al., 2014).

## Curriculum Vitae

### Ilijana Mastilovic

---

#### Education

---

- |                  |  |
|------------------|--|
| <b>2017-2023</b> | <b>University of Wisconsin – Milwaukee, Ph.D., Atmospheric Science</b><br>Advisor: Prof. Sergey Kravtsov         |
| <b>2021-2023</b> | <b>University of Wisconsin – Milwaukee, Graduate Certificate in Artificial Intelligence and Machine Learning</b> |
| <b>2013-2014</b> | <b>University of Belgrade, M.S., Meteorology</b><br>Advisor: Prof. Ivana Tošić                                   |
| <b>2007-2013</b> | <b>University of Belgrade, B.S. with honors, Meteorology</b>   |

---

#### Experience

---

- |                  |   |
|------------------|---|
| <b>2017-2023</b> | <b>Graduate Researcher, University of Wisconsin - Milwaukee</b>                     |
| <b>2017-2023</b> | <b>Teaching assistant, University of Wisconsin - Milwaukee</b>                      |
| <b>2022-2022</b> | <b>Researcher, Frontier Development Lab Program 2022</b>                            |
| <b>2017-2021</b> | <b>Meteorologist, Innovative Weather at UWM</b>                                     |
| <b>2014-2017</b> | <b>Aviation Meteorologist, Bosnia and Herzegovina Air Navigation Service Agency</b> |
| <b>2013-2014</b> | <b>Graduate Research Assistant, University of Belgrade</b>                          |

---

## Award and honors

---

2023	Dhirenda Sikdar Memorial Scholarship, University of Wisconsin – Milwaukee
2022	Award of Merit, Frontier Development Lab 2022
2020	Dhirenda Sikdar Memorial Scholarship, University of Wisconsin – Milwaukee
2008-2012	Scholarship from city of Tivat, Montenegro
2007	'Luca II' award for maintaining great grades for all four years in high school.

---

## Peer-review publications

---

- Kravtsov, S., **Mastilovic, I.**, Hogg, A. McC., Dewar, W. K., and Blundell, J. R.: The Moist Quasi-Geostrophic Coupled Model: MQ-GCM 2.0, *Geosci. Model Dev.*, 15, 7449–7469, <https://doi.org/10.5194/gmd-15-7449-2022>, 2022.
- **Under review:** Kurihana, T., **Mastilovic, I.**, Wang, L., Meray, A., Praveen, S., Xu, Z., Memarzadeh, M., Lavin, A., Wainwright, H. M: Identifying Climate Patterns using Clustering Autoencoder Techniques: T, *Journal of Artificial Intelligence for the Earth Systems*, American Meteorological Society
- **Under review:** Meray, A., Wang, L., Kurihana, T., **Mastilovic, I.**, Praveen, S., Xu, Z., Memarzadeh, M., Lavin, A., Wainwright, H. M: Physics-Informed Surrogate Modeling for Supporting Climate Resilience at Groundwater Contamination Sites, *Journal of Computers & Geosciences*, Elsevier

---

## Selected Presentations

---

- **Mastilovic I.**, Kravtsov S., Hogg A., Dewar W., Blundell J.: "A Moist Quasi-Geostrophic Coupled Model", Mesoscale and Frontal-Scale Air-Sea Interactions Workshop 2023 [Poster]
- L. Wang, T. Kurihana, A. Meray, **I. Mastilovic**, S. Praveen, Z. Xu, M. Memarzadeh, A. Lavin, H. Murakami-Wainwright, "Physics-informed surrogate modeling for supporting climate resilience at groundwater contamination sites", American Geophysical Union, Fall Meeting 2022 [Poster]

- L. Wang, T. Kurihana, A. Meray, **I. Mastilovic**, S. Praveen, Z. Xu, M. Memarzadeh, A. Lavin, H. Murakami-Wainwright: "Multi-scale Digital Twin: Developing a fast and physics-infused surrogate model for groundwater contamination with uncertain climate models", Machine Learning and the Physical Sciences Workshop at the 36th conference on Neural Information Processing Systems [Poster]
- L. Wang, T. Kurihana, A. Meray, **I. Mastilovic**, S. Praveen, Z. Xu, M. Memarzadeh, A. Lavin, H. Murakami-Wainwright: "Physics-informed surrogate modeling for supporting climate resilience at groundwater contamination sites", Frontier Development Lab 2022 Live Showcase [Oral]
- **Mastilovic I.**, Kravtsov S., Hogg A., Dewar W., Blundell J.: "A Moist Quasi-Geostrophic Coupled Model: MQ-GCM2.0", 102nd American Meteorological Society Annual Meeting [Poster]
- **I. Mastilovic** and S. Kravtsov: "Climatic effects of mesoscale ocean–atmosphere interaction in an idealized coupled model ", European Geosciences Union 2019 [Poster]